HAL
open science

# Multi-user Data Transmission in Optical Wireless Body-Area Networks for Medical Applications

Md Jahid Hasan

## To cite this version:

Md Jahid Hasan. Multi-user Data Transmission in Optical Wireless Body-Area Networks for Medical Applications. Signal and Image processing. Ecole Centrale Marseille, 2021. English. NNT : 2021ECDM0010 . tel-03873596

**HAL Id: tel-03873596**

**https://theses.hal.science/tel-03873596**

Submitted on 27 Nov 2022

**HAL** is a multi-disciplinary open access archive for the deposit and dissemination of scientific research documents, whether they are published or not. The documents may come from teaching and research institutions in France or abroad, or from public or private research centers.

L'archive ouverte pluridisciplinaire **HAL**, est destinée au dépôt et à la diffusion de documents scientifiques de niveau recherche, publiés ou non, émanant des établissements d'enseignement et de recherche français ou étrangers, des laboratoires publics ou privés.

École Doctorale 352

Unité de recherche – INSTITUT FRESNEL et OLEDCOMM

# THÈSE DE DOCTORAT

pour obtenir le grade de

DOCTEUR de L'ÉCOLE CENTRALE de MARSEILLE

Discipline:

Optique, Photonique et Traitement d'Image

**TITRE DE LA THÈSE:**

# Techniques de Transmission Multi-utilisateurs pour les Réseaux Corporels Médicaux Utilisant la Technologie d'Optique Sans-fil

Par

**Md Jahid HASAN**

**Directeur de thèse:** Dr. Mohammad-Ali KHALIGHI

**Co-Directeur de thèse:** Dr. Luis Nero ALVES

*Soutenue le 26 Novembre 2021*

*devant le jury composé de:*

| | | |
|---|---|---|
| Mr. Luc CHASSAGNE | Université Versailles Saint-Quentin, France | Rapporteur |
| Mme. Christelle AUPETIT | XLIM, Limoges, France | Rapporteur |
| Mr. Kosai RAOOF | Université du Mans, France | Examinateur |
| Mr. Rafael PEREZ | Université de Gran Canaria, Espagne | Examinateur |
| Mr. Paolo MONTI | Université de Technologie Chalmers, Suède | Examinateur |
| Mr. Bastien BÉCHADERGUE | Université Versailles Saint-Quentin, France | Examinateur |
| Mr. Mohammad-Ali KHALIGHI | École Centrale Marseille, France | Dir. de thèse |
| Mr. Luis Nero ALVES | Institut de Télécommunications, Portugal | Co-Dir. de thèse |

ANNÉE : 2021

Doctoral School 352
Research unit – FRESNEL INSTITUTE and OLEDCOMM

# DOCTORAL THESIS

to obtain the degree of Doctor of Philosophy
issued by ÉCOLE CENTRALE MARSEILLE

Discipline:
Optics, Photonics and Image Processing

**THESIS TITLE:**

# Multi-user Data Transmission in Optical Wireless Body-Area Networks for Medical Applications

by

**Md Jahid HASAN**

**Thesis advisor:** Dr. Mohammad-Ali KHALIGHI
**Thesis co-advisor:** Dr. Luis Nero ALVES

*Presented and defended on 26 November 2021*

*in front of the thesis committee composed of:*

| | | |
|---|---|---|
| Prof. Luc CHASSAGNE | University Versailles Saint-Quentin, France | Reviewer |
| Prof. Christelle AUPETIT | XLIM, Limoges, France | Reviewer |
| Prof. Kosai RAOOF | University of Maine, France | Examiner |
| Prof. Rafael PEREZ | University of Gran Canaria, | Examiner |
| Prof. Paolo MONTI | Chalmers University of Technology, Sweden | Examiner |
| Dr. Bastien BÉCHADERGUE | University Versailles Saint-Quentin, France | Examiner |
| Dr. Mohammad-Ali KHALIGHI | École Centrale Marseille, France | Thesis advisor |
| Dr. Luis Nero ALVES | Institute of Telecommunications, Portugal | Thesis co-advisor |

YEAR : 2021

## Acknowledgments

To begin, all praise is due to almighty Allah, who bestowed this wondrous existence onto us. Without blessings of Allah, I would not have made it this far.

I would like to express my heartfelt gratitude and appreciation to my thesis supervisor, Dr. Ali Khalighi, for his insight, knowledge, and guidance. It was mainly his excellent supervision, dedication, and great attention that have contributed to the completion of this thesis work. Being your student has been an incredible honor and privilege. Sincere thanks to Dr. Luis Nero Alves, my co-supervisor, for his assistance and interesting discussions.

I am grateful to the "Vision" project, which was funded by the European Union's Horizon 2020 research and innovation program, for providing me with the scholarship to complete my PhD. I am highly indebted to Oledcomm for hosting me as part of the Vision ITN program and making the necessary arrangements during this difficult COVID pandemic. Sincere gratitude to Institut Fresnel and École Centrale Marseille, who offered me the opportunity to carry out the research.

I wish to convey my deepest gratitude to the reviewers Prof. Christelle Aupetit and Prof. Luc Chassagne, for their detailed and constructive comments on my work. My sincere thanks to Prof. Kosai Raoof, Prof. Rafael Perez, and Prof. Paolo Monti for their participation in the jury and careful review of my manuscript. I would also like to thank Dr. Bastien Béchadergue for being my supervisor at oledcomm and part of the jury, as well as for all of his support.

I owe a debt of appreciation to many people who assisted me in countless ways over the period of my PhD research. Many thanks to Dr. Jorge García-Márquez, who was my supervisor at Oledcomm for a year, for his support and advice during my research. Special thanks to Mr. Benjamin Azoulay, CEO of Oledcomm, and his technical team for their support and collaboration. I would like to express my gratitude to Prof. Volker Jungnickel for his valuable time and feedback on my work.

I would like to thank all of my friends and colleagues from the Vision project, the Institut Fresnel, and Oledcomm, from whom I have benefited greatly and spent many memorable moments. Particularly, thanks to Dr. Camilo Valencia-Estrada, Dr. Oussama Haddad, Dr. Mahmoud Eltokhey, Dr. Ikenna Chinazaekpere Ijeh, and Dr. Taha Essalih.

I owe my parents a debt of gratitude for their unwavering love and support throughout my life. Thank you for inspiring me to pursue my ambitions. My sister, younger brother, cousins, and relatives all deserve my heartfelt gratitude.

Last but not least, I am extremely grateful to my wife, Sadia Afroze, for her unconditional support and encouragement throughout these years. I can't express how happy it makes me to see you growing my son, Ayaaz, who was born during my PhD.

**TITRE**: Tchniques de Transmission Multi-utilisateurs pour les Réseaux Corporels Médicaux Utilisant la Technologie d'Optique Sans-fil

**RÉSUMÉ:**

Le secteur de la santé est en train de passer des services médicaux conventionnels à des solutions de e-santé centrées sur le patient, telles que la télésurveillance en temps réel des patients. Cette tendance contribuera à améliorer les résultats cliniques des maladies chroniques tout en réduisant les coûts liés à la santé et en augmentant la qualité de vie. De plus, dans le sillage de la pandémie mondiale de COVID-19, le suivi à distance des patients à domicile pendant la quarantaine ou dans les hôpitaux peut permettre de détecter efficacement toute détérioration soudaine de l'état de la santé et sauver des vies.

Une telle télésurveillance des patients peut être réalisée, en particulier, grâce à l'utilisation de réseaux corporels sans-fil (WBAN pour *Wireless Body Area Network*) en transmettant des données collectées à partir d'un certain nombre de capteurs médicaux sur le corps ou implantés. La majorité des solutions WBAN existantes reposent sur les transmissions radiofréquences fonctionnant dans la bande de fréquences libre, qui est de plus en plus soumise aux interférences électromagnétiques et vulnérable à l'interception et au piratage de données. Une alternative intéressante est alors d'utiliser la communication optique sans-fil basée dans la bande visible ou infrarouge (IR). Dans ce contexte, un enjeu important consiste en la transmission simultanée des données de plusieurs patients dans une chambre d'hôpital, par exemple, ce qui nécessite le développement de techniques d'accès multiple (MA pour *Multiple Access*) appropriées.

Par conséquent, l'objectif principal de cette thèse a été d'étudier et de proposer des techniques de MA appropriées pour les liaisons WBAN optiques. Le travail présenté se concentre sur la liaison montante (extra-WBAN) basée sur la transmission IR, où les données médicales collectées de plusieurs patients sont transmises àun ou plusieurs points d'accès (AP pour *Access Point*). Premièrement, nous étudions les performances de la CDMA optique (O-CDMA pour *Optical Code-Division MA*) dans des scénarios avec un nombre relativement faible d'utilisateurs, tout en prenant en compte l'effet des orientations aléatoires des émetteurs. À cette fin et pour envisager des scénarios réalistes, nous mettons en œuvre un modèle de mobilité aléatoire pour prendre en compte la mobilité des patients à l'intérieur d'une chambre d'hôpital. De plus, nous démontrons l'amélioration des performances obtenue en utilisant plusieurs points d'accès. Nous étudions également la mise en œuvre pratique du schéma O-CDMA à travers une série d'expériences. Deuxièmement, pour répondre à l'exigence de MA dans des scénarios avec un nombre relativement important d'utilisateurs, nous proposons une nouvelle solution basée sur la O-OFDMA (pour *Optical Orthogonal Frequency Division MA*), où seule la partie réelle du signal OFDMA est transmise. Nous montrons que les performances du schéma proposé, appelé O-ROFDMA, sont très proches de celles de l'O-OFDMA, tout en offrant une complexité de calcul réduite d'un facteur de 2.

**MOTS-CLÉS :** E-Santé; Réseaux corporels sans-fil; Communications optiques sans-fil; Accès multiples; Accès multiples par répartition de code; Accès multiple par répartition de fréquence.

---

**TITLE**: Multi-user Data Transmission in Optical Wireless Body-Area Networks for Medical Applications

**ABSTRACT:**

The healthcare industry is leading towards a transition from conventional medical services to patient-centric e-Health solutions, e.g., real-time remote monitoring of patients. This trend will help improve clinical outcomes of chronic diseases while reducing health-related costs and increasing the quality of life. Moreover, in the wake of the global COVID-19 pandemic, remote monitoring of patients at home during quarantine or in hospitals can effectively detect any sudden health deterioration and save lives. Such tele-monitoring of patients can be realized, in particular, through the use of wireless body-area networks (WBANs) by sending timely data from a number of on-body or implanted medical sensors. The majority of existing WBAN solutions rely on radio-frequency transmission operating in the unlicensed frequency band, which is increasingly subject to electromagnetic interference and vulnerable to data interception and hacking. An interesting alternative against these impairments is the use of license-free optical wireless communication based on visible light or infrared (IR). Within this context, an important issue consists

of simultaneous data transmission from multiple patients in a room, which requires the development of appropriate multiple access (MA) techniques. Therefore, the main objective of this thesis has been to investigate and propose suitable modulation and MA techniques for the optical WBAN links. The presented work focuses on the extra-WBAN uplink based on IR transmission, where the collected medical data of several patients is transmitted to one or several access points (APs). Firstly, we investigate the performance of optical code-division MA (O-CDMA) in scenarios with relatively small number of users, while taking into account the effect of random transmitter orientations. For this purpose and to consider realistic scenarios, we implement an orientation-based random waypoint mobility model to consider the mobility of patients inside a hospital ward. Meanwhile, we demonstrate the performance improvement achieved by using several APs. We also investigate the practical implementation of the O-CDMA scheme through a set of experiments. Secondly, to address the MA requirement in scenarios with a relatively large number of users, we propose a new solution based on orthogonal-frequency division MA (OFDMA), where only the real part of the OFDMA signal is transmitted. We show that the performance of the proposed scheme, called optical-ROFDMA, is almost the same as optical-OFDMA, while offering a reduced computational complexity of factor 2.

**KEYWORDS :** E-Health; Wireless body area networks; Optical wireless communications; Multiple access; Optical code-division multiple access; Optical-orthogonal frequency division multiple access.

---

**Adresse :**

Institut Fresnel, UMR CNRS 7249, École Centrale Marseille,
D.U. de Saint Jérôme, 13397 Marseille - France.

# Table of contents

**List of Notations** **1**

**List of Acronyms** **5**

**1 Introduction** **9**

1.1 General Context . . . . . 9

1.1.1 Remote Patient Monitoring . . . . . 9

1.1.2 Key Enabling Technologies for Remote Monitoring . . . . . 10

1.1.3 Medical WBANs . . . . . 12

1.1.4 Challenges of Existing WBAN Technology . . . . . 15

1.1.5 Interest in Optical WBANs . . . . . 15

1.2 Thesis Objectives . . . . . 16

1.2.1 Thesis Outline . . . . . 19

1.2.2 Thesis Contributions . . . . . 19

1.2.3 Author's Publications . . . . . 20

**2 Optical Transmission for Medical WBANs** **23**

2.1 Introduction . . . . . 23

2.2 Optical Wireless Signal Transmission . . . . . 24

2.2.1 Transmitter . . . . . 24

2.2.2 Receiver . . . . . 28

2.2.3 Indoor Optical Channel . . . . . 29

2.2.4 Modulation Technologies . . . . . 31

2.3 Channel Modeling for Optical WBANs . . . . . 33

2.3.1 Channel Propagation Model . . . . . 34

2.3.2 Modeling User Mobility . . . . . 35

2.4 Chapter Summary . . . . . 38

**3 Multiple Access Solutions for Optical WBANs** **41**

3.1 Introduction . . . . . 41
3.2 Conventional MA Solutions . . . . . 42
3.2.1 Orthogonal MA Solutions . . . . . 42
3.2.2 Non-orthogonal MA Solutions . . . . . 47
3.3 MA Candidates for Optical WBANs . . . . . 49
3.3.1 O-CDMA . . . . . 49
3.3.2 O-OFDMA . . . . . 51
3.3.3 O-SCFDMA . . . . . 53
3.4 Chapter Summary . . . . . 54

**4 Performance of O-CDMA for Medical WBANs 57**
4.1 Introduction . . . . . 57
4.2 Assumptions and Considered Hospital Ward Scenario . . . . . 58
4.3 BPPM O-CDMA Signaling . . . . . 59
4.4 Performance Evaluation of BPPM O-CDMA Signaling . . . . . 61
4.4.1 BER Analysis . . . . . 61
4.5 Performance Analysis . . . . . 64
4.5.1 Effect of Tx Orientation on the Received Power . . . . . 65
4.5.2 MAI Effect on Link Performance . . . . . 66
4.5.3 Interest of Using Multiple APs . . . . . 70
4.6 Chapter Summary and Discussions . . . . . 73

**5 Energy-Efficient O-OFDMA Scheme for Medical Extra-WBANs 77**
5.1 Introduction . . . . . 77
5.2 System Description . . . . . 78
5.2.1 General Assumptions . . . . . 78
5.3 Description of the Proposed MA Scheme . . . . . 80
5.3.1 DCO-ROFDMA . . . . . 81
5.3.2 ACO-ROFDMA . . . . . 82
5.3.3 Setting DC Bias and Clipping . . . . . 82
5.4 Performance Analysis . . . . . 83
5.4.1 Parameter Specification and Performance Metrics . . . . . 83
5.4.2 PAPR Analysis . . . . . 84
5.4.3 BER Performance . . . . . 85
5.4.4 Electrical Power Efficiency . . . . . 88

5.5 Elucidating MAI effect . . . . . 88
5.6 Complexity Analysis . . . . . 90
5.7 Chapter Summary . . . . . 94

**6 Experimental Implementation of O-CDMA for Medical Extra-WBANs 95**
6.1 Introduction . . . . . 95
6.2 System Description . . . . . 96
6.2.1 General Assumptions . . . . . 96
6.2.2 General Principles of OOK O-CDMA . . . . . 96
6.2.3 OOK O-CDMA Rx Structure . . . . . 97
6.2.4 Digital Design Concept on Tx/Rx Synchronization . . . . . 98
6.3 Implemetation . . . . . 99
6.3.1 Overall Architecture of O-CDMA System . . . . . 99
6.3.2 AFE Design . . . . . 100
6.3.3 CN Digital HW Design . . . . . 100
6.3.4 AP Digital HW Design . . . . . 101
6.4 Experimental Results . . . . . 102
6.4.1 Validation of Digital Design . . . . . 103
6.4.2 Validation of O-CDMA System . . . . . 103
6.5 Chapter Summary . . . . . 106

**7 Conclusions and Perspectives 107**
7.1 Conclusions . . . . . 107
7.2 Perspectives for Future Work . . . . . 108

**A Incident angle on the Reflecting Surface 111**

**B O-CDMA Acquasition and Verfication Block 113**

**List of Figures 115**

**List of Tables 121**

**Bibliography 123**

# List of Notations

| | |
|---|---|
| $(\cdot)^T$ | Transposition |
| $A_{\mathrm{PD}}$ | Photodetector's active area |
| $A_E$ | Area of the reflecting surface element |
| $B$ | Transmission bandwidth |
| $B_{\mathrm{ACO}}$ | Required bandwidths of ACO schemes |
| $\mathscr{B}_{\mathrm{DC}}$ | DC bias |
| $CK(t)$ | Sampling clock |
| $C_{\mathrm{Th}}$ | Detection threshold |
| $D$ | LOS link distance between the CN and the AP |
| $d$ | Distance between the CN and the AP |
| $D_1$ | Distance between the Tx and the $E_\iota$ |
| $D_2$ | Distance between the $E_\iota$ and the Rx |
| $\delta$ | Radiance angle of the reflected rays from $E_\iota$ |
| $E\{\cdot\}$ | Expected value |
| $E_\iota$ | Reflecting surface element |
| $\eta$ | PD quantum efficiency |
| $F$ | OOC code length |
| $\Gamma_{\mathrm{ACO}}$ | Spectral efficiency for the ACO schemes |
| $\Gamma_{u,u}$ | Auto-correlation of $u$ |
| $\Gamma_{u,v}$ | Cross-correlation of $u$ and $v$ |
| $h$ | Plank's constant |
| $h_{\mathrm{AP}}$ | AP height |
| $h_{\mathrm{CN}}$ | CN height |
| $H_{\mathrm{LOS}}$ | Channel DC gain for the LOS link |
| $H_{\mathrm{ref}}$ | Channel DC gain of the non-LOS links |
| $h(t)$ | Channel impulse response |
| $I_1$ | Mean of the correlator output corresponding to the first BPPM slot |
| $I_2$ | Mean of the correlator output corresponding to the second BPPM slot |
| $I_a$ | Ambient current noise |
| $I_d$ | Dark current noise |
| $I_{Ij}$ | Photo-current corresponding to the $j^{\mathrm{th}}$ interfering user's chip |

| | |
|---|---|
| $I_r$ | Photo-current corresponding to the desired user's chip |
| $\Im\{\cdot\}$ | Imaginary part |
| $K$ | OOC code weight |
| $K_B$ | Boltzman's constant |
| $L'$ | Room length |
| $\mathscr{L}$ | Maximum number of users |
| $L$ | Data bits per transmitted packet |
| $\ell$ | Number of interfering users |
| $\lambda_a$ | Auto-correlation constraints |
| $\lambda_c$ | Cross-correlation constraints |
| $L_p$ | Training bits |
| $M$ | QAM order |
| $\mathscr{M}$ | Number of data-carrying symbols per user |
| $m$ | Lambertian order |
| $N$ | Number of subcarriers before the HS block |
| $\mathscr{N}$ | FFT/IFFT size |
| $N_0$ | Noise power spectral density |
| $\boldsymbol{n}_{\text{AP}}$ | Normal vector corresponding to the AP |
| $\mathscr{N}_{\text{CP}}$ | Length of cyclic prefix |
| $n(t)$ | Receiver noise |
| $\boldsymbol{n}'_{\text{Tx}}$ | Normal vector corresponding to the Tx |
| $\nu$ | Light frequency |
| $\wp$ | Electrical-to-optical power conversion efficiency |
| $\partial$ | Radiance angle of the Tx |
| $P_E$ | Probability of bit error |
| $\phi_{1/2}$ | LED semi-angle at half power |
| $P_i$ | Probability of interference |
| $P_{\text{out}}$ | Outage Probability |
| $P_r$ | Total received power |
| $P_{\mathfrak{r}}$ | Received electrical power from the LOS link |
| $P_{r,d}$ | Received power from the desired user |
| $P_{r,j}$ | Received power from the $j^{\text{th}}$ interfering user |
| $\psi_c$ | Rx FOV |
| $\psi$ | Beam incident angle |
| $\psi'$ | Incident angle at the Rx |
| $P_{t(\text{elec})}$ | Average electrical transmit power |
| $P_{t(\text{opt})}$ | Average optical transmit power |
| $q_e$ | Electron charge |
| $\Re\{x_n\}$ | Real part of the signal $x_n$ |
| $\mathscr{R}$ | PD responsivity |

| | |
|---|---|
| $\Re\{\cdot\}$ | Real part |
| $R_b$ | Transmit data-rate |
| $\boldsymbol{R}$ | Rotation matrix |
| $\boldsymbol{R}_{\text{pitch}}$ | Rotation matrix about the X axis |
| $\boldsymbol{R}_{\text{roll}}$ | Rotation matrix about the Y axis |
| $\boldsymbol{R}_{\text{yaw}}$ | Rotation matrix about the Z axis |
| $r_{\text{cell}}$ | Cell radius |
| $\rho$ | Reflectivity coefficient |
| $R_L$ | Load resistance of the Rx TIA |
| $r_n$ | Discrete TD signal |
| $r(t)$ | LED instantaneous optical transmit power |
| $\mathscr{S}$ | Transition length between two points |
| $\sigma_1^2$ | Variance of the correlator output corresponding to the first BPPM slot |
| $\sigma_2^2$ | Variance of the correlator output corresponding to the second BPPM slot |
| $\sigma_T^2$ | Thermal noise variance |
| $\sigma_n^2$ | Total Rx noise variance |
| $T_c$ | Chip time |
| $\theta$ | Radiance angle of the Tx |
| $\omega_{tx}$ | Azimuth angle of the Tx |
| $\theta_{tx}$ | Elevation angle of the Tx |
| $T_{\text{OOK}}$ | OOK symbol duration |
| $f_{XY}(x,y)$ | Two dimensional PDF of the node location $(x,y)$ |
| $\mathscr{T}_p$ | Pause time |
| $\mathscr{T}$ | Transition time |
| $T_{\text{PPM}}$ | PPM symbol duration |
| $T_r$ | Noise temperature |
| $T_{\text{slot}}$ | PPM slot duration |
| $V_{\max}$ | Maximum speed of the node |
| $V_{\min}$ | Minimum speed of the node |
| $\vartheta$ | Incident angle on $E_\iota$ |
| $W'$ | Room width |
| $\chi_1$ | Correlator output corresponding to the first BPPM slot |
| $\chi_2$ | Correlator output corresponding to the second BPPM slot |
| $X_k$ | Symbols before the HS block |
| $X_{N-k}^*$ | Complex conjugate and time reversed version of $X_k$ |
| $\check{X}_{\acute{k}}$ | QAM mapped complex symbols |
| $\tilde{X}_{\hat{k}}$ | Symbols before the IFFT block |
| $\check{x}_n$ | Amplified TD signal |
| $\hat{x}_n$ | DC biased TD signal |
| $\tilde{x}_n$ | Clipped TD signal |

| | |
|---|---|
| $x_n$ | Real-valued TD signal |
| $\check{\Upsilon}_{\acute{k}}$ | Symbols after subcarrier demapping |
| $\tilde{\Upsilon}_{\hat{k}}$ | Symbols after performing FFT |
| $\Upsilon_k$ | Symbols after removing HS |
| $\alpha$ | Yaw angle |
| $\beta$ | Pitch angle |
| $\gamma$ | Roll angle |
| $y(t)$ | Baseband signal at the Rx |

# List of Acronyms

| | |
|---|---|
| AC | Asymmetrically Clipped |
| ADC | Analog-to-Digital Converter |
| AFE | Analog Front-End |
| AMP | Amplifier |
| AP | Access Point |
| APD | Avalanche PD |
| AT | Acquisition and Tracking |
| BER | Bit-Error-Rate |
| BPPM | Binary PPM |
| bps | Bit Per Second |
| BW | Bandwidth |
| CCDF | Complementary Cumulative Distribution Function |
| CDMA | Code-Division MA |
| CHL | Correlator with a Hard-Limiter |
| CLD | Chip-Level Detector |
| CN | Coordinator Node |
| COVID-19 | Coronavirus Disease-2019 |
| CP | Cyclic Prefix |
| CSI | Channel State Information |
| DAC | Digital-to-Analog Converter |
| DR | Dynamic Range |
| e-Health | Electronic Health |
| ECG | Electrocardiogram |
| EEG | Electroencephalogram |
| EGC | Equal Gain Combining |
| EMG | Electromyography |
| EMI | Electromagnetic Interference |
| EPA | Expectation Propagation Algorithm |
| ETSI | European Telecommunication Standards Institute |
| FD | Frequency-Domain |
| FDMA | Frequency-Division MA |

| | |
|---|---|
| FEC | Forward Error Correction |
| FER | Frame-Error-Rate |
| FF | Flip-Flop |
| FFT | Fast-Fourier Transform |
| FIFO | First-Input First-Output |
| FLOP | Floating-Point Operation |
| FOV | Field-of-View |
| FPGA | Field-Programmable Gate Array |
| FSO | Free Space Optical |
| GaAs | Gallium Arsenide |
| GaN | Gallium Nitride |
| HBC | Human Body Communications |
| HL | Hard-Limiter |
| HS | Hermitian Symmetry |
| HW | Hardware |
| ICU | Intensive Care Unit |
| IEC | International Electrotechnical Commission |
| IFFT | Inverse-Fast-Fourier Transform |
| ILA | Integrated Logic Analyzer |
| IM/DD | Intensity Modulation and Direct Detection |
| IoMT | Internet of Medical Things |
| IoT | Internet of Things |
| IR | Infrared |
| IRC | IR Communications |
| IrDA | IR Data Association |
| ISI | Inter-Symbol Interference |
| ISM | Industrial Scientific and Medical |
| LD | Laser Diode |
| LED | Light-Emitting Diode |
| LiFi | Light Fidelity |
| LOS | Line-of-Sight |
| m-Health | Mobile Health |
| MA | Multiple Access |
| MAC | Media Access Control |
| MAI | Multiple Access Interference |
| MF | Matched Filter |
| MMSE | Minimum Mean Square Error |
| MPA | Message Passing Algorithm |
| MUD | Multiuser Detection |
| MUSA | Multi-User Shared Access |

| | |
|---|---|
| NB | Narrowband |
| NMAI | No-MAI |
| NOMA | Non-Orthogonal MA |
| O-CDMA | Optical-CDMA |
| O-OFDM | Optical-Orthogonal Frequency-Division Multiplexing |
| O-OFDMA | Optical-Orthogonal Frequency-Division MA |
| O-ROFDMA | Optical Real-valued OFDMA |
| O-SCFDMA | Optical Single-Carrier FDMA |
| OFDMA | Orthogonal FDMA |
| OMA | Orthogonal MA |
| OOC | Optical Orthogonal Code |
| OOK | On-Off-Keying |
| ORWP | Orientation-based RWP |
| OWC | Optical Wireless Communication |
| P/S | Parallel to Serial |
| PAM | Pulse Amplitude Modulation |
| PAN | Personal Area Network |
| PAPR | Peak-to-Average-Power Ratio |
| PC | Prime Code |
| PD | Photo-Detector |
| PDF | Probability Density Function |
| PDMA | Pattern Division MA |
| PHY | Physical |
| PN | Pseudo-Noise |
| PoC | Proof-of-Concept |
| PPM | Pulse Position Modulation |
| PSD | Power Spectral Density |
| PWM | Pulse Width Modulation |
| QoS | Quality-of-Service |
| RF | Radio-Frequency |
| ROC | Random Optical Code |
| RSMA | Resource Spread MA |
| RWP | Random Waypoint |
| Rx | Receiver |
| S/P | Serial to Parallel |
| SAR | Specific Absorption Rate |
| SC | Signature Code |
| SCMA | Sparse-Code MA |
| Si | Silicon |
| SIC | Successive Interference Cancellation |

| | |
|---|---|
| SiPM | Silicon Photomultiplier |
| SmartBAN | Smart Body Area Network |
| SN | Sensor Node |
| SNR | Signal-to-Noise-Ratio |
| TD | Time-Domain |
| TDMA | Time-Division MA |
| TIA | Trans-Impedance Amplifier |
| Tx | Transmitter |
| UV | Ultraviolet |
| UWB | Ultra Wideband |
| UWO | Underwater Wireless Optical |
| VL | Visible Light |
| VLC | Visible Light Communications |
| WBAN | Wireless Body Area Network |
| WH | Walsh-Hadamard |
| WSN | Wireless Sensor Network |

# Chapter 1

# Introduction

**Contents**


**1.1 General Context** . . . . . **9**
1.1.1 Remote Patient Monitoring . . . . . 9
1.1.2 Key Enabling Technologies for Remote Monitoring . . . . . 10
1.1.3 Medical WBANs . . . . . 12
1.1.3.1 Communication Architecture of Medical WBANs . . . . . 12
1.1.3.2 Requirements for Medical WBANs . . . . . 13
1.1.4 Challenges of Existing WBAN Technology . . . . . 15
1.1.5 Interest in Optical WBANs . . . . . 15
**1.2 Thesis Objectives** . . . . . **16**
1.2.1 Thesis Outline . . . . . 19
1.2.2 Thesis Contributions . . . . . 19
1.2.3 Author's Publications . . . . . 20


## 1.1 General Context

### 1.1.1 Remote Patient Monitoring

The increasing rate of chronic health conditions, particularly the rapid growth of such patients with multiple health issues, has created a serious challenge to the healthcare systems. While the majority of chronic diseases are associated with the aging population, an increasing number of children and young adults are also affected, accounting for about 71% of global mortality in 2016, as reported by the World Health Organization [1]. Moreover, postoperative patients are at high risk of clinical deterioration. In such situations, monitoring of patients in hospital wards or intensive care units (ICUs) plays a crucial role in order to minimize major deterioration of health conditions and preventing sudden death.

Traditionally, ICUs are the only facility in hospitals where patients are continuously monitored by attending nursing staff. Unfortunately, no continuous monitoring system is in place when patients are moved outside the ICU, either in a private room or a standard ward. The typical patient

monitoring approach in hospital wards, where nurses assess physiological parameters, e.g., body temperature, blood pressure, and heart rate, manually at an extended interval, poses significant difficulties. Moreover, one major cause of increasing patient mortality in hospitals is the delays in proper treatment or hospitalization due to long wait times in an emergency waiting room [2]. Indeed, timely detection of rapidly changing abnormalities in a patient's health is crucial in order to intervene effectively. This can be achieved by continuous remote monitoring of patients at home, hospital wards or emergency waiting rooms. Additionally, such a telemonitoring system at home will reduce the load on hospitals and health economic burden, while improving the quality of life.

Recently, Coronavirus disease-2019 (COVID-19) has emerged as a global pandemic, affecting millions of lives worldwide. The level of severity of COVID-19 is classified as asymptomatic, mild, moderate, severe, and critical [3]. However, a sudden clinical deterioration might occur, usually within the second week of sickness, resulting in serious health problems, ICU hospitalization, and death. Therefore, continuous monitoring of such patients is crucial in order to detect any abnormalities in health. Moreover, given the severity and rapid spread of the COVID-19, healthcare systems are under severe stress, limiting their ability to provide efficient services to patients. In such cases, the burden on hospitals can be reduced by remote monitoring at home while maintaining a safe distance from COVID-19 patients.

Indeed, the delay in timely detection and intervention of medical conditions could be a matter of life and death for a patient. This is the gap that a continuous remote monitoring system can bridge.

### 1.1.2 Key Enabling Technologies for Remote Monitoring

The recent advances in electronic devices, sensing technology and the internet have already enabled electronic health (e-Health) solutions, and played a key role for remote monitoring to become a reality [4, 5]. The introduction of mobile devices and sophisticated communication technologies have created a new subfield under e-Health known as mobile health (m-Health). Mobile patient monitoring is a type of m-Health service where physiological parameters, i.e., vital signs, of remote patients are monitored continuously [6]. In a remote patient monitoring system, wearable health sensors collect patients' vital signs from the body and transmit them to a remote location, e.g., medical and emergency centers, which simplifies the practice of telemedicine [7]. Recently, due to the COVID-19 crisis, the term telehealth has become a buzzword, and often used interchangeably with telemedicine [8]. However, telehealth represents a broader concept and involves both clinical and non-clinical remote services [9]. The relationship between e-Health, telehealth and remote patient monitoring is illustrated in Fig. 1.1. Note that, in this thesis, we focus on remote patient monitoring, with a particular emphasis on mobile patients.

The remarkable progress in micro-electro-mechanical systems technology has led to the creation of low-powered and tiny sensor nodes. With the help of modern communication and networking technologies, these sensor nodes are used to form a wireless sensor network (WSN) that might work collectively for remote monitoring purposes, e.g., environment, healthcare, smart

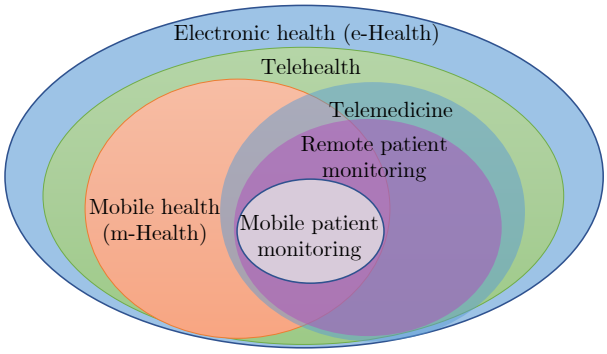


**Figure 1.1:** The e-Health paradigm (reproduced from [6]).

**Table 1.1:** Frequency bands and their bandwidths of IEEE 802.15.6 PHY layers [15].

| PHY layers | Frequency | Bandwidth |
|---|---|---|
| HBC | 16 MHz, 27 MHz | 4 MHz |
| NB | 402-405 MHz, 420-450 MHz | 300 KHz |
| | 863-870 MHz, 956 MHz | 400 KHz |
| | 902-928 MHz | 500 KHz |
| | 2360-2400 MHz, 2400-2438.5 MHz | 1 Mhz |
| UWB | 3.2-4.7 GHz, 6.2-10.3 GHz | 499 MHz |

grids, etc. [10]. A wireless body area network (WBAN) is a subfield of WSNs that employs body sensors for monitoring medical and non-medical (e.g., sport, body posture, location, sleeping) applications wirelessly [11]. The classification of WBANs based on different application scenarios is given in Fig. 1.2 [12]. Compared to the classical WSNs, WBANs have unique requirements, in terms of communication architecture, number of sensors, periodic or non-periodic monitoring, reliability, and patient mobility [13].

The first idea of WBAN dates all the way back to 1996, when Zimmerman introduced the concept of personal area network (PAN), which demonstrated how electronic devices on and around the human body may transfer digital information [14]. The IEEE 802.15.6 communication standard for WBANs was released in 2012 [15], and defined three distinct physical (PHY) layer technologies based on radio-frequency (RF) transmission: narrowband (NB) PHY, ultra wideband (UWB) PHY, and human body communications (HBC) PHY. NB PHY operates on seven different frequency bands, where, in most countries, the MICS (Medical Implant Communication Service) uses the first licensed band of NB PHY within a range of 402-405 MHz for implanted medical device communication. However, the license-free industrial scientific and medical (ISM) band, i.e., the seventh band of NB PHY within a range of 2400-2438.5 MHz, is the most popular choice for wearable devices. Table 1.1 presents the frequency bands and their corresponding bandwidths utilized by different PHY layers of IEEE 802.15.6 WBAN standard.

The majority of works on WBAN found in the literature are based on rather well-known IEEE 802.15.4 (ZigBee) [16–18] and IEEE 802.15.1 (Bluetooth) [19–21] standards. These communica-

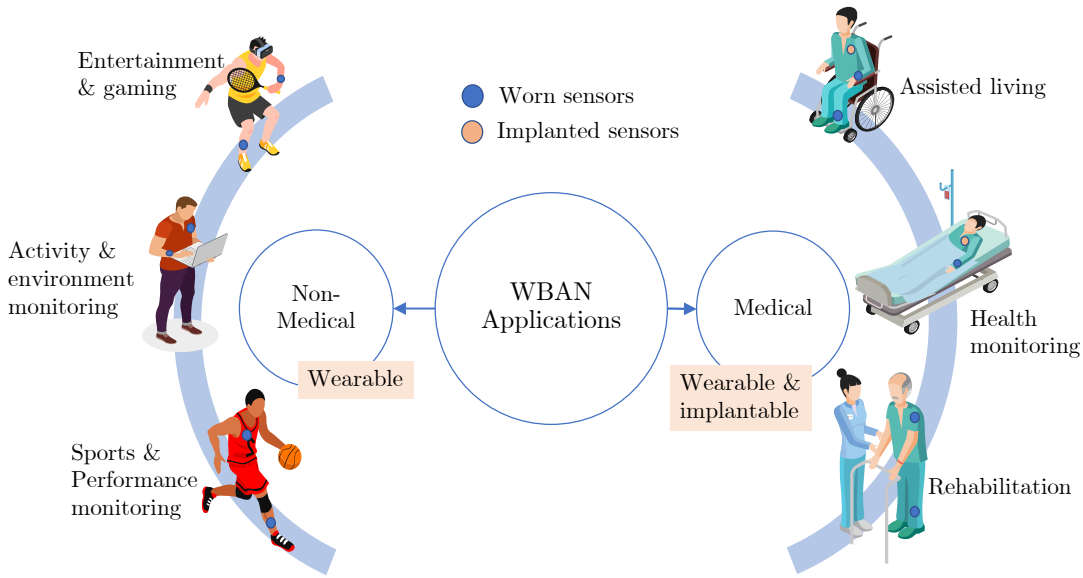


**Figure 1.2:** Different WBAN application scenarios.

tion standards also rely on RF operating in the 2.4 GHz ISM frequency band. Besides, with the concept of internet of things (IoT), the number of connected devices to the internet is growing rapidly [22] and WSN is becoming an integral part of it for wireless connectivity [23]. Using IoT for medical applications, e.g., for remote patient monitoring, is referred to as the internet of medical things (IoMT), including the use of WBANs [24, 25]. To address the issue of IoT and IoMT devices using several communication technologies, European Telecommunication Standards Institute (ETSI) has developed a new WBAN standard in 2018 called smart body area network (SmartBAN), which enables multi-radio wireless connectivity, e.g., Bluetooth, ZigBee, and IEEE 802.15.6, at the same time [26, 27].

### 1.1.3 Medical WBANs

As explained, in a remote patient monitoring system, sensors implanted, placed on or around the patient body communicate through the use of WBANs for real-time continuous monitoring of vital signs from a remote location [28–31]. The WBAN communication architecture and its requirements are defined in the IEEE 802.15.6 standard. ETSI adopted the same architecture for SmartBAN, with an additional option of smart relay coordination control [26]. In what follows, we present the communication architecture, requirements, and challenges of medical WBANs.

#### 1.1.3.1 Communication Architecture of Medical WBANs

Figure 1.3 illustrates the communication architecture of a typical WBAN, where sensor nodes (SNs) placed on a patient's body transmit their data to a coordinator node (CN) (also called hub, here placed on the shoulder of the patient's body), and then the collected medical data from the CN

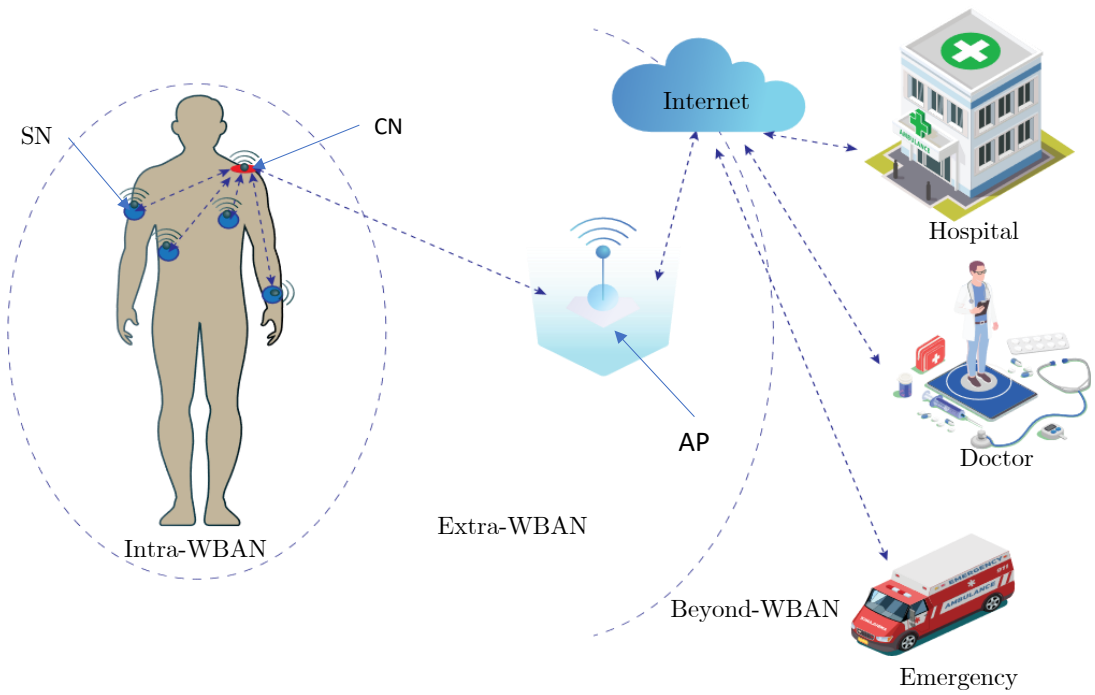


**Figure 1.3:** Communication architecture of a typical WBAN composed of intra-WBAN, extra-WBAN, and beyond-WBAN.

are sent to an access point (AP). Finally, the AP transfers those data to an external network. In a WBAN, from a data transmission point of view, the communication architecture can be divided into intra-WBAN, extra-WBAN, and beyond-WBAN.

- Intra-WBAN concerns the communication between the SNs and the CN [32]. The SNs with their associated CN have a typical transmission range of 1 m in and around the human body [30].
- Extra-WBAN refers to the communication between the CN and an external network or an AP [29, 30, 33]. This AP could be integrated into the infrastructure or strategically deployed in a dynamic environment. Furthermore, several APs may be used to create a mesh network to increase network coverage and enable patient mobility.
- Beyond-WBAN considers the transfer of health monitoring data from the AP to hospitals, doctors or emergency centers, in particular, through the use of the internet [29, 30]. In fact, medical servers may record patients' health information history, which could be accessed and utilized for medical treatment when needed.

#### 1.1.3.2 Requirements for Medical WBANs

WBANs employ a variety of heterogeneous sensors, resulting in data-rate variations depending on the application, which can impose significant complexity to the PHY and media access con-

**Table 1.2:** Data-rate and QoS requirements for some popular medical WBAN sensors, reproduced from [33].

| SNs | Target data rate | Target BER |
|---|---|---|
| Temperature, Glucose | 20 bps | $< 10^{-10}$ |
| Oxygen saturation (SPO2) | 32 bps | $< 10^{-10}$ |
| Blood pressure | < 10 Kbps | $< 10^{-10}$ |
| ECG | 72 Kbps | $< 10^{-10}$ |
| EEG | 86.4 Kbps | $< 10^{-10}$ |
| Cochlear implant | ~ 200 Kbps | $< 10^{-10}$ |
| Endoscope capsule | 1 Mbps | $< 10^{-10}$ |
| EMG | 1.536 Mbps | $< 10^{-10}$ |
| Deep brain stimulation | 128 – 320 Kbps | $< 10^{-3}$ |

trol (MAC) layers. Mobility also puts constraints on energy consumption and transmission link reliability, i.e., quality-of-service (QoS). Moreover, security and privacy requirements for medical applications are among the major concerns.

**1. Data Rate and QoS:** A medical WBAN can use several sensors for monitoring a range of physiological parameters, e.g., electroencephalogram (EEG), electrocardiogram (ECG), electromyography (EMG), blood pressure, temperature, and oxygen saturation (SPO2), resulting in data-rate heterogeneity. The data-rates of those sensors for medical applications range from a few bit per second (bps) up to a few Mbps. Moreover, a high degree of QoS must be assured, which is directly associated with the data transmission reliability. Link reliability usually refers to the guaranteed delivery of a data, i.e., ratio of successfully received and transmitted packets, realized in terms of bit-error-rate (BER). The IEEE 802.15.6 and SmartBAN standards define, in addition, packet delay requirements of up to 250 and 10 milliseconds, respectively, between data packet generation at the MAC layer and successful reception at the CN [15, 26, 34]. Table 1.2 presents several popular medical WBAN sensors along with their typical data-rate and BER requirements. Note that, in any digital communication system, nearly error-free performance (in the sense of very low BER) can be achieved by employing a forward error correction (FEC) coding when the pre-FEC BER is lower than $10^{-3}$ [35].

**2. Power Consumption:** Considering the battery-powered sensing devices, low power consumption is a critical requirement in medical WBANs. In particular, implantable medical devices, e.g., pacemakers and cardiac defibrillators, may require a battery lifetime of at least five years, while some other devices may require battery lifetimes of tens of hours to a few years depending on the application [15,36]. Therefore, special attention should be devoted to the design of energy-efficient signal processing techniques, e.g., the PHY and MAC layers. A popular approach for the latter is the implementation of a duty-cycled MAC, allowing devices to be in sleep mode most of the time [37, 38]. In addition, energy harvesting for WBANs is a growing area of research that considers harnessing energy by using body temperature, vibrations, and the human gait cycle [39, 40].

Note that, another serious concern on energy consumption is that, due to the semi-conductive nature of the body, the energy absorbed by the tissue surrounding the sensors may lead to severe thermal damages. This energy absorption is quantified by the so-called specific absorption rate (SAR), which must comply to both national and international requirements.

**3. Security and Privacy:** The security issue is extremely important when it comes to medical applications since they involve private and confidential health information. Given the limited computational power, size, and energy constraints, an appropriate encryption mechanism must be employed to prevent hacking and to ensure data integrity. Although IEEE 802.15.6 specifies three layers of security, recent research indicates that such authentication and encryption approaches are still vulnerable to different types of attacks [41, 42]. Moreover, RF-based communication technology causes serious security risks for medical WBANs, since it lacks the needed battle-hardening to identify and mitigate RF-borne threats.

### 1.1.4 Challenges of Existing WBAN Technology

As mentioned before, most already proposed RF-based IoT and IoMT networks operate in the shared ISM frequency band, resulting in increased spectrum congestion and electromagnetic interference (EMI), which has been attributed to crucial medical equipment malfunctions in hospitals [43, 44]. Interference in WBANs may occur due to the coexistence of other RF-enabled devices, e.g., Wi-Fi, microwave ovens, WSNs etc., and the coexistence of multiple WBANs, where the former refers to cross-interference and the latter to inter-WBAN interference [45]. In particular, given the very low transmit power in WBANs, interference may severely degrade the system performance [46]. Moreover, in an intra-WBAN network, sensors operating on the same frequency may cause intra-WBAN interference, resulting in increased complexity of the MAC layer to manage it. Also, a recent study shows that, for a given sensor, with the increasing number of neighboring nodes on the body, the SAR increases [47].

Figure 1.4 illustrates the types of interference that may occur in WBANs. Furthermore, as mentioned earlier, such RF-based systems are vulnerable to security breaches and can also be easily jammed [41].

### 1.1.5 Interest in Optical WBANs

Given the above mentioned constraints on RF-based medical WBANs, an interesting alternative is the use of optical wireless communication (OWC) wireless connectivity in these networks [48]. OWCs have recently gained increasing attention and being considered as one of the most promising technologies in 6G for medical use cases and the massive IoT connectivity. In OWC systems, signals can be transmitted using unguided visible light (VL), infrared (IR), or ultraviolet (UV). In fact, the well known visible light communications (VLC) technology is a subset of OWC operating in the VL band, offering communication and illumination simultaneously [49]. Over the last few

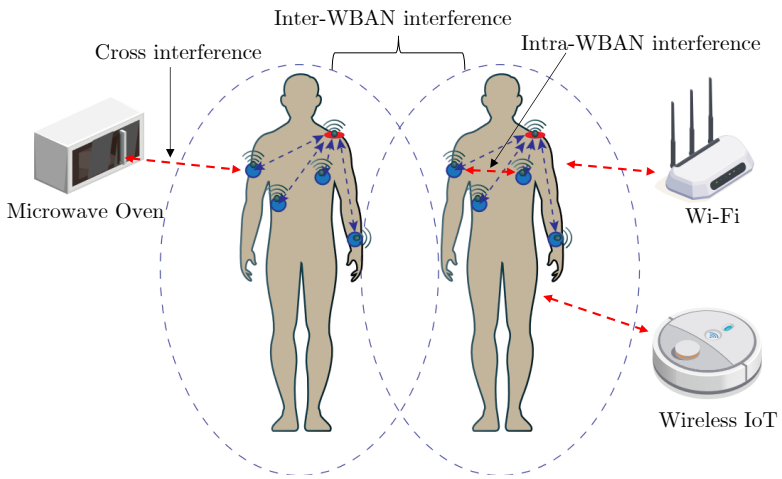


**Figure 1.4:** Illustration of different types of signal interference in medical WBANs.

decades, VLC and IR communications (IRC) have gained popularity, in particular, in indoor application scenarios. Thanks to their ability to deliver high-speed wireless access, usually referred to as light fidelity (LiFi) [50, 51]. As a matter of fact, IRC has been used for short and medium range data transmission dating back to the 80s, even years before the IR data association (IrDA) released the first standard in 1993.

More generally, OWC offers a wide range of applications, including short- and medium-range indoor and outdoor communications [49,52,53], as well as long-range free space optical (FSO) [54] and underwater wireless optical (UWO) [55,56] communications. Typical examples of OWC applications are illustrated in Fig. 1.5. In contrast to RF technologies, OWC systems provide several advantages. They operate in the unregulated and license-free electromagnetic spectrum, resulting in cost free use of optical bands. Furthermore, their immunity against EMI enables interference-free parallel transmission with other communication technologies. OWC systems also provide inherent security features against interception and hacking, since the optical links are usually confined within a room and can not pass through the opaque walls. One significant advantage of OWC is the wide availability of low cost opto-electronic front-ends, which allows relatively straightforward implementation in practice.

Therefore, the use of OWCs in medical WBANs is considered to be an promising approach. The significant operational and technical advantages of light communication led to the creation of first dedicated training program on OWC called “Vision” (2017-2022) [57]. The research work we will present here is a part of the “Vision” project, thanks to the Marie Skłodowska-Curie grant funded by European Union’s Horizon 2020 research and innovation program.

## 1.2 Thesis Objectives

In this thesis, we consider the use of OWC based on VL and IR for remote patient monitoring. In particular, we focus on extra-WBAN links, i.e., communication between a CN placed on the pa-

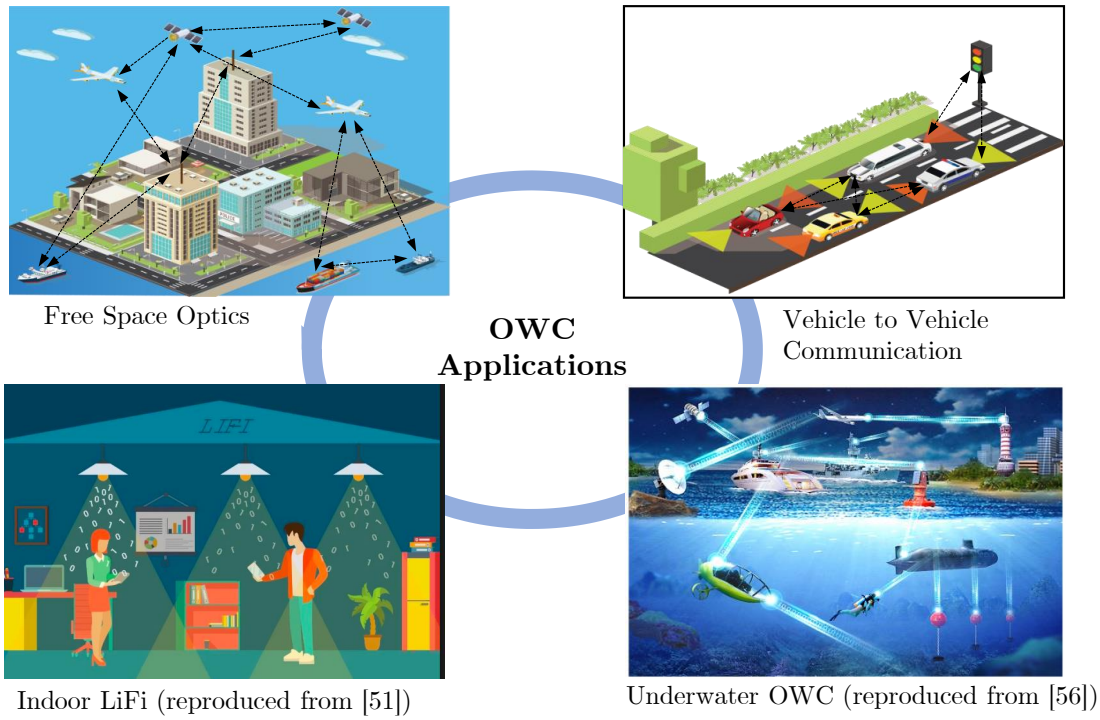


**Figure 1.5:** Examples of OWC applications in indoor and outdoor scenarios.

tient's body and an AP. Concerning intra-WBAN communication, given the constraints discussed in Section 1.1.4 and in order to limit the power consumption, some research proposed wired connectivity in place of wireless in between the on body sensors and the CN [58]. Obviously, this will not restrict patient mobility, as the communication between the CN and the external networks considers wireless connectivity. Additionally, the use of flexible electronic textiles capable of sensing body temperature, heart rate, and respiration rate avoids the need for intra-WBAN wireless connectivity [4, 59, 60]. However, the use of OWC for intra-WBAN wireless connectivity has been also shown a feasible solution recently [32, 61].

We consider the use of IR links for the uplink extra-WBANs, where a CN placed on the patient's body transmits the medical data to an AP. The use of IR rather than VL is to avoid user discomfort and visual annoyance. VL can be used in downlink, i.e., from the AP to the CN probably by using the light-emitting diode (LED) luminaires; this way, the interference between the uplink and downlink can also be avoided [62].

Concerning the IR uplink, one major concern is the eye-safety, which will impose a limitation on the transmit optical power according to the International Electrotechnical Commission (IEC) standard [63]. Then, considering the WBAN requirements, special attention should be devoted to link reliability and power consumption. In particular, mobility of the patients, random transmitter (Tx) orientations, link blockage, and shadowing may impair the link quality significantly.

As a matter of fact, in typical situations, several patients may share a hospital ward, and similarly, few elderly people may need to be monitored at a senior's residence room. Then, simulta-

neous data transmission from multiple patients is unavoidable, which requires the use of appropriate multiple access (MA) techniques. In this context, code-division MA (CDMA), i.e., optical-CDMA (O-CDMA), is a potential MA solution of relatively low implementation complexity that allows asynchronous data transfer [64]. However, it may suffer from multiple access interference (MAI) due to the so-called "near-far" problem, which may lead to a decrease in link reliability. Moreover, due to the required long signature codes (SCs) in O-CDMA, this technique may not be suitable for a large number of patients in a typical emergency waiting room scenario. In such a scenario, an interesting alternative could be the use of the popular optical-orthogonal frequency-division MA (O-OFDMA) [65]. However, O-OFDMA usually comes with relatively high computational complexity, resulting in increased power consumption of the nodes.

The main objective of this thesis is to investigate, design, and develop appropriate modulation and MA schemes for optical transmission in medical extra-WBANs. Considering the low power consumption requirement, here the critical question is how to achieve the needed data transmission reliability while taking into account patient mobility and random Tx orientations in different scenarios. We focus, in particular, on two relevant application scenarios of a hospital ward and an emergency waiting room. To study the reliability of the signaling schemes for an extra-WBAN link, we consider two criteria of BER and outage probability ($P_{\text{out}}$). We mostly focus on the latter as a more appropriate metric for a randomly changing channel. It is defined as the probability that the BER for a given channel realization exceeds a target value, $\text{BER}_{\text{th}}$:

$$P_{\text{out}} = P(\text{BER} \geq \text{BER}_{\text{th}}). \tag{1.1}$$

Note that given the $\text{BER}_{\text{th}}$ of $10^{-3}$, the required QoS for the considered WBAN applications is achieved when $P_{\text{out}}$ is limited to about $10^{-2}$ [66]. In order to achieve these objectives, by focusing on the uplink, we proceed with the following steps:

- Assess the fundamentals of optical wireless transmission in the context of medical WBANs, and study how user mobility may affect the QoS of the optical links.
- Investigate the state-of-the-art MA solutions for medical WBANs, and propose suitable modulation and MA schemes considering WBAN requirements (i.e., reliability, energy efficiency) for different medical scenarios.
- Propose solutions to improve the reliability and power consumption of the transmission schemes.
- Analyze the performance of the proposed solutions taking into account the mobility of patients for hospital ward and emergency waiting room scenarios.
- Design and implement the signaling schemes on the programmable logic and experimentally demonstrate the proof-of-concept (PoC).

### 1.2.1 Thesis Outline

This thesis dissertation is divided into seven chapters, the first one being is this introduction-**Chapter 1**. The remaining chapters are structured as follows:

In **Chapter 2**, we present the fundamentals of optical wireless transmission technology, the employed system components and channel modeling approach for medical WBANs. We provide an overview of the literature on optical WBANs and discuss their practical limitations. We specify the system setup for an extra-WBAN optical link and propose a user mobility model taking into account random Tx orientations.

In **Chapter 3** , we investigate appropriate MA techniques for OWC-based medical WBANs. For this purpose, first we provide a literature review on traditional and cutting-edge MA techniques. Meanwhile, we highlight their implementation challenges for the considered optical WBAN scenarios. Then, we present the detail structures of the potential MA solutions to be employed for optical transmission in medical WBAN applications.

In **Chapter 4** , we analyze the performance of O-CDMA scheme for uplink transmission in extra-WBANs considering a hospital ward scenario. Meanwhile, we investigate and highlight the interest of employing multiple APs. First, we describe the considered hospital ward scenario, O-CDMA signaling scheme model, and the mathematical formulations in order to evaluate the performance. Then, we present the performance analysis results and show the improvement achieved by using multiple APs.

In **Chapter 5**, we propose a new O-OFDMA based scheme that does not need any Hermitian symmetry (HS) constraint to meet the intensity modulation and direct detection optical transmission requirement. We investigate the performance of the proposed scheme compared to the conventional orthogonal schemes in terms of peak-to-average-power ratio and BER. Finally, we show the suitability of the scheme for an emergency waiting room scenario managing relatively a large number of users.

In **Chapter 6**, we develop a PoC of the proposed O-CDMA based extra-WBAN system and experimentally investigate its performance. First, we provide the implementation details of the analog front-ends and field-programmable gate array prototypes. Then, we experimentally investigate the performance of the implemented system in terms of BER and frame-error-rate managing MAI.

Finally, **Chapter 7** concludes the thesis and provides some perspectives for future extension of this work.

### 1.2.2 Thesis Contributions

The main contributions of this thesis are summarized as follows:

- Studying the O-CDMA performance using accurate and realistic channel modeling for a hospital ward scenario; Elucidating the limitation of its performance in mobility conditions due

to the near-far problem.

  - Quantifying the O-CDMA link performance degradation due to line-of-sight (LOS) link blockage with the presence or absence of MAI; Showing the contribution of the diffuse link.
  - Demonstrating the substantial improvement in the link performance and data transmission reliability by using multiple APs.

- Proposing a HS-free O-OFDMA signaling scheme called optical real-valued OFDMA (O-ROFDMA) for the extra-WBAN uplink by transmitting only the real part of the time-domain (TD) signal.

  - Performance comparison of the proposed scheme with alternative MA schemes considering realistic characteristics of the opto-electronic components.
  - Demonstrating the suitability of the proposed O-ROFDMA scheme for the emergency waiting room scenario, and its relatively low computational complexity.
  - Elucidating the MAI effect in the O-ROFDMA scheme due to clipping noise; Studying its performance taking into account LOS link blockages due to random Tx orientations in the absence and presence of MAI.

- Investigating the implementation of an O-CDMA system for extra-WBAN in medical application.

  - Designing and Implementing the system on a field-programmable gate array (FPGA) and proposing an analog front-end (AFE) for the transmission and reception of the optical signal; Evaluating the performance of the implemented system in managing the MAI.

### 1.2.3 Author's Publications

**Conferences**

- M. J. Hasan, M. A. Khalighi and B. Béchadergue, "*Experimental Implementation of Optical-CDMA for Medical Extra-WBAN Links*," International Symposium on Communication Systems, Networks and Digital Signal Processing (CSNDSP), pp. 1-6, Porto, Portugal, July 2020.

- M. J. Hasan, M. A. Khalighi, L. N. Alves and B. Béchadergue, "*Impact of Synchronization Errors on the Performance of ACO-OFDMA Signaling for Medical Extra-WBAN Links*," IEEE International Symposium on Personal Indoor and Mobile Radio Communications (PIMRC), Helsinki, Finland, Sept. 2021.

**Journals**

- M. J. Hasan, M. A. Khalighi, J. García-Márquez and B. Béchadergue, "*Performance Analysis of Optical-CDMA for Uplink Transmission in Medical Extra-WBANs,*" in IEEE Access, vol. 8, pp. 171672-171685, Sept. 2020.
- M. J. Hasan, M. A. Khalighi, V. Jungnickel, L. N. Alves and B. Béchadergue, "*An Energy-Efficient Optical Wireless OFDMA Scheme for Medical Body-Area Networks,*" in IEEE Transactions on Green Communications and Networking, Submitted, Sept. 2021

# Chapter 2

# Optical Transmission for Medical WBANs

**Contents**


**2.1 Introduction** . . . . . **23**
**2.2 Optical Wireless Signal Transmission** . . . . . **24**
2.2.1 Transmitter . . . . . 24
2.2.1.1 LEDs . . . . . 25
2.2.1.2 Laser Diodes . . . . . 27
2.2.2 Receiver . . . . . 28
2.2.2.1 PIN Photo-diode . . . . . 28
2.2.2.2 APDs . . . . . 29
2.2.3 Indoor Optical Channel . . . . . 29
2.2.3.1 Link Configurations . . . . . 29
2.2.3.2 Signal Transmission Formulation . . . . . 31
2.2.4 Modulation Technologies . . . . . 31
2.2.4.1 Pulse-Based Modulations . . . . . 32
2.2.4.2 Multi-Carrier Modulations . . . . . 33
**2.3 Channel Modeling for Optical WBANs** . . . . . **33**
2.3.1 Channel Propagation Model . . . . . 34
2.3.2 Modeling User Mobility . . . . . 35
2.3.2.1 Tx Orientation . . . . . 36
2.3.2.2 ORWP Model . . . . . 37
**2.4 Chapter Summary** . . . . . **38**


## 2.1 Introduction

The objective of this chapter is to review the fundamentals of OWC in order to realize optical transmission for medical WBANs. Therefore, we present an overview of OWC system components, their possible configurations, and challenges. Meanwhile, we identify the most suitable optical sources and photo-detectors, and their arrangements, i.e., the placement of the CN and AP for the uplink extra-WBANs. We also describe the modeling of patients' mobility and random Tx orientations.

For this, in Section 2.2, we describe a typical OWC system and review the optical sources, receivers, optical link configurations, and modulation schemes. We explain that the IR LEDs are best suited for uplink WBANs, as compared to other types of optical sources, i.e., laser diodes (LDs). Moreover, we compare the characteristics of different photo-detectors and highlight the interest of using a PIN photo-diode in our application. Then, we present different arrangements of the CN and AP, and discuss the potential channel limiting factors, such as user mobility and background noise. We also briefly review the typical modulation schemes, including pulse-based and multi-carrier modulations. Obviously, channel modeling is a prerequisite to the design of a wireless communication system. Hence, in Section 2.3, we review the channel modeling approaches of OWC. To consider the effect of random Tx orientations due to mobility of patients, based on random waypoint (RWP) mobility, we present a generalized orientation-based RWP (ORWP) mobility model. Lastly, Section 2.4 concludes the chapter, outlining the considered optical WBAN system parameters and description.

## 2.2 Optical Wireless Signal Transmission

Figure 2.1 presents the generalized block diagram of a typical OWC system. As with any conventional wireless communication system, it is composed of three parts: the Tx, the propagation channel, and the receiver (Rx). At the Tx, the information bits to be transmitted are probably encoded and then modulated, and then converted to an electrical signal by passing through a digital-to-analog converter (DAC). Then, the signal passes through a driver circuit before being fed into an optical source, where the latter converts the electrical signal into an optical signal. Note that, in the context of indoor OWC, non-coherent optical sources are often the preferred choice. Therefore, only intensity modulation and direct detection (IM/DD) is possible, i.e., the electrical signal must be strictly positive, which is usually achieved by adding a DC component before driving the source. Also, optional optics may be placed after the optical source to control its field of emission. Then, the generated optical signal propagates through the wireless indoor channel. At the Rx, the optical signal is collected by a photo-detector (PD), that may also be equipped with photon collecting optics. Then the resulting photo-current is converted to a voltage by a trans-impedance amplifier (TIA) circuit before being sampled by an analog-to-digital converter (ADC). Finally, the original transmitted bits are recovered by signal demodulation and decoding.

In this section, we briefly explain the different components of the OWC system presented above and review the existing optical sources and PDs. We also discuss optical link configurations and the modulation schemes that are widely used for indoor optical transmission.

### 2.2.1 Transmitter

The key advantages of OWC in our application are its relatively low cost optical front-ends, its suitability for short-range links, and resilience to EMI and interference from adjacent rooms. Nevertheless, special attention should be devoted to eye and skin safety, which limits the transmit

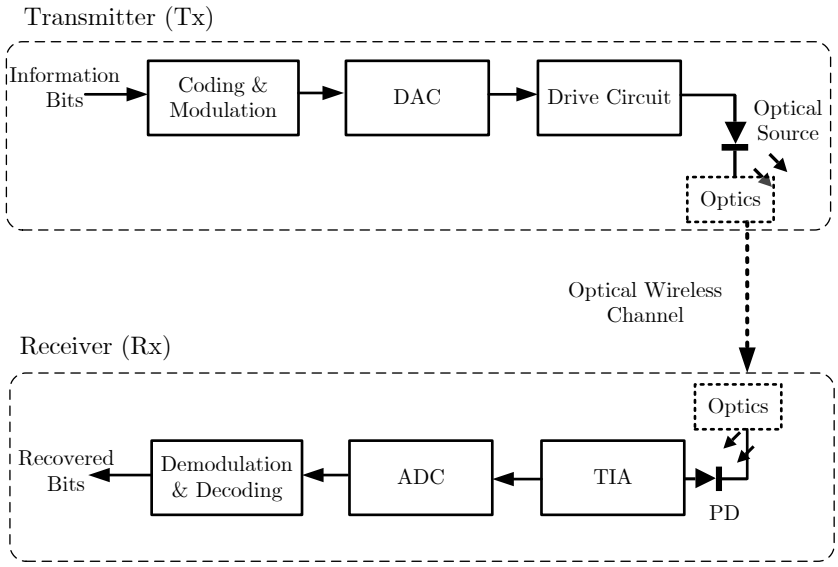


**Figure 2.1:** General representation of a typical OWC system.

power as well as the types of optical sources that can be employed.

Semiconductor optical sources, such as LEDs and LDs, are the most popular choices in OWC. These optical sources may be manufactured to emit light across a wide range of electromagnetic spectrum from VL to IR. In order to determine the suitability of LEDs or LDs for use in optical WBANs, hereafter, we review their characteristics, merits, and limitations.

#### 2.2.1.1 LEDs

An LED is a two-terminal semiconductor device that emits light when its p-n junction is activated by applying a forward bias voltage. The recombination of electrons and holes produces non-coherent light typically by spontaneous emission of photons. In terms of illumination, in contrast to the conventional incandescent light sources, LEDs offer a number of benefits such as, lower power consumption, compact size, longer operational life, better thermal management, and a better physical resilience [67]. Also, LEDs are environmentally beneficial since they contain no mercury and have a minimal health effect due to their low UV radiation.

Typically, LEDs used for illumination are classified as white and RGB, where the former may use yellow phosphors in combination with a blue LED to emit white light. For the latter, based on their colors, different types of epitaxial layers are grown on a bare wafer made of materials such as sapphire, gallium nitride (GaN), silicon (Si), or gallium arsenide (GaAs). For instance, the epi wafers made of AlGaAs and InGaN may produce IR and blue light, respectively [67][1].

When used for data communication, due to the slow response time of the yellow phosphorous, white LEDs have modulation bandwidths smaller than 10 MHz [68], whereas IR LEDs can have

[1] Note that, Al and In stand for the aluminium and indium, respectively.

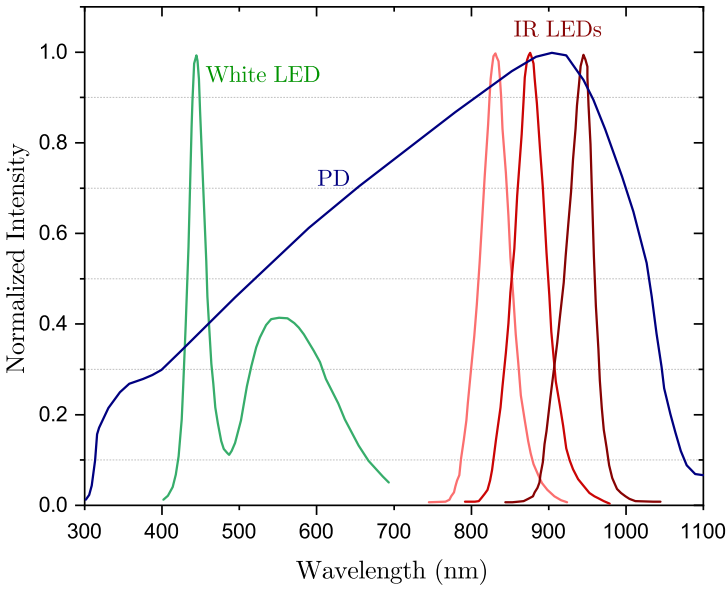


**Figure 2.2:** Spectral responses of a white LED, IR LEDs with center wavelengths of 830 nm, 870 nm, and 950 nm, and a typical PIN PD, reproduced from [70].

bandwidths of up to 35 MHz [69]. Additionally, IR LEDs outperform VL LEDs in terms of photodetection sensitivity, as shown in Fig. 2.2.

The use of IR LEDs for wireless data communication goes back to the 1980s, when IBM researchers developed the first IR LED-based wireless connected network between distributed computers [71]. In [72], Barry *et al.* pioneered the theoretical foundations for indoor OWC based on IR LEDs. Meanwhile, in 1962, Holonyak *et al.* invented the first LED (low-intensity red) in the VL spectrum [73]. However, it was not until 1990 that Nakamura *et al.* demonstrated the first blue LED, which laid the groundwork for modern white LEDs [74], replacing the energy-hungry incandescent light sources. In 2000, Nakagawa *et al.* employed white LEDs for data communication, referred to as VLC, offering communication and illumination simultaneously [75, 76]. Since then, significant research has been conducted demonstrating the feasibility of establishing bidirectional indoor VLC [77–80].

Employing white LEDs in the both uplink and downlink imposes number of difficulties, e.g., the problem of interference between optical links. Proposed solutions include time division duplexing and the use of distinct color LEDs for bidirectional links [79, 81]. Nevertheless, in the claimed LiFi application scenarios, where LED-based luminaires are used as APs, the use of VL in the uplink, i.e., from a device to the AP on the ceiling, could be unpleasant for the users. One possible solution is to use an IR link for uplink [82, 83]. For the same reason, we chose IR uplink transmission in our application of medical WBAN.

Considering here IR LEDs as Tx, one major concern is the eye-safety limitation. In fact, such

emitters are safe from any health hazard as long as they satisfy the photobiological safety requirements imposed by IEC. For example, according to the IEC-62471 standard, for pulsed IR, a cornea exposure irradiance limit of 100 W/m2 and a retina exposure radiance limit of 545.5 mW/mm2/sr have likely no eye hazard at a distance of 200 mm [63].

Compared to LDs, one major advantage of LEDs is their relatively wider beam width, which allows the use of relatively higher optical powers, enabling the link ranges of a few meters and user mobility. Moreover, LEDs show less temperature dependency as compared to LDs [70].

#### 2.2.1.2 Laser Diodes

Similar to an LED, an LD is a semiconductor device formed by a p-n junction, which can be pumped directly to convert an electrical signal into an optical signal. However, unlike an LED, an LD produces coherent light by stimulated emission of photons, which means they have a constant relative phase.

LDs are the most common sources employed in UWO and FSO communications for many years [52, 54, 56, 84, 85]. However, growing interest in high-speed applications has motivated the consideration of LDs as promising optical sources for indoor OWCs because of their high modulation bandwidth and better electrical-to-optical power efficiency [86]. For instance, in [87], Tsonev *et al.* studied the feasibility of LDs for high-rate applications at standard indoor illumination levels. In [88], Watson *et al.* reported the use of 422 nm Gallium-nitride LDs for indoor VLC and demonstrated 2.5 Gbps data-rate with a sensitivity of 11.5 dBm. In [89], Lee *et al.* achieved 4 Gbps data-rate employing RGB LDs in indoor VLC system. In [90], Hussein *et al.* employed LDs with an imaging receiver in a realistic indoor mobile scenario and reported minimum 5 Gbps data-rate. Recently, in [91], Wei *et al.* built a full-duplex indoor OWC system where an IR vertical cavity surface emitting laser is used for uplink. They experimentally achieved 2.125 Gbps data-rate from a distance of 2.2 m.

The major concern while employing LDs in WBAN applications is eye- and skin-safety. For point source lasers, the IEC-60825 classified safety standard based on transmit power, where Class 1, limited to only 0.2 mW, is intended for indoor applications and considered safe under all conditions [92]. LEDs, on the contrary, may transmit at much higher power, typically ranging from 250 to 750 mW tailored to the operational wavelength [86], due to their reasonably large area and wide emission angle.

However, an LD can be used for WBAN applications demanding higher data-rates. In such a case, an optical diffuser should be inserted in front of the LD to break its spatial coherence, allowing relatively high transmit power ($\sim$ 100 mW) while satisfying the eye-safety requirement. Nevertheless, such diffusers may attain efficiencies maximum of 70 %, and the resulting Tx would be more expensive and bulkier, compared to the case of using an LED. As a matter of fact, LDs are nearly 10 times more expensive compared to their LED counterparts [93].

**Table 2.1:** Typical characteristics of the different PD technologies, reproduced from [97, 98].

| Characteristic | PIN PD | APD | SiPM |
|---|---|---|---|
| Spectral range (nm) | 320 – 1100 | 200 – 1150 | 320 – 900 |
| Gain | 1 | < 100 | $<10^5 - 10^6$ |
| Response time | Fast | Slow | Fast |
| Operating voltage | 5 V | 100-200 V | <50 V |
| Form factor | Small | Small | Small |
| Temperature sensitivity | Low | High | Low |
| Noise | Low | Medium | Low |
| Cost | Low | High | Low |

### 2.2.2 Receiver

Given the mobility of patients in a typical medical WBAN scenario, OWC Rxs are expected to have a relatively large field-of-view (FOV) to capture as much optical signal as possible. Nevertheless, a larger Rx FOV will also result in collecting more ambient light, i.e., background noise. Moreover, given the IR transmission in the uplink, due to the limited transmit power imposed by the eye-safety concerns, photo-detection sensitivity is crucial in the considered application. Generally, two types of optical Rxs can be employed to receive the transmitted signal by the LED luminaires: a PD or a camera sensor [94]. However, camera sensors can only accommodate a very limited data throughput due to their low sampling frequency. For PDs, their spectral range, low noise, faster response time, low cost, and high internal gain influence their choices. The most common PDs in OWC systems are the PIN PD and the avalanche PD (APD). Recently, the use of silicon photomultipliers (SiPMs) has gained attention as an interesting and highly sensitive alternative [95]. A SiPM is a multi-pixel photon counter, where each pixel is an APD biased in Geiger mode [96]. A comparison of the main characteristics of PIN PD, APD, and SiPM are provided in Table 2.1.

Here, we focus on the PIN PD and APD options in order to determine their suitability for our considered application, as discussed in the following.

#### 2.2.2.1 PIN Photo-diode

A PIN PD consists of a lightly doped intrinsic layer sandwiched between two layers of heavily doped p-type and n-type semiconductor materials. Based on operating wavelength, different semiconductor materials may be used to fabricate PIN PDs. For instance, Si is used for the spectral range of 320 to 1100 nm, GaAs for the range of 650 to 870 nm, and InGaAs for the range of 900 to 1700 nm [48, 98]. Given the requirement of operating spectral wavelength in the VL and IR regions, Si PIN PDs are the most appropriate choice in this context. Moreover, due to their relatively low operating bias voltage, low temperature sensitivity, high photosensitivity, and low capacitance (i.e., fast response time), they are widely adopted for OWC applications.

Compared with an APD, the use of a PIN PD allows a less expensive and a less bulky Tx with simpler electronics, and furthermore less sensitivity to background illuminations. For instance,

in [99], Haddad *et al.* analyzed the performances of optical intra-WBAN links using PIN PDs and showed better performance for relatively high background noise level compared to their APD counterparts.

#### 2.2.2.2 APDs

APDs are structurally quite similar to PIN PDs, with the exception that they improve sensitivity through the process called impact ionization, resulting in increased internal gain. APDs have several advantages, including high gain and relatively high photon conversion efficiency.

In the context of OWC, APDs have been considered in several works, particularly for long-distance communications and low-level signaling [100–102]. However, a high bias voltage is required for the ionization process. Moreover, the gain of the APD is highly sensitive to the temperature and bias voltage variations, and thus requires complex circuitry to ensure temperature and voltage stability. Additionally, in the presence of non-negligible background radiations, APDs are shot noise limited [103].

### 2.2.3 Indoor Optical Channel

The quality of the communication channel significantly affects the performance of optical transmission systems. Many factors influence the indoor OWC channel, such as room dimension, Tx angle of emission, link range, Rx FOV, link configurations, and background noise.

#### 2.2.3.1 Link Configurations

Kahn and Barry defined indoor OWC links based on the presence of a LOS link between the Tx and the Rx, as well as the degree of directionality [52]. The most typical link configurations are: directed LOS, non-LOS or diffuse, and hybrid.

In the context of optical WBANs for uplink, given the mobility of patients and battery powered Tx (i.e., the CN), the placement of the CN and link configurations are crucial. We consider that the CN is placed on the shoulder of each patient, which has been shown in [104] to be an appropriate choice due to the patient comfort and also the relatively high probability of having a LOS connection with the AP (i.e., Rx), typically placed on the ceiling.

In what follows, considering uplink transmission in medical WBANs, we describe different possible link configurations, as illustrated in Fig 2.3, as well as their advantages and limitations.

**1. Directed LOS:** Figure 2.3a illustrates a directed LOS link, where the CN and AP are pointing towards each other. Typically, this setup is equipped with a narrow-beam LED at the Tx and a Rx with a relatively small FOV, which is ideal for point-to-point communication, particularly for high data-rate applications. Due to narrow FOV at the Rx, directed LOS links are robust to multi-path distortion and less affected by ambient noise sources. However, in order to address user mobility,

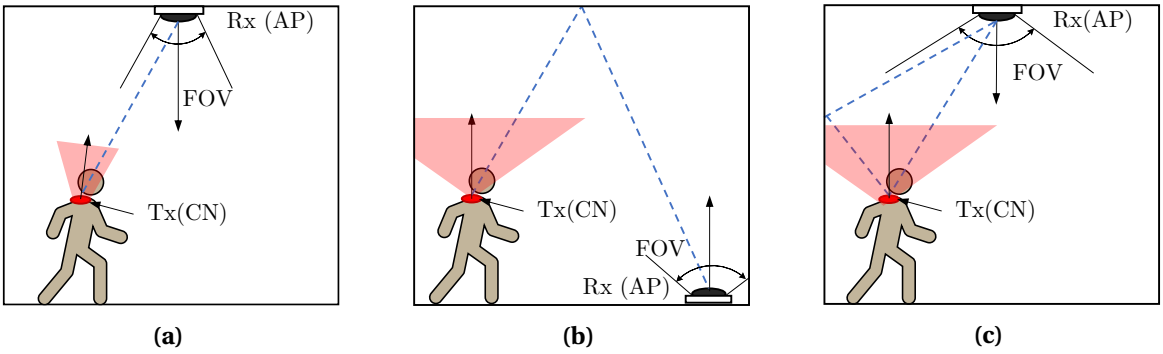


**Figure 2.3:** Link configurations for indoor optical extra-WBANs: (a) directed LOS, (b) non-LOS, (c) hybrid link. The Tx is placed on the shoulder of the patient.

this configuration may require a complex tracking mechanism to maintain an uninterrupted LOS link between the Tx and Rx.

In the context of optical WBANs, the effect of patients' mobility inside a hospital room was studied in [105], while assuming a half-tracked LOS link between a medical sensor and an AP. Such a half-tracked link is, however, still complex to implement as it requires a fine knowledge of the user and AP positions to align the Tx with the Rx.

**2. Non-LOS:** For a non-LOS link, also known as diffuse link, no optical direct link exists between the Tx and Rx. Typically, both Tx and Rx are oriented towards the ceiling, and the Rx with a wide FOV collects diffusely reflected optical signal from the ceiling, as shown in Fig. 2.3b. The advantages of this configuration include resistance to link blockage and good support of mobility. However, diffuse links suffer from significant path loss, which is further exacerbated in a situation called shadowing, where the strongest link paths are blocked by any means, e.g., a person or furniture in the room. Moreover, channel multipath dispersion may result in inter-symbol interference (ISI), which will require channel equalization at the Rx. Additionally, transmission in a relatively large room needs the use of relatively high transmit power.

Therefore, considering the eye-safety concerns for uplink IR in medical WBANs, we do not recommend diffuse configuration for medical WBANs, particularly, for the room dimensions provided in the health-building guidelines for hospitals [106]. Note that, in [107], nevertheless diffuse link configuration was considered for medical WBANs for a relatively small hospital room of dimension $3 \times 4 \times 2.5\,\mathrm{m}^3$.

**3. Hybrid:** The hybrid link configuration includes contributions from both the LOS and diffuse components, as shown in Fig. 2.3c. This is probably the most widely used configuration due to its high energy efficiency and low implementation complexity. It requires a wide-angle LED at the Tx and a Rx with a relatively large FOV, where reliable communication can be achieved in mobility condition by using diffusely reflected links when the LOS link is not available due to blockage.

Several studies have considered hybrid link configuration in optical WBANs to transmit med-

ical data from the patient's body. For example, in [108], the authors achieved the required QoS by employing the hybrid link setup for IR-based uplink extra-WBAN transmission. In [109], Haddad *et al.* analyzed hybrid link channels under mobility conditions for extra-WBANs. In [110], Kaba *et al.* studied the performance of a optical body sensor taking into account both the LOS and diffuse contributions, and also analyzed the effect of user mobility in [111].

In this thesis, taking into account the requirement of implementation simplicity and communication reliability, we consider the hybrid link configuration for the medical data transmission in extra-WBAN uplink.

#### 2.2.3.2 Signal Transmission Formulation

Regardless of the link configurations described in the previous subsection, the IM/DD baseband signal at the Rx (without any optical concentrator), i.e., the generated instantaneous photocurrent $y(t)$ at the Rx PD, can be written as [52]:

$$y(t) = \mathscr{R} r(t) \otimes h(t) + n(t), \tag{2.1}$$

where $\mathscr{R}$ is the PD responsivity, $r(t)$ is the optical transmitted power, $h(t)$ represents the channel impulse response, $\otimes$ denotes convolution, and $n(t)$ refers to the Rx noise.

Considering a PIN PD, the main sources of noise are dark current noise, thermal noise, and shot noise. Dark current noise is the random variations of the leakage current induced by the bias voltage applied to the PIN PD. The shot noise is caused by random variations in the generated photo-current at the PD, due to both received signal and ambient radiations [103]. Thermal noise is mainly generated by the load resistance of the Rx TIA. Neglecting the signal-generated shot noise, remaining noise sources are modeled as signal-independent zero-mean white Gaussian with the one sided noise power spectral density (PSD) $N_0$ [49, 52]. Therefore, denoting the total Rx noise variance by $\sigma_n^2$, we have $\sigma_n^2 = BN_0$, where $B$ refers to the Rx bandwidth. Note that the dominant noise sources are background and thermal noises [103].

### 2.2.4 Modulation Technologies

For medical WBANs, a low-complex and energy-efficient modulation scheme should be used, achieving the required QoS. Note that the choice of a modulation technique may also be influenced by the MA solutions used to serve multiple users in a communication network. In contrast to RF systems, IM/DD based OWC systems do not suffer from multipath fading due to the large size of PDs (typically in cm) compared to the nm range wavelength [112]. The most straightforward approach is the use of pulse-based modulation schemes, e.g., on-off-keying (OOK). However, more advanced multi-carrier modulation techniques have gained increasing attention.

In the sequel, we provide a brief description of the most popular modulation technologies used in OWC. We will later discuss the architecture and performance analysis based on considered MA and modulation schemes in Chapters 3, 4, and 5.

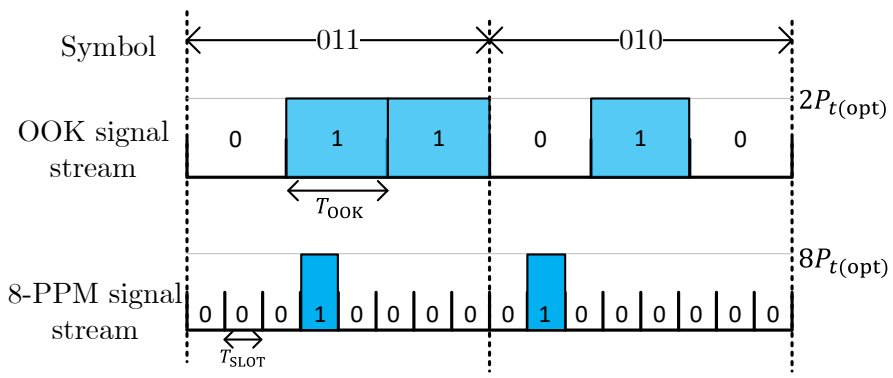


**Figure 2.4:** Example of bit-symbol mapping in OOK and 8-PPM signaling scheme.

#### 2.2.4.1 Pulse-Based Modulations

Pulse-based modulation schemes include OOK, pulse position modulation (PPM), pulse width modulation (PWM), and multi-level pulse amplitude modulation (PAM). OOK can be regarded as PAM with two intensity levels. Compared to the binary modulation schemes, multi-level modulations are more sensitive to noise [48]. Moreover, PWM has a relatively low energy efficiency [113]. Therefore, considering the low power requirements of WBANs, we focus on the OOK and PPM signaling schemes. An example of bit-symbol mapping is presented in Fig. 2.4, where ON and OFF slots are represented by bits '1' and '0', respectively.

**A. OOK Signaling:** OOK is the most widely used modulation scheme due to its simple hardware requirement. The OOK signals can be transmitted in two modes: non-return-to-zero and return-to-zero, where the former represents the bit '1' with an ON pulse that equals the bit duration, and for the latter, the pulse occupies only a part of the bit duration. Here, we consider the non-return-to-zero OOK signaling, as illustrated in Fig. 2.4. Now, denoting the average optical transmit power by $P_{t(\text{opt})}$, the transmit optical power per ON slot is $2P_{t(\text{opt})}$. Also, the required bandwidth is equal to the data-rate $R_b$, $R_b = 1/T_{\text{OOK}}$; $T_{\text{OOK}}$ refers to the OOK symbol duration.

OOK signaling scheme has been considered in many commercial OWC systems, e.g., IrDA [114]. It has been widely used in optical WBANs as a basic modulation scheme. For instance, in [115], authors achieved data-rate of 500 Kbps using OOK modulation.

**B. PPM Signaling:** The interest of PPM as compared to OOK is its better power efficiency and the fact that it does not require any adaptive thresholding for signal detection at the Rx [116]. However, it has a lower bandwidth efficiency. An example of 8-PPM signaling compared to OOK is illustrated in Fig. 2.4. Here, denoting the PPM symbol and slot duration by $T_{\text{PPM}}$ and $T_{\text{slot}}$, respectively, we have $T_{\text{slot}} = T_{\text{PPM}}/8$ for 8-PPM signaling. Also, the average optical transmit power per ON slot corresponds to $8P_{t(\text{opt})}$.

Given the low data-rate transmission of medical WBANs, an alternative approach is the use

of binary PPM (BPPM) due to its relatively small bandwidth penalty, and no need for adaptive thresholding as in OOK. We will later provide detailed structure of BPPM signaling along with MA technique in Chapter 4.

#### 2.2.4.2 Multi-Carrier Modulations

Multi-carrier modulation techniques have recently gain growing interest for high data-rate OWC applications mainly to deal with the limited bandwidth of opto-electronic components. The optical-orthogonal frequency-division multiplexing (O-OFDM) is one of the efficient modulation schemes addressing channel frequency selectivity [117–119], while outperforming simple modulation techniques such as OOK in terms of energy efficiency [120]. O-OFDM is also adjustable to manage multi-user access through frequency multiplexing, i.e., O-OFDMA, by allocating distinct subcarriers to each user. We will later describe in more detail the O-OFDMA scheme in Chapter 3.

## 2.3 Channel Modeling for Optical WBANs

Accurate channel modeling is crucial for the design of an OWC system. Several simulation-based approaches have been developed so far to characterize and model the OWC channel mainly for static scenarios [121]. For instance, the works in [112, 122–124] calculated the optical channel impulse response based on ray-tracing methods. However, they suffer from high computational complexity with increased number of reflections. A more popular method is to employ relatively faster Monte Carlo ray tracing [125–128]. Most of these methods have been verified using IR LEDs by experimental measurements, e.g., in [129–131]. Channel modeling for optical WBANs using Monte Carlo ray tracing approach was considered in [109, 132].

An important point here is to consider the effect of user mobility. For instance, it was shown in [133] that the quality of an RF-based extra-WBAN link is significantly affected by mobility. Moreover, the effect of random Tx orientations due to mobility may further impair the link performance. A considerable effort has been made on the channel characterization of optical extra-WBAN links, considering the mobility of patients. In [62, 66, 134], the mobility was considered assuming uniformly distributed random positions of the patient, where the patient body was modeled as volume of rectangular surfaces. Recently, In [32], a more realistic three-dimensional animation of the patient's walk cycle was modeled and characterize the optical intra-WBAN links using the non-sequential ray-tracing function of Zemax. However, the body has a rather little impact on the link performance for relatively low data-rate applications, provided that the $P_{\text{out}}$ requirement is limited to about $10^{-2}$ [66]. Therefore, for the sake of simulation simplicity, the detailed modeling of the patient body can be avoided.

In this section, we describe the mathematical model of the channel propagation for the considered hybrid OWC link configuration. Moreover, we present the user mobility model taking into account random Tx orientations.

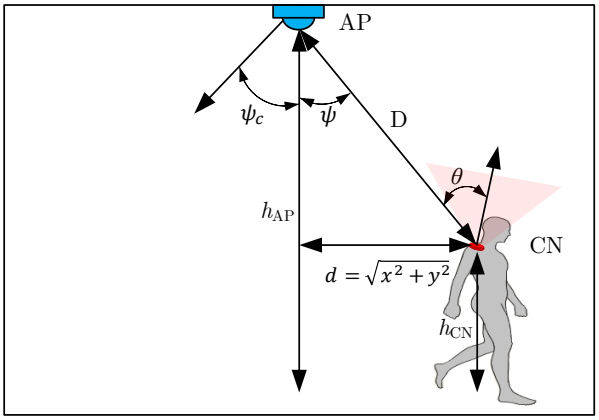


**Figure 2.5:** Illustration of a typical LOS link configuration between a CN and the AP. $x$ and $y$ represent the coordinates of the CN with respect to the room center, i.e., the AP position.

### 2.3.1 Channel Propagation Model

Considering a Lambertian radiation pattern for the LED at the Tx (i.e., the CN), and denoting the channel DC gain for the LOS link by $H_{\text{LOS}}$, we have [52]:

$$H_{\text{LOS}} = \begin{cases} \frac{A_{\text{PD}}(m+1)}{2\pi D^2} \cos^m(\theta)\cos(\psi) & ; 0 \le \psi \le \psi_c \\ 0 & ; \psi > \psi_c, \end{cases} \tag{2.2}$$

where $\psi$ denotes the beam incident angle at the Rx, $A_{\text{PD}}$ is the PD's area, $\psi_c$ denotes the FOV of the Rx (i.e., the AP), and $D$ is the LOS link distance between the CN and the AP, as shown in Fig. 2.5. We have $D = \sqrt{d^2 + (h_{\text{AP}} - h_{\text{CN}})^2}$, where $h_{\text{CN}}$ and $h_{\text{AP}}$ stand for the heights of the CN and the AP, respectively. Also, $d$ is the distance between the CN and the AP, and $\theta$ is the radiance angle of the Tx that depends on the elevation angle $\theta_{tx}$ as shown in Fig. 2.6. Moreover, $m$ in (2.2) is the Lambertian order, related to the LED semi-angle at half power $\phi_{1/2}$ [48]:

$$m = \frac{-\ln 2}{\ln(\cos\phi_{1/2})}. \tag{2.3}$$

Concerning the diffuse link, we denote by $H_{\text{ref}}$ the channel DC gain component corresponding to the signals collected from the beam reflections at the Rx. To avoid too timely simulations, here only 1$^{\text{st}}$-order reflections are taken into account. Note that this choice is practically rational as most non-LOS contributions correspond to the first-order reflections [135]. To calculate $H_{\text{ref}}$, we consider a set of small Lambertian reflecting surface elements, each one with area $A_E$ and reflectivity coefficient $\rho$, as shown in Fig. 2.6. For each element $E_\iota$, the corresponding channel DC gain is given by [52, 136]:

$$H_{\text{ref},\iota} = \begin{cases} \frac{(m+1)\rho A_{\text{PD}} A_E}{2\pi^2 D_1^2 D_2^2} \cos^m(\partial)\cos(\vartheta)\cos(\delta)\cos(\psi') & ; 0 \le \psi' \le \psi_c \\ 0 & ; \psi' > \psi_c, \end{cases} \tag{2.4}$$

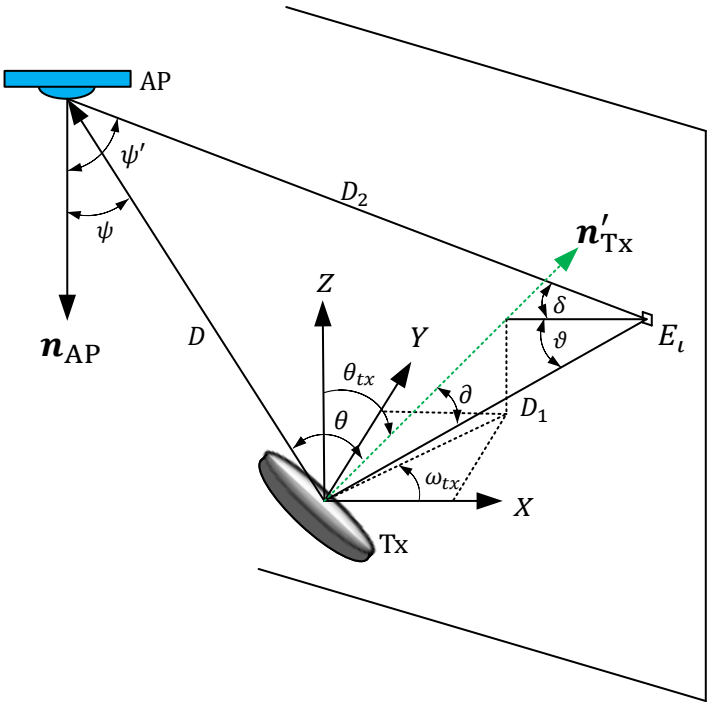


**Figure 2.6:** LOS and diffuse link with randomly oriented Tx. Here, $\theta_{tx}$ denotes the elevation angle, $\omega_{tx}$ is the azimuth angle, and $\boldsymbol{n}_{\mathrm{AP}}$ and $\boldsymbol{n}'_{\mathrm{Tx}}$ stand for the normal vectors corresponding to the AP and Tx, respectively.

where $D_1$ denotes the distance between the Tx and the reflecting surface element $E_\iota$, $D_2$ is the distance between $E_\iota$ and the Rx, $\partial$ is the radiance angle of the Tx, $\vartheta$ expresses the incident angle on $E_\iota$, $\delta$ is the radiance angle of the reflected rays from $E_\iota$, and $\psi'$ denotes the incident angle at the Rx, as shown in Fig. 2.6.

Given the average transmit optical power $P_{t(\mathrm{opt})}$, the total received power $P_r$ on the PD taking into account both LOS and the diffuse links is given by [48]:

$$P_r = \left(H_{\mathrm{LOS}} + \sum_{\iota} H_{\mathrm{ref},\iota}\right) P_{t(\mathrm{opt})}. \tag{2.5}$$

### 2.3.2 Modeling User Mobility

A variety of mobility models have been proposed so far in the context of cellular mobile networks such as random walk model [137], RWP [138, 139], random group model [140–142], and random trip model [143]. In the context of RF extra-WBANs, a modified RWP, called random room mobility model, was proposed in [133] for the case of mobility within a hospital building. Moreover, [144] showed that the human walk nature in outdoor follows the levy-walk model. In indoor environments, RWP is the most widely used mobility model because of being more realistic and its implementation simplicity [145]. In the case of OWC, in addition to user mobility, the effect of Tx orien-

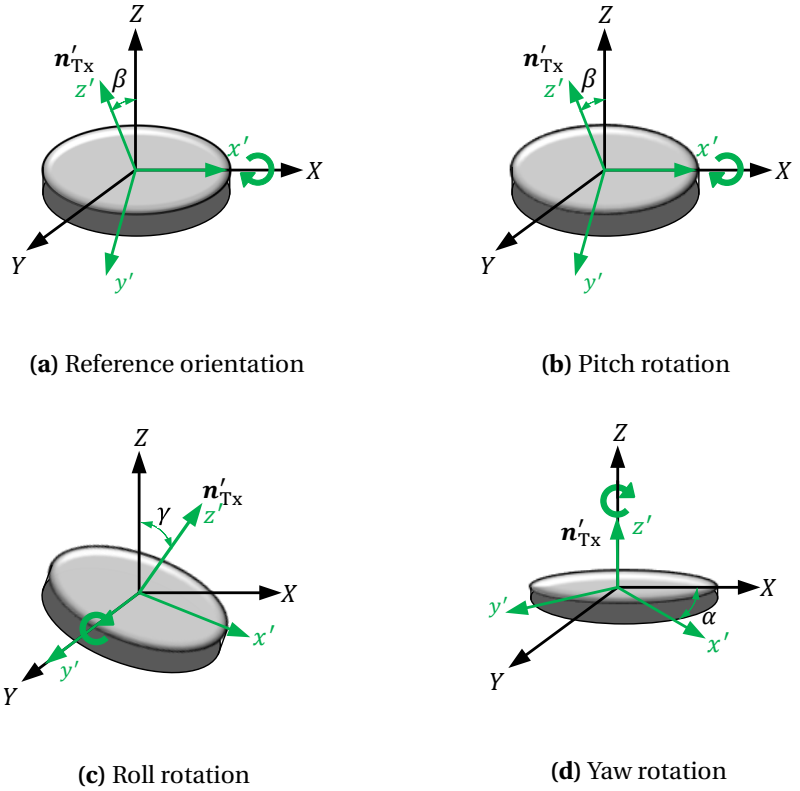


**(a)** Reference orientation

**(b)** Pitch rotation

**(c)** Roll rotation

**(d)** Yaw rotation

**Figure 2.7:** Orientations of a Tx: (a) reference orientation, when the reference coordinate system $XYZ$ and the actual Tx coordinate system $x'y'z'$ are aligned, (b) Pitch rotation, the Tx rotation around the $X$ axis with angle $\beta$, (c) Roll rotation, the Tx rotation around the $Y$ axis with angle $\gamma$, (d) Yaw rotation, the Tx rotation around the $Z$ axis with angle $\alpha$.

tations on the link performance can be quite significant. Recently, an ORWP mobility model was proposed for the LiFi use cases, where mobile devices were considered to be oriented randomly with a Gaussian distribution [146]. Although in our case of extra-WBAN link, the Tx (placed on the patient's shoulder) would have smaller orientation variations, compared to the case of handheld devices in LiFi applications, here for the sake of modeling simplicity, we also consider the Gaussian distribution and use it in our ORWP mobility model.

#### 2.3.2.1 Tx Orientation

The orientation of a Tx placed on a patient's shoulder can be described by the Euler's rotation theorem [147]. We denote the yaw, pitch, and roll angles by $\alpha$, $\beta$, and $\gamma$, respectively. Let's define the reference coordinate system $XYZ$, corresponding to when the Tx is pointing straight towards the ceiling, in contrast to the actual coordinate system $x'y'z'$, see Fig. 2.7. Any spatial orientation can be represented by a $3 \times 3$ rotation matrix $\boldsymbol{R}$ given by [148]:

$$\boldsymbol{R} = \boldsymbol{R}_{\text{yaw}}(\alpha)\,\boldsymbol{R}_{\text{pitch}}(\beta)\,\boldsymbol{R}_{\text{roll}}(\gamma) = \begin{bmatrix} \cos\alpha & -\sin\alpha & 0 \\ \sin\alpha & \cos\alpha & 0 \\ 0 & 0 & 1 \end{bmatrix} \begin{bmatrix} 1 & 0 & 0 \\ 0 & \cos\beta & -\sin\beta \\ 0 & \sin\beta & \cos\beta \end{bmatrix} \begin{bmatrix} \cos\gamma & 0 & \sin\gamma \\ 0 & 1 & 0 \\ -\sin\gamma & 0 & \cos\gamma \end{bmatrix}, \tag{2.6}$$

where $\boldsymbol{R}_{\text{yaw}}$, $\boldsymbol{R}_{\text{pitch}}$ and $\boldsymbol{R}_{\text{roll}}$ are the rotation matrices about the $Z$, $X$ and $Y$ axes with rotation angles $\alpha$, $\beta$, and $\gamma$, respectively. Let us define the normal vectors $\boldsymbol{n}_{\text{Tx}} = [n_x n_y n_z]^T$ and $\boldsymbol{n}'_{\text{Tx}} = [n'_x n'_y n'_z]^T$ corresponding to before and after Tx rotation, respectively, where $(\cdot)^T$ denotes transposition. According to the Euler's theorem,

$$\boldsymbol{n}'_{\text{Tx}} = \boldsymbol{R}\boldsymbol{n}_{\text{Tx}}. \tag{2.7}$$

We assume that the reference and the actual Tx coordinate systems are initially aligned so that $\boldsymbol{n}_{\text{Tx}} = [0\,0\,1]^T$, see Fig. 2.7a. Then, substituting $\boldsymbol{R}$ from (2.6) in (2.7), we have:

$$\boldsymbol{n}'_{\text{Tx}} = \begin{bmatrix} \sin\alpha\,\sin\beta\,\cos\gamma + \cos\alpha\,\sin\gamma \\ \sin\alpha\,\sin\gamma - \cos\alpha\,\cos\gamma\,\sin\beta \\ \cos\beta\,\cos\gamma \end{bmatrix}. \tag{2.8}$$

Now, we convert the rectangular coordinates to spherical coordinates as shown in Fig. 2.6 to obtain the elevation $\theta_{tx}$ and the azimuth $\omega_{tx}$ angles as follows:

$$\theta_{tx} = \arccos\left(\cos\beta\,\cos\gamma\right) \tag{2.9}$$

$$\omega_{tx} = \arctan\left(\frac{\sin\alpha\,\sin\gamma - \cos\alpha\,\cos\gamma\,\sin\beta}{\sin\alpha\,\sin\beta\,\cos\gamma + \cos\alpha\,\sin\gamma}\right). \tag{2.10}$$

Note that the radiance angle $\partial$ in Fig. 2.6 depends on the elevation $\theta_{tx}$ and the azimuth $\omega_{tx}$ angles, and can be calculated by employing the trigonometry of the rectangular triangles (see in Appendix A).

#### 2.3.2.2 ORWP Model

According to the RWP mobility model, within a rectangular room of area $W' \times L'$, the distance between two random points is assumed to be distributed uniformly with the probability density function (PDF) $\frac{1}{W'L'}$ [149]. For the transition between two successive points, the trajectory is a straight path with a constant speed, as illustrated in Fig. 2.8. The PDF of the distance or the transition length between two points, denoted by $\mathscr{S}$ can be found in [149]. For the case of an $L' \times L'$ square room that we will consider later, the expected transition length is $E\{\mathscr{S}\} = 0.5214L'$ [149, 150], where $E\{\cdot\}$ refers to the expected value. The two dimensional PDF of the node location $(x, y)$ is then [150]:

$$f_{XY}(x, y) = \frac{36}{L'^6}\left(x^2 - L'^2/4\right)\left(y^2 - L'^2/4\right). \tag{2.11}$$

Here, we assume that the speed of the node (i.e., the user) is uniformly distributed between $V_{\text{min}}$ and $V_{\text{max}}$, which is considered to be unchanged during each transition. Then, the expected value of the transition time $\mathscr{T}$ is [150]:

$$E\{\mathscr{T}\} = \frac{\ln(V_{\text{max}}/V_{\text{min}})}{V_{\text{max}} - V_{\text{min}}} E\{\mathscr{S}\}. \tag{2.12}$$

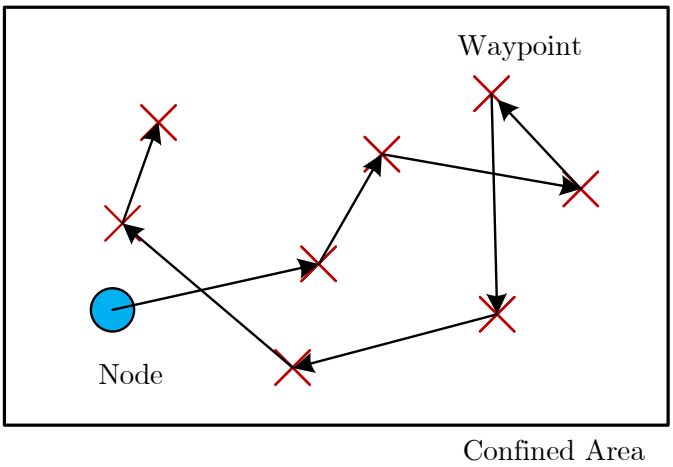


**Figure 2.8:** Illustration of RWP mobility model for a node within a confined area.

We consider the user movements with a certain amount of pause time $\mathcal{T}_p$ with the probability of pause, $P_{\text{Pause}} = E\{\mathcal{T}_p\}/(E\{\mathcal{T}_p\} + E\{\mathcal{T}\})$ [150]. The random location of the paused nodes is assumed to be uniformly distributed with the PDF $f_{XY}^{\text{Pause}}(x, y) = \frac{1}{W'L'}$. The global PDF of the node location taking into account the pause feature will be then:

$$f_{XY}^{\text{Global}} = P_{\text{Pause}}\, f_{XY}^{\text{Pause}}(x, y) + (1 - P_{\text{Pause}})\, f_{XY}(x, y), \tag{2.13}$$

where $f_{XY}(x, y)$ corresponds to (2.11).

Now, to simulate the general ORWP mobility for a given user, for each waypoint, we consider an independently generated random Tx orientation to the user's location using (2.13).

## 2.4 Chapter Summary

In this chapter, we presented a typical indoor optical transmission system and detailed its basic parts and the optical propagation channel. Taking into account the medical WBAN context, we reviewed the issues related to the Tx and Rx components and their arrangements. Based on the considered link setup, we also presented channel modeling approach and mobility model for patient's movements. Meanwhile, we specified the general assumptions for later use, as summarized in the following:

- At the Tx (i.e., the CN):
  - IR LED
  - Intensity modulation
- Optical channel:
  - No body model; neglecting link blockage by obstacles

  - User mobility with ORWP model and random Tx orientations

- At the Rx (i.e., the AP):
  - Si PIN PD; no optical concentrator
  - Direct detection

- Configurations:
  - CN placed on the shoulder
  - AP placed on the ceiling
  - Hybrid link configuration, i.e., LOS and non-LOS components.

# Chapter 3

# Multiple Access Solutions for Optical WBANs

**Contents**


**3.1 Introduction** . . . . . **41**
**3.2 Conventional MA Solutions** . . . . . **42**
3.2.1 Orthogonal MA Solutions . . . . . 42
3.2.1.1 FDMA . . . . . 43
3.2.1.2 TDMA . . . . . 43
3.2.1.3 CDMA . . . . . 44
3.2.1.4 OFDMA . . . . . 45
3.2.2 Non-orthogonal MA Solutions . . . . . 47
3.2.2.1 Power-domain NOMA . . . . . 47
3.2.2.2 Code-domain NOMA . . . . . 48
**3.3 MA Candidates for Optical WBANs** . . . . . **49**
3.3.1 O-CDMA . . . . . 49
3.3.1.1 O-CDMA Based on Unipolar Codes . . . . . 50
3.3.1.2 O-CDMA Based on Bipolar Codes . . . . . 50
3.3.2 O-OFDMA . . . . . 51
3.3.2.1 DCO-OFDMA . . . . . 51
3.3.2.2 ACO-OFDMA . . . . . 53
3.3.3 O-SCFDMA . . . . . 53
3.3.3.1 DCO-SCFDMA . . . . . 53
3.3.3.2 ACO-SCFDMA . . . . . 53
**3.4 Chapter Summary** . . . . . **54**


## 3.1 Introduction

As outlined in Chapter 1, we consider the two cases where several patients in a typical hospital ward or a large number of patients in a typical emergency waiting room need to be monitored

simultaneously. Signal transmission in these cases should use an efficient MA solution that allows several patients to share the same communication channel for the transfer of their medical data. In this chapter we review the state-of-the art MA techniques, taking into account the aforementioned medical scenarios.

In Section 3.2, we provide an overview of conventional MA solutions, and their pros and cons for the considered application scenarios. Considering asynchronous data transmission and hardware simplicity requirements of medical WBANs, we show the suitability of the O-CDMA technique compared to the time-division MA (TDMA) and frequency-division MA (FDMA) counterparts. We further show that in a typical emergency waiting room scenario with potentially a large number of patients, orthogonal FDMA (OFDMA)-based solutions are preferable. On the other hand, non-orthogonal MA (NOMA) schemes based on power- and code-domain multiplexing have recently gained significant attention in cellular networks for massive IoT connectivity. Thus, we briefly review the state-of-the-art NOMA techniques and investigate their advantages and limitations in our context. We show that power-domain NOMA is not suitable for medical WBANs, due to its dependency on the channel gains, given the possibility of closely placed patients and the random nature of channels. Moreover, we compare several code-domain NOMA techniques and highlight their advantages and drawbacks. Next, in Section 3.3, we describe in detail the potential MA candidates for medical WBANs, considering the two scenarios of the hospital ward and emergency waiting room. Lastly, the chapter is summarized in Section 3.4.

## 3.2 Conventional MA Solutions

MA techniques can be divided into orthogonal MA (OMA) and NOMA, where the former allocates users with different frequency or time resources or attributes to them orthogonal signatures (codes) [151]. On the other hand, NOMA allows multiple users to simultaneously use all the time-frequency resources via power- or code-domain multiplexing, where signal detection at the Rx side is typically done based on successive interference cancellation (SIC) [152, 153]. Note that, the majority of existing works on MA schemes for OWC are derived from RF.

In this section, we present a brief overview of OMA and NOMA schemes, and discuss their advantages and drawbacks for the considered WBAN application scenarios.

### 3.2.1 Orthogonal MA Solutions

An OMA scheme uses orthogonal resources for each user signal to minimize the multi-user interference. Typical widely used OMA schemes are FDMA, TDMA, CDMA, and OFDMA.

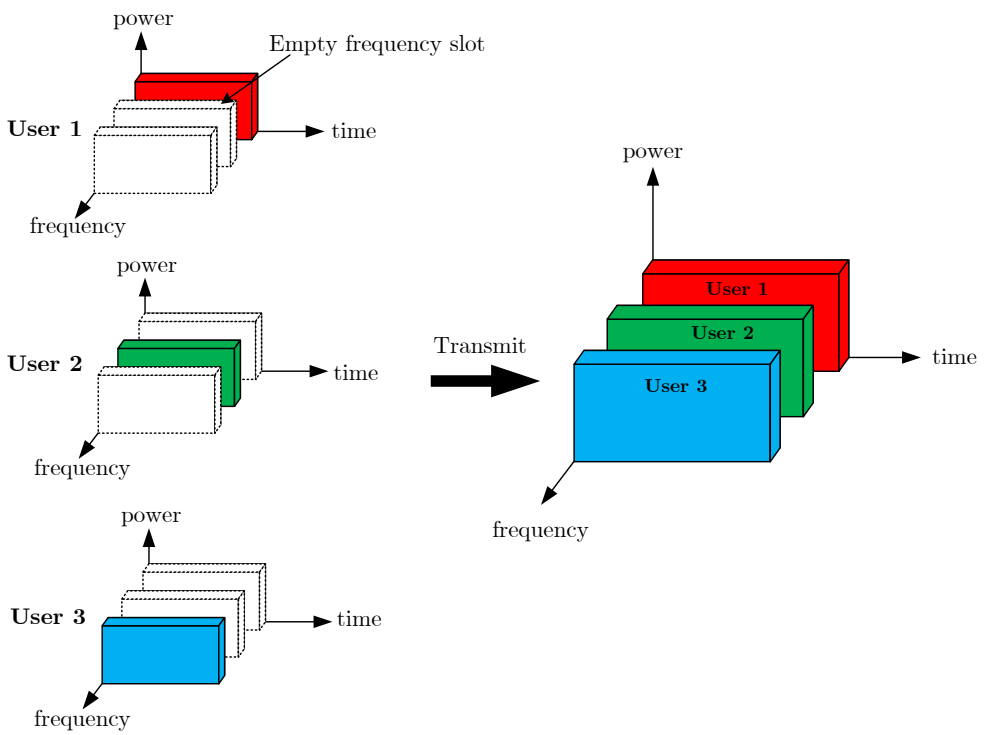


**Figure 3.1:** Resource allocation by FDMA considering three users in the uplink where each user is assigned a unique frequency band.

#### 3.2.1.1 FDMA

In FDMA, each user is assigned a non-overlapping unique frequency band to transmit its data, as depicted in Fig. 3.1. FDMA was, for instance, used in the first generation of cellular networks.

The primary drawback of FDMA is its inefficiency in utilizing entirely the available spectrum bandwidth, as guard bands are used to prevent inter-channel interference. Moreover, in its basic form, it requires bandpass filters in order to avoid adjacent channel interference, resulting in increased system cost.

#### 3.2.1.2 TDMA

By allocating distinct time slots for different users, TDMA enables multi-user access. In TDMA, the users transmit sequentially, i.e., one after another, each in its own time slot, as illustrated in Fig. 3.2. The main advantage of TDMA is its relatively low implementation complexity.

In the context of OWC-based WBANs, different variants of TDMA techniques including time-hopping, and periodic- and priority-based data transmission were proposed for multiple-patient monitoring [154–156]. However, these solutions do not support asynchronous data transmission from different patients. Moreover, their complexity increases with increased number of users, due to the synchronization requirement of TDMA.

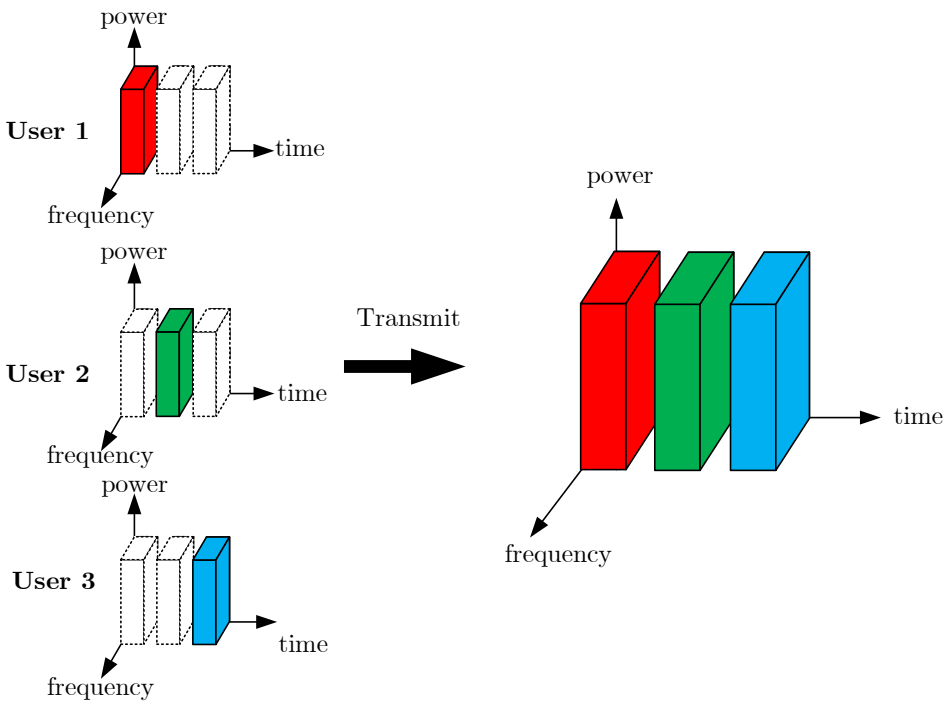


**Figure 3.2:** Resource allocation by TDMA in the uplink. Here, three users transmit data at their assigned time slots.

#### 3.2.1.3 CDMA

In CDMA, each user is assigned a unique SC, allowing users to communicate at the same time and use the whole bandwidth, as shown in Fig. 3.3. Here, signals can be recovered in two ways of single-user or multi-user detection, where the former recovers the desired user signal by considering other interfering users as noise. The latter employs optimal maximum likelihood or linear zero-forcing or minimum mean square error (MMSE) algorithms in order to jointly recover the signals of multiples users [157].

The performance of CDMA is significantly influenced by the type of SCs employed. Conventional RF-based CDMA uses pseudo-random or pseudo-noise binary sequences that are random in nature but can be replicated deterministically. They have good correlation properties, make it efficient to distinguish received signals from different users and mitigate MAI [158]. However, due to the IM/DD nature of signal transmission in OWC systems, bipolar SCs cannot be applied directly. One solution is to modify SCs to meet the OWC requirement, i.e., conversion of bipolar codes to unipolar by replacing “-1” into “0”. Alternatively, specific unipolar SCs are designed for use in optical CDMA (i.e., O-CDMA). Later, in Section 3.3, we will briefly review most popular SCs and the O-CDMA signaling scheme.

In comparison to TDMA, one major advantage of O-CDMA is that it allows asynchronous data transfer simultaneously from multiple users. Moreover, since O-CDMA requires a simple Tx hardware, it is a good MA candidate for uplink WBANs.

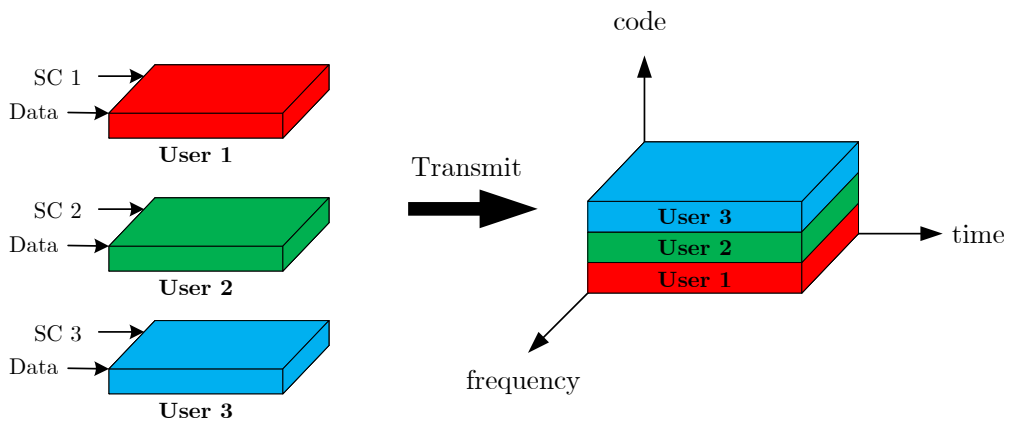


**Figure 3.3:** Resource allocation by CDMA considering three users in the uplink. Each user is assigned a unique SC.

The performance of O-CDMA was experimentally investigated for indoor optical wireless local-area networks in [159], [160]. The authors in [161] and [162] considered the impact of ambient noise on the diffuse IR O-CDMA channel. Also, the near-far problem and MAI effect on a diffuse IR uplink were studied in [163, 164]. In [105], O-CDMA was proposed for uplink transmission in medical extra-WBAN applications for a few number of patients, where the effect of patients' mobility inside a hospital room was studied as well, while assuming a half-tracked LOS link between a medical sensor and an AP. However, as mentioned before, such a half-tracked link is impractical and rather complex to implement. On the other hand, for intra-WBAN medical applications, the analytical study of a diffuse O-CDMA link was presented in [107, 132] based on a so-called hard-limiter (HL) Rx structure.

#### 3.2.1.4 OFDMA

OFDMA is a multi-user version of the widely used OFDM modulation that is, for instance, adopted in the fourth generation cellular networks in the downlink. In OFDMA, each user is assigned a subset of subcarriers before transmission. To reduce ISI, a cyclic prefix (CP) is further inserted in between time symbols, as illustrated in Fig. 3.4.

In the context of OWC, considering IM/DD, to obtain a real-valued TD signal by O-OFDM, HS is imposed on the transmitted frequency-domain (FD) signal frame. Given that the transmit signal must be strictly positive before modulating the optical source, i.e., the LED, a DC-bias is further added to the signal before lower clipping; what is usually called DCO-OFDM. Alternatively, asymmetrically clipped (AC)O-OFDM can be used, which consists in modulating only the odd subcarriers and zero-clipping the negative TD signal [165], resulting in a spectral efficiency loss of factor 2, compared to DCO-OFDM [166]. Since O-OFDMA is a natural extension of O-OFDM, it retains all of the advantages of O-OFDM discussed in Chapter 2.

One of the main issues with O-OFDM signaling is the relatively high peak-to-average-power

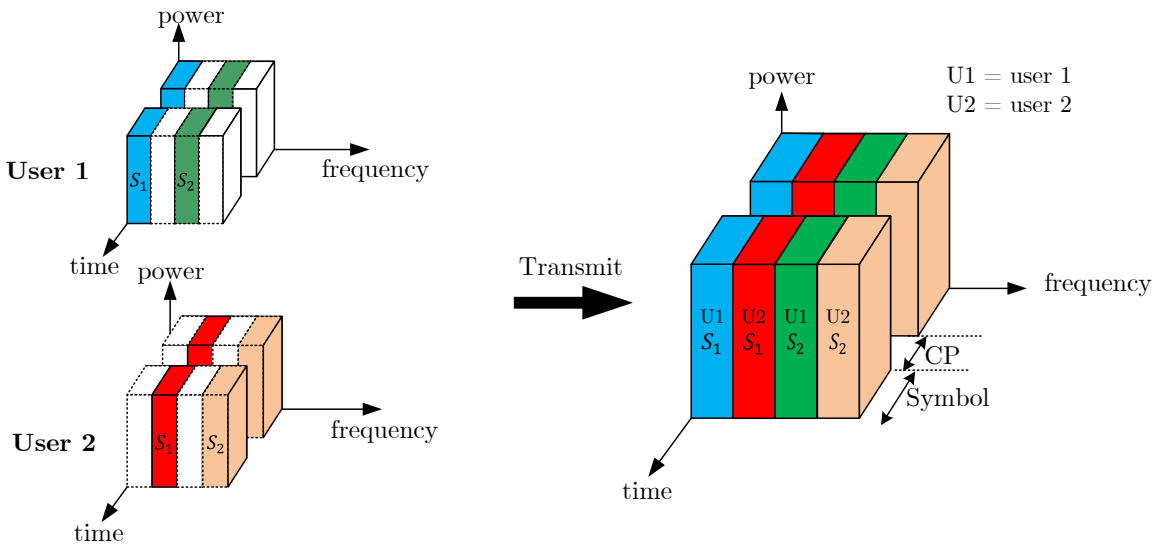


**Figure 3.4:** Resource allocation by OFDMA considering two users in the uplink. Here, $S_1$ and $S_2$ refer to the symbol 1 and symbol 2, respectively.

ratio (PAPR) of the modulated signal given the limited dynamic range of the optical front-ends [167–169]. In fact, in order to avoid the LED from over-heating due to the high signal peaks, the transmit signal is further upper clipped [170]. The resulting signal distortion due to lower and upper clipping is usually modeled by considering the so-called clipping noise. Several solutions have been proposed so far to reduce the PAPR of an O-OFDM signal, based on techniques such as block coding, selective mapping, and pilot assisted transmission, usually at the cost of increased system complexity [171, 172]. As concerns the MA solution, an alternative approach to O-OFDMA is the so-called optical single-carrier FDMA (O-SCFDMA) [173]. In fact, SCFDMA has been adopted in the LTE standard as the uplink MA scheme due to its low PAPR [174, 175]. Note that, compared to OFDMA, additional precoding is required at the Tx side when using SCFDMA, which results in a relatively high computational complexity. The conceptual diagram of SCFDMA is illustrated in Fig. 3.5, where a single carrier is used to transmit users' signals. Detailed description of O-OFDMA and O-SCFDMA signaling will be later presented in Section 3.3

As mentioned before, in a typical emergency waiting room scenario, a large number of patients may need to be monitored simultaneously. The already proposed O-CDMA for few number of patients suffers from high implementation complexity with the increased number of patients due to the required long SCs. Also, using long SCs in O-CDMA results in reduced data-rate due to the limited LED modulation bandwidth.

Last but not least, considering battery-powered CNs, power consumption is a crucial aspect in our application, which depends on the computational complexity and the transmit power. It is therefore of practical interest to design an energy-efficient MA technique for uplink extra-WBAN links.

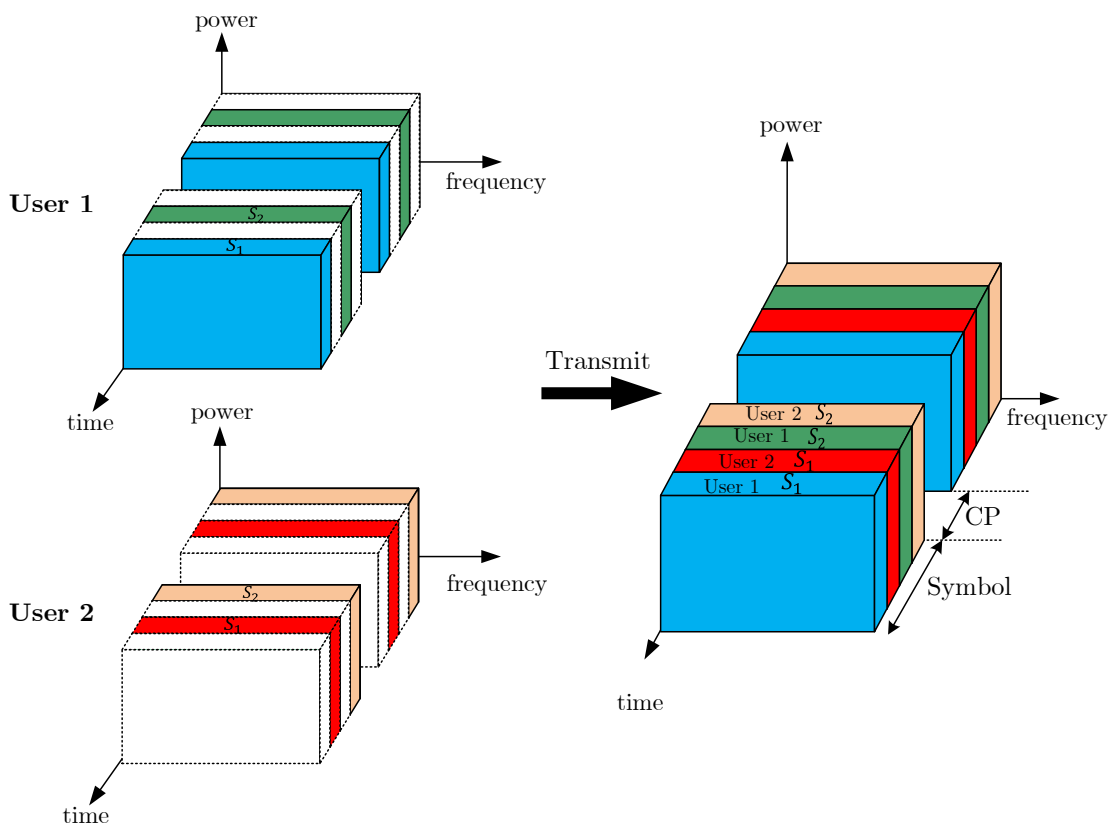


**Figure 3.5:** Resource allocation by SCFDMA considering two users in the uplink. Here, $S_1$ and $S_2$ refer to the symbol 1 and symbol 2, respectively.

### 3.2.2 Non-orthogonal MA Solutions

Recently, NOMA has attracted extensive attention for massive IoT connectivity with the requirement of low latency and long battery life and for future generation of cellular networks [153]. Massive connectivity is achieved in NOMA by permitting signal to overlap over the same time-frequency bands via power-domain or code-domain multiplexing. NOMA could be an interesting MA option in the context of WBANs, particularly for the case of emergency waiting room scenario. Therefore, in the following, we briefly describe NOMA techniques and their pros and cons to be used in optical WBANs.

#### 3.2.2.1 Power-domain NOMA

In power-domain NOMA, signals from different users are transmitted by allocating different power levels. The channel gain difference between the received signals from multiple users is exploited at the Rx to recover the desired user signal. Figure 3.6 presents a conceptual diagram of a power-domain NOMA for the uplink, where transmitted signals from user 1 and user 2 are decoded by performing multi-user detection, e.g., SIC. Note that the strongest received signal (e.g., user 2 signal in Fig. 3.6) is decoded first, which is then subtracted from the received signal of user 1 before decoding its signal [176].

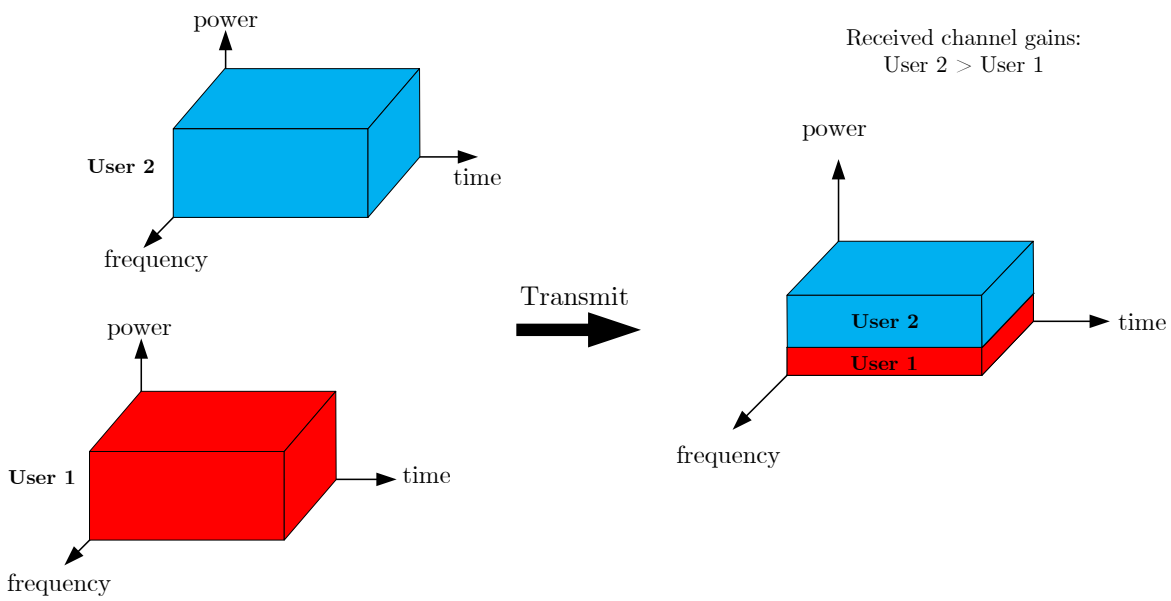


**Figure 3.6:** Resource allocation by a typical power-domain NOMA considering two users in the uplink. At the Rx, SIC is performed to distinguish desired user signal based on the difference in received channel gains.

In addition to the high computational complexity of SIC detection in the case of large number of users, the performance of power-domain NOMA is highly affected by the correlation between the users' channel gains [177]. This latter is usually the case in our $2^{nd}$ considered application scenario due to users' mobility and closely placed patients inside the emergency waiting room.

#### 3.2.2.2 Code-domain NOMA

In a code-domain NOMA, each user's data is spread over available time and frequency resources using SCs. Unlike conventional CDMA, this scheme allows overloading, i.e., the number of orthogonal resources can be less than the total number of users, in order to address massive connectivity. At the Rx, advanced multiuser detection (MUD) algorithms, e.g., message passing algorithm (MPA), expectation propagation algorithm (EPA), MMSE-SIC, and matched filter (MF)-SIC [178], can be employed in order to decode each user's signal. One major concern in code-domain NOMA is to optimize the trade-off between overloading factor and Rx complexity.

Several code-domain NOMA techniques have been proposed so far, the most popular include sparse-code MA (SCMA) [179], multi-user shared access (MUSA) [180], pattern division MA (PDMA) [181], and resource spread MA (RSMA) [182]. Table 3.1 presents the main features of these techniques, where RSMA appears to be the most interesting one for our application due to its low decoding complexity. However, scrambling codes with good correlation properties for optical communications are yet to be identified, which is an interesting direction for future research.

Note that, in the context of optical WBANs, a bandwidth-efficient SCMA technique was proposed in [183] for health information monitoring with relatively high decoding complexity, as compared to the TDMA and O-CDMA schemes. Bitstream mapping by SCMA technique is illus-

**Table 3.1:** Main features of different code-domain NOMA schemes, reproduced from [178].

| Attributes | SCMA | MUSA | PDMA | RSMA |
|---|---|---|---|---|
| Signature | Codebooks | Spreading Sequence | Codebooks | Scrambler |
| Sparse signature | Yes | No | Yes | No |
| MUD Rx | MPA (SIC)<br>EPA(SIC) | MMSE-SIC | MPA<br>MPA-SIC | MMSE-SIC<br>MF-SIC |
| Rx Complexity | High/<br>Moderate | Low | High/<br>Moderate | Low<br>Low |
| Device overload | Moderate | High | Moderate | High |

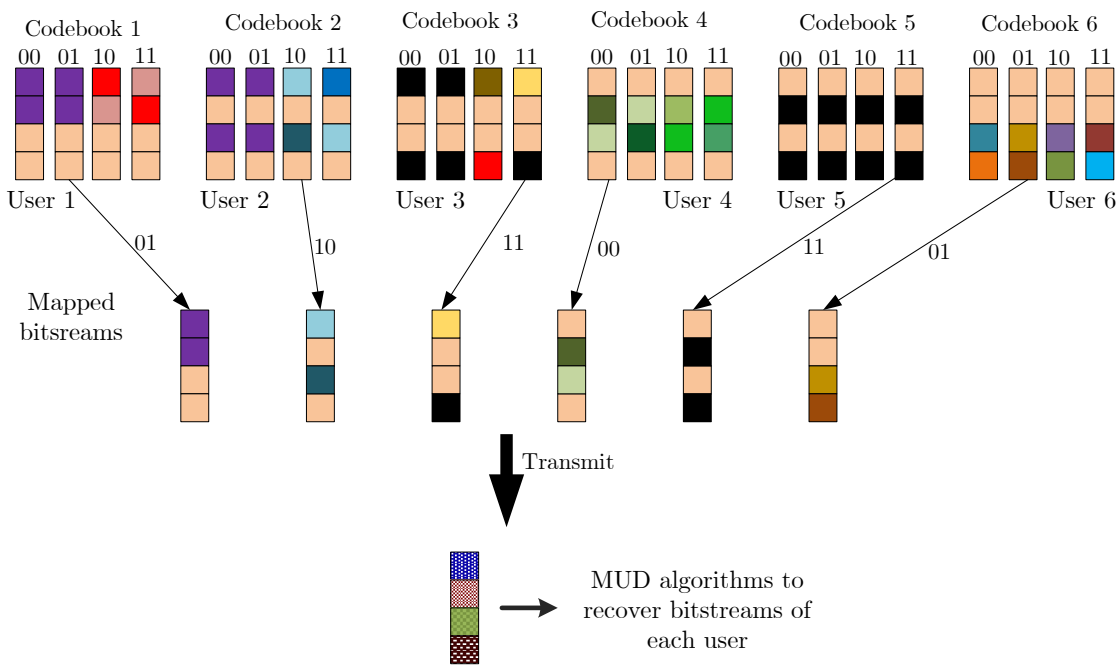


**Figure 3.7:** Bitstream mapping by SCMA considering six users for the uplink. Each user's bitstreams are mapped to four orthogonal sparse codes from the assigned codebook.

trated in Fig. 3.7, where six users data are transmitted using four sparse code, i.e., with an overloading factor of 150%.

## 3.3 MA Candidates for Optical WBANs

In this section, we describe in more detail suitable MA candidates, i.e., O-OCDMA, O-OFDMA, and O-SCFDMA, for uplink extra-WBAN transmission.

### 3.3.1 O-CDMA

The structure of O-CDMA signaling depends on the type of SCs, i.e., bipolar or unipolar codes, used to map the data of different users [184].

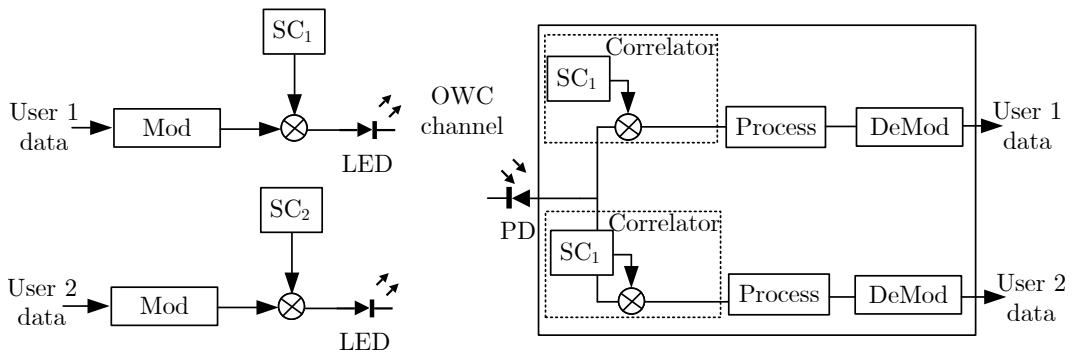


**Figure 3.8:** Typical block diagram of O-CDMA for two users in the uplink. Blocks Mod and DeMod stand for modulator and demodulator, respectively.

#### 3.3.1.1 O-CDMA Based on Unipolar Codes

Figure 3.8 presents the typical structure of O-CDMA signaling based on unipolar codes. At the Tx, each user is at first assigned a SC, then each bit from the user data stream is multiplied by this SC and transmitted through the optical channel. At the Rx, to recover the data of a specific user, the received signals are at first correlated with the corresponding assigned SC. The output of each correlator is then processed based on the modulation technique employed. The resulting signal is then demodulated to extract the transmitted bits of each user.

O-CDMA can be implemented using unipolar codes, e.g., optical orthogonal code (OOC) [185], prime code (PC) [186], or random optical code (ROC) [187]. O-CDMA based on PCs has the advantages of a relatively simple implementation and straightforward code generation techniques. However, it is not suitable for asynchronous data transmission. A variety of ROCs has been proposed for O-CDMA in [187, 188], but they do not have ideal correlation properties. The OOCs are the most mature binary SCs, first employed for optical fiber communications. Due to their good correlation properties, OOCs have been widely adopted in O-CDMA systems, as compared to the PCs and ROCs [184]. The use of OOC-based O-CDMA for WBANs was first considered in [105]. In order to increase the robustness against MAI, we also consider in this thesis O-CDMA based on OOC that will be described in detail in Chapter 4, where we will also analyze its performance considering a realistic medical WBAN scenario.

#### 3.3.1.2 O-CDMA Based on Bipolar Codes

Bipolar codes, which are commonly employed in RF CDMA systems, can also be adapted for use in O-CDMA. The Walsh-Hadamard (WH) sequences are the most popular bipolar codes used in most O-CDMA systems. For instance, in [189], O-CDMA was used for VL downlink transmission, where WH codes are employed along with pseudo-noise (PN) sequences to mitigate inter- and intra-cell interference. Figure 3.9 presents an O-CDMA signaling scheme based on bipolar sequences, in which modulated data from each user are multiplied by the assigned WH and PN sequences before

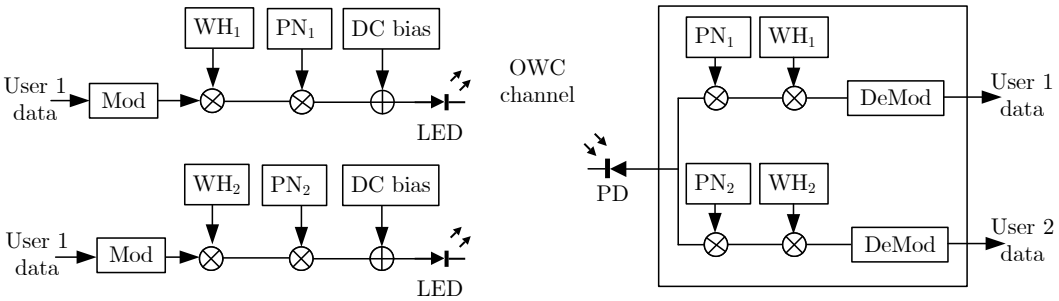


**Figure 3.9:** Typical block diagram of O-CDMA signaling based on WH and PN sequences for two users.

being transmitted by the LED. At the Rx side, the received signals at the PD are multiplied by the desired user's PN and WH sequences to recover its transmitted data. However, when used in asynchronous systems, the ideal autocorrelation and cross-correlation properties of WH sequences are lost. To address this, Gold sequences [190] or m-sequences [191] can be used for asynchronous O-CDMA systems. However, their drawback is that, unlike unipolar OOC codes, they lack good correlation properties. Moreover, bipolar O-CDMA systems require DC biasing prior to drive the LED (see Fig. 3.9), resulting in higher power consumption at the Tx.

### 3.3.2 O-OFDMA

#### 3.3.2.1 DCO-OFDMA

Figure 3.10 shows the block diagram of DCO-OFDMA signaling. First, the collected data bits from sensors are grouped together by the serial to parallel (S/P) converter and mapped into $M$-QAM complex symbols $\check{X}_{\acute{k}}$, $\acute{k} = 0, 1 \ldots, \mathscr{M} - 1$. Here, $\mathscr{M}$ refers to the number of data-carrying symbols (i.e., subcarriers) per user[1]. Then, these $\mathscr{M}$ symbols are mapped into a subset of subcarriers $X_k$, $k = 0, 1 \ldots, N - 1$, where $N$ is the total number of subcarriers before the HS block. Considering a maximum $\mathscr{L}$ number of patients, the total number of subcarriers is $N = \mathscr{M}\mathscr{L}$. We will later explain in detail the subcarrier mapping techniques. To obtain a real TD OFDMA signal, HS constraint is then imposed on $X_k$ to get $\tilde{X}_{\hat{k}}$, $\hat{k} = 0, 1 \ldots, \mathscr{N} - 1$; $\mathscr{N} = 2N + 2$, such that,

$$\tilde{X}_{\hat{k}} = \left[0, X_0, X_1, \ldots, X_{N-1}, 0, X^*_{N-1} \ldots, X^*_0\right].$$

Then, an $\mathscr{N}$-point inverse-fast-Fourier transform (IFFT) is performed, that generates the real-valued TD signal $x_n$:

$$x_n = \frac{1}{\sqrt{\mathscr{N}}} \sum_{\hat{k}=0}^{\mathscr{N}-1} \tilde{X}_{\hat{k}} \exp\left(j \frac{2\pi n \hat{k}}{\mathscr{N}}\right); \; n = 0, 1, \ldots, \mathscr{N} - 1. \tag{3.1}$$

After parallel to serial (P/S) and adding a CP of length $\mathscr{N}_{\text{CP}}$ at the end of each frame, the resulting signal is passed through a DAC and an amplifier (AMP) before the addition of a DC bias $\mathscr{B}_{\text{DC}}$ to

[1] In the sequel, we use the two terms subcarriers and symbols interchangeably.

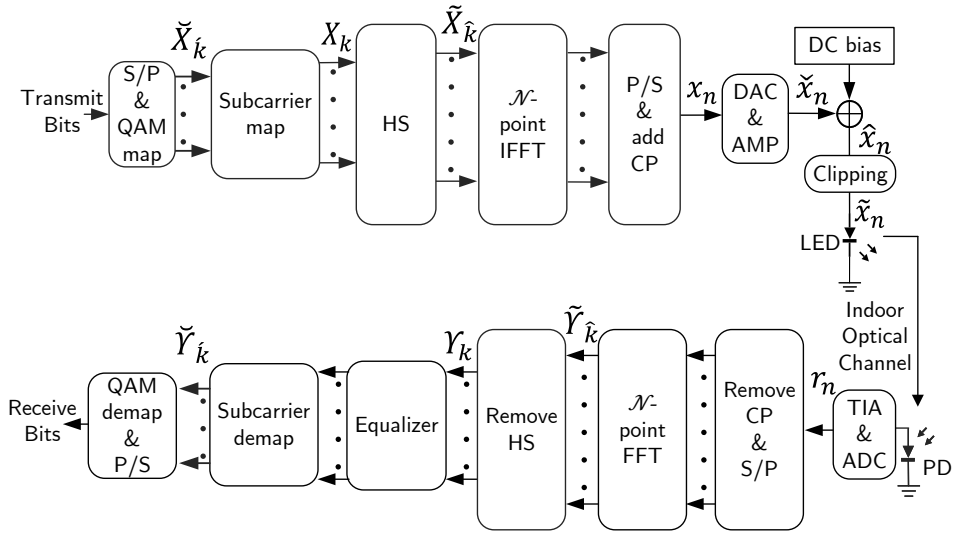


**Figure 3.10:** Block diagram of the DCO-OFDMA signaling scheme.

obtain $\hat{x}_n$:

$$\hat{x}_n = \check{x}_n + \mathscr{B}_{\mathrm{DC}}, \tag{3.2}$$

where $\check{x}_n$ denotes the amplified signal (see Fig. 3.10). Note that, to fix the DC bias, the dynamic range (DR) of the LED should be taken into account, as explained later in Section 5.3.3. Lastly, after lower and upper clipping $\hat{x}_n$, the resulting signal $\tilde{x}_n$ will drive the LED.

At the Rx, after photo-detection and removing the DC, the obtained electrical signal is amplified by a TIA and passed to an ADC to generate a discrete-time signal $r_n$. Then, after removing the CP and S/P conversion, $\mathcal{N}$-point fast-Fourier transform (FFT) is done on the signal, resulting in:

$$\tilde{\Upsilon}_{\hat{k}} = \frac{1}{\sqrt{\mathcal{N}}} \sum_{n=0}^{\mathcal{N}-1} r_n \exp\Big(-j\frac{2\pi n\hat{k}}{\mathcal{N}}\Big)\,;\ \hat{k} = 0,1,\ldots,\mathcal{N}-1. \tag{3.3}$$

Afterwards, after removing HS from $\tilde{\Upsilon}_{\hat{k}}$, a single-tap equalization is performed on the resulting signal $\Upsilon_k$. Then, the signal is passed through a subcarrier demapping block to obtain symbols $\check{\Upsilon}_{\acute{k}}$ corresponding to the desired user data before P/S conversion and QAM demodulation.

**A. Subcarrier Mapping:** Subcarrier mapping techniques are typically classified into localized subcarrier mapping and distributed subcarrier mapping, where the former allocates the subcarriers consecutively and the latter distributes subcarriers throughout the entire bandwidth while the zeros occupying the unused subcarriers. In fact, the distributed subcarrier mapping with equidistant subcarriers is referred to as interleaved subcarrier mapping. The interleaved and localized subcarrier mappings are presented in Fig. 3.11 for the case of three users. Not that the interleaved subcarrier mapping leads to a better PAPR performance for the case of SCFDMA [192], and allows mitigating burst errors.

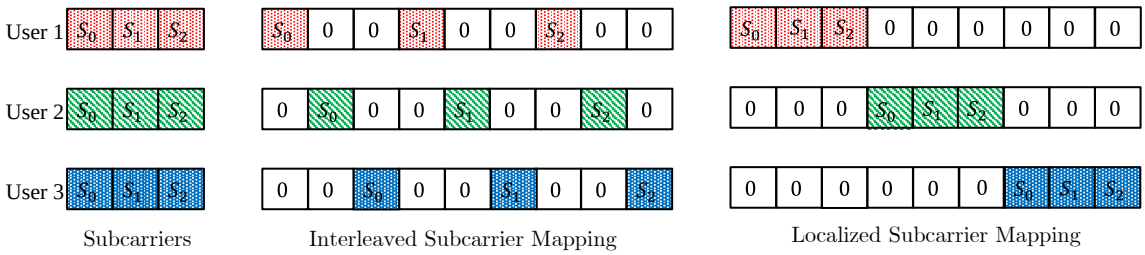


**Figure 3.11:** An example of interleaved subcarrier mapping and localized subcarrier mapping for the case of three users, each having three symbols denoted by $S_0$, $S_1$, and $S_2$.

#### 3.3.2.2 ACO-OFDMA

In ACO-OFDMA, only odd subcarriers are used for signal transmission. After applying the HS constraint, the input symbol frame $\tilde{X}_{\hat{k}}$ before the IFFT has the following structure,

$$\tilde{X}_{\hat{k}} = \left[0, X_0, 0, X_1, \ldots, 0, X_{N-1}, 0, X^*_{N-1}, \ldots, 0, X^*_0\right].$$

After the IFFT, the negative samples can be clipped without loss of information due to the anti-symmetry property of $x_n$ [193]. The subsequent steps for ACO-OFDMA are similar to those of DCO-OFDMA, described in the previous subsection. Note that ACO-OFDMA also requires a DC bias to be added to $\check{x}_n$ to adapt to the actual LED I-V characteristics [120], as will be explained later in Chapter 4.

### 3.3.3 O-SCFDMA

#### 3.3.3.1 DCO-SCFDMA

The block diagram of the DCO-SCFDMA scheme is shown in Fig. 3.12. The QAM mapped symbols from each user are precoded by an additional $\mathscr{M}$-point FFT before subcarrier mapping and applying HS, and $\mathscr{N}$-point IFFT. This allows to reduce the signal PAPR at the cost of increased complexity. The other steps of signal transmission are similar to the case of DCO-OFMDA, explained above.

At the Rx side, after $\mathscr{N}$-point FFT, equalization and subcarrier demapping, an $\mathscr{M}$-point IFFT is applied to the resulting signal to remove the precoding done at the Tx, see Fig. 3.12.

#### 3.3.3.2 ACO-SCFDMA

Similar to the case of O-OFDMA, described in Subsection 3.3.2.1 and 3.3.2.2, by ACO-SCFMDA, the transmit signal frame follows the same steps as for DCO-SCFDMA except that only the odd subcarriers are used for data transmission.

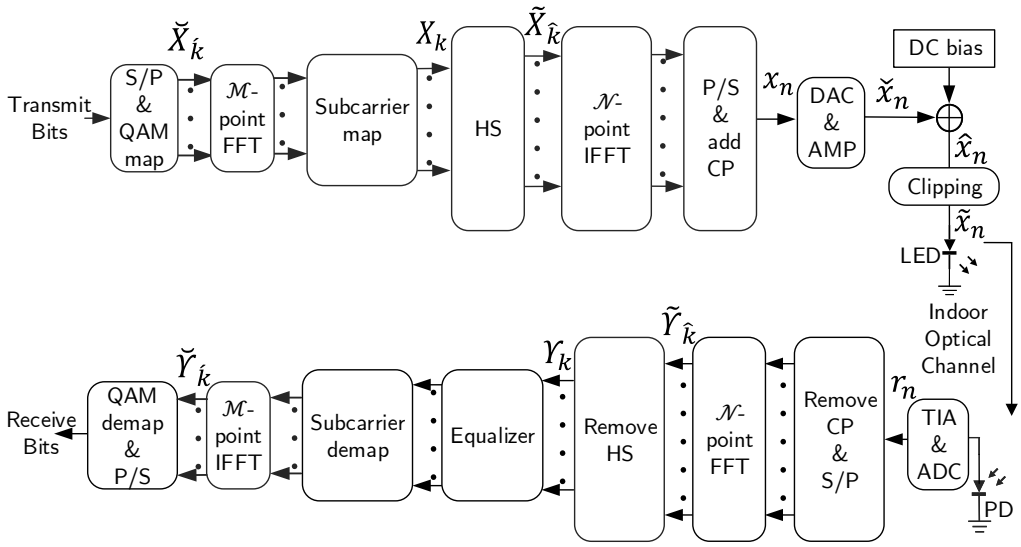


**Figure 3.12:** Block diagram of the DCO-SCFDMA signaling scheme.

## 3.4 Chapter Summary

In this chapter, we provided a literature survey of conventional and state-of-the-art MA solutions and investigated their suitability for use in optical WBANs. Taking into account two use cases, i.e., a small number of patients in a hospital ward scenario and a relatively large number of patients in an emergency waiting room scenario, we proposed two different MA solutions. Moreover, we presented the detailed structures of O-CDMA schemes based on bipolar and unipolar codes. Meanwhile, we showed that bipolar codes are not suitable for asynchronous data transfer and further a DC bias needs to be added to the transmitted signal (prior to LED intensity modulation). Considering the good correlation properties in asynchronous mode and the requirement of managing MAI efficiently, we have concluded that the most appropriate approach here is to use O-CDMA based on unipolar SCs. Finally, we provided the descriptions of O-FDMA and O-SCFDMA schemes for the cases of ACO and DCO signaling, and explained their subcarrier mapping techniques. The retained MA techniques based on the application scenarios are summarized as follows:

- MA solutions:
  - O-CDMA for a hospital ward scenario (small number of patients)
  - O-OFDMA for an emergency waiting room scenario (relatively large number of patients)
- SC for O-CDMA:
  - Optical orthogonal code (OOC)
- Subcarrier mapping technique for O-OFDMA based schemes:
  - Interleaved subcarrier mapping

In the next chapter, we analyze the performance of O-CDMA based on OOC codes for uplink transmission considering the hospital ward scenario. We will take into account random Tx orientations by employing the ORWP mobility model as described in Chapter 2. Afterwards, considering the computational complexity of the O-OFDMA scheme, a new energy-efficient technique will be proposed in Chapter 5, based on the transmission of the real-part of the OFDMA signal.

# Chapter 4

# Performance of O-CDMA for Medical WBANs

**Contents**


**4.1 Introduction** . . . . . **57**
**4.2 Assumptions and Considered Hospital Ward Scenario** . . . . . **58**
**4.3 BPPM O-CDMA Signaling** . . . . . **59**
**4.4 Performance Evaluation of BPPM O-CDMA Signaling** . . . . . **61**
4.4.1 BER Analysis . . . . . 61
**4.5 Performance Analysis** . . . . . **64**
4.5.1 Effect of Tx Orientation on the Received Power . . . . . 65
4.5.2 MAI Effect on Link Performance . . . . . 66
4.5.2.1 Fixed Tx Orientation . . . . . 66
4.5.2.2 Random Tx Orientation . . . . . 68
4.5.2.3 Accounting for Non-LOS Contribution . . . . . 68
4.5.2.4 Accounting for Random User Movements . . . . . 69
4.5.3 Interest of Using Multiple APs . . . . . 70
**4.6 Chapter Summary and Discussions** . . . . . **73**


## 4.1 Introduction

In this chapter, we study the performance of O-CDMA when used for extra-WBAN links. In contrast to the work presented in [105], we take into account the Tx power constraint due to eye-safety considerations, the different noise sources at the Rx, as well as randomly changing Tx orientations. Based on the RWP model, we further consider the user mobility in our study by using the generalized model of ORWP model presented in Chapter 2, in order to include the effect of random Tx orientations. Moreover, we investigate the improvement of the link quality through the use of multiple APs in the room. Performance evaluation is mainly done in terms of the link outage probability $P_{\text{out}}$, which is studied for the first time within this context, to the best of our knowledge.

In Section 4.2, we present the hospital ward scenario and the underlying assumptions, e.g., room dimensions, number of patients. In Section 4.3, we describe the BPPM O-CDMA signaling based on OOC codes as signature sequences. In Section 4.4, we provide the mathematical formulations for studying the link performance. Numerical results are then presented in Section 4.5 to investigate the BER and $P_{\text{out}}$ performances of the system for changing users' locations in the room and different AP arrangements. At first, we study the effect of Tx orientations on the LOS link outage, i.e., LOS blockage. We show that the random orientation of the CN has a detrimental impact on the link performance when the distance between the CN and the AP increases. Then, we analyze the MAI effect on the O-CDMA link performance by changing users' positions while accounting for LOS and LOS+1$^{\text{st}}$ order reflections. Meanwhile, we evaluate the impact of random Tx orientations and user movements based on realistic ORWP mobility model on the MAI performance. We conclude that the performance degrades mostly due to the LOS link blockage and the received weak signals from the reflections. Finally, we demonstrate the performance improvements through the use of multiple AP arrangements. The main conclusions and some discussions of this chapter are provided in Section 4.6.

## 4.2 Assumptions and Considered Hospital Ward Scenario

Figure 4.1 illustrates a typical hospital ward with potentially up to four patients inside, where IR links are used for extra-WBAN uplink transmission. Note that, most hospital guidelines recommend a maximum of four patients in a ward [106].

As mentioned in Chapter 2, we consider the use of IR LEDs because of their relatively low cost and more tolerable eye-safety features (due to the typically much wider beams), compared to LDs. In practice, each CN could be equipped with an IR LED, like [194], with a wavelength of 940 nm, a transmitting area of 1 mm$^2$ and a radiant intensity of 300 mW/sr corresponding to a typical transmit power of 1150 mW. Then, according to [63], up to 10 LEDs can be used simultaneously in this configuration and with a 50% duty cycle while still meeting the IEC "no risk group" requirements.

We consider a hospital ward with room dimensions $8 \times 8 \times 3\,\text{m}^3$, which satisfies the general health-care guidelines [106]. Unless otherwise specified, only one single AP, placed at the center of the room ceiling, is assumed in the sequel. The AP is connected through a wire backbone to a local network switch as shown in Fig. 4.1. Patients are considered to be equipped with different medical sensors to monitor their temperature, blood-saturation, blood pressure, etc. (not shown in the figure). The CN collects the data from all sensors before sending them to the AP(s). As mentioned in Chapter 1, IR OWC links can be used for intra-WBAN data transmission, where a different wavelength can be used in order to avoid any interference between intra- and extra-WBAN links (using optical filters at the Rxs). Therefore, reasonably, we do not consider any potential MAI corresponding to intra-WBAN connections in this thesis. The requirement in terms of data-rate for most sensors is less than 100 Kbps, as presented in Table 1.2. Consequently, here we consider a data-rate of up to 100 Kbps for the extra-WBAN link.

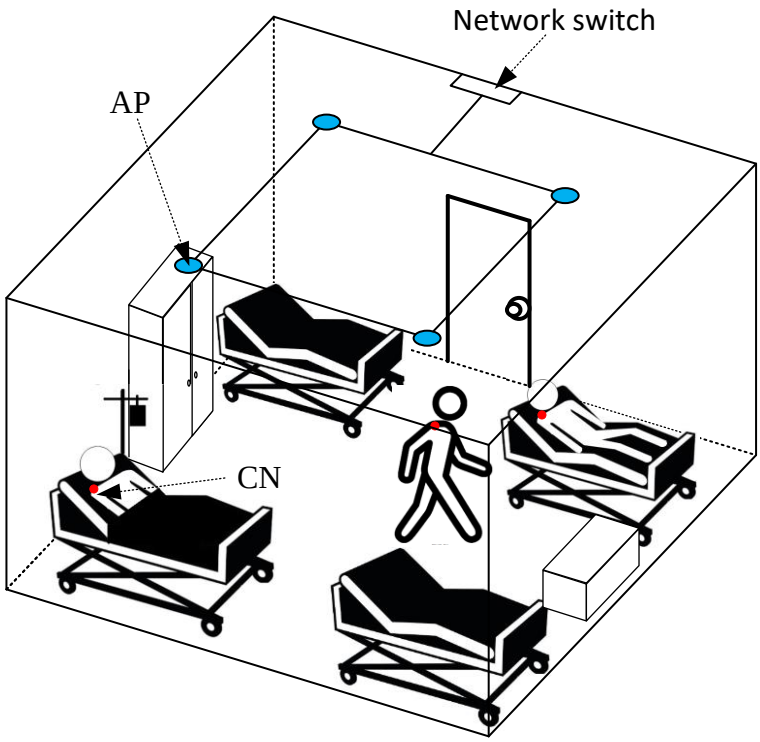


**Figure 4.1:** Illustration of a typical hospital ward scenario using an IR based extra-WBAN with multiple patients, each one having a CN (the red bullet on the shoulder). Here, 4 APs are considered, placed on the ceiling.

As mentioned in Chapter 2, considering hybrid link configuration, we assume a relatively large FOV at the AP (with no concentrator) and the use of a simple PIN PD. Given the relatively low data-rate transmission, the OOK modulation would be a suitable choice due to its simplicity. Here, instead, we consider the BPPM modulation, which has almost the same performance as OOK but with the advantage that no adaptive thresholding is needed for optimal signal detection at the Rx [116,195]. Note that, although non-binary PPM would be more advantageous in terms of energy efficiency [196], we suggest using BPPM which has the advantages of a lower required bandwidth, less constraints in terms of eye-safety, and lower implementation complexity.

## 4.3 BPPM O-CDMA Signaling

An illustrative example of a BPPM O-CDMA transmitted signal is shown in Fig. 4.2. Each user is assigned a SC, also called spread sequence, which is multiplied by the corresponding signal. At the Rx (i.e., the AP), signals of all users are received on the PD, see Fig. 4.3. In order to extract and detect the data of a specific user, each BPPM slot of the received signal is correlated with the corresponding SC (block "Correlator") over the slot duration. Afterwards, the demodulator extracts the transmitted bits by comparing the correlator outputs corresponding to the BPPM slots.

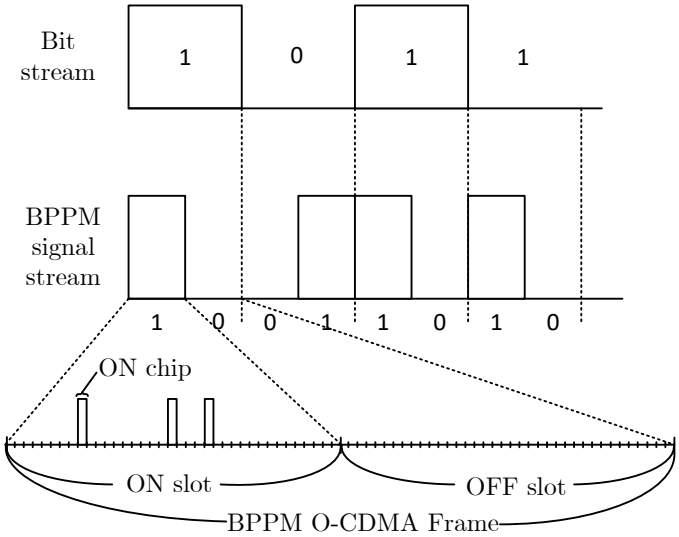


**Figure 4.2:** Example of frame structure of BPPM O-CDMA signaling.

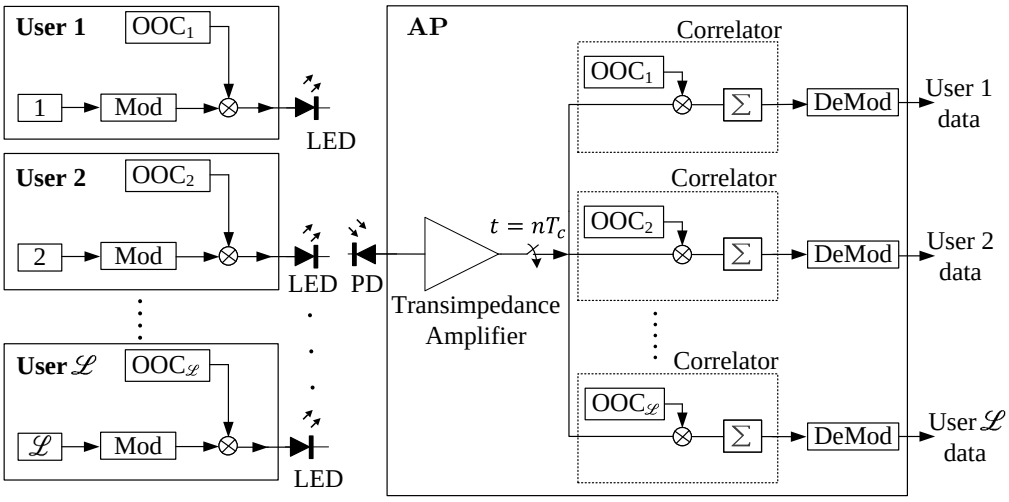


**Figure 4.3:** Block diagram of the proposed O-CDMA based extra-WBAN system; Blocks Mod and DeMod stand for modulator and demodulator. Signal sampling at the trans-impedance amplifier output is done at sampling period of $T_c$, the chip duration.

As explained in Chapter 3, an OOC is usually used as SC. This binary sequence, is denoted by OOC $(F, K, \lambda_a, \lambda_c)$, where $F$ is the SC length (i.e., the number of chips), $K$ is its weight (i.e., the number of ones in the sequence), and $\lambda_a$ and $\lambda_c$ stand for the auto-correlation and cross-correlation constraints, respectively [197]. For given OOCs $u$ and $v$, the following conditions hold

[185]:

$$\Gamma_{u,u}(\kappa) = \sum_{n=0}^{F-1} u_n u_{n+\kappa} \begin{cases} = K & ; \kappa = 0 \\ \leq \lambda_a & ; 1 \leq \kappa \leq F-1 \end{cases} \tag{4.1}$$

$$\Gamma_{u,v}(\kappa) = \sum_{n=0}^{F-1} u_n v_{n+\kappa} \leq \lambda_c \ ; \ 0 \leq \kappa \leq F-1. \tag{4.2}$$

Here, $\Gamma_{u,u}$ and $\Gamma_{u,v}$ denote the auto-correlation of $u$, and the cross-correlation of $u$ and $v$, respectively. As a matter of fact, since IM/DD signal transmission is used, here we cannot have strict orthogonality between two SCs. For OOCs, we have $\lambda_a$=$\lambda_c$= 1 which results in minimum MAI. For OOC ($F$, $K$, 1, 1) codes, the maximum number of users $\mathscr{L}$ that can be handled is upper bounded by [185]:

$$\mathscr{L} \leq \frac{F-1}{K(K-1)}. \tag{4.3}$$

For such codes, error-free data recovery for an "ideal" link (i.e., without noise effect and only from a MAI point of view) is possible provided that $K$ satisfies the following condition [185, 197]:

$$K > \mathscr{L} - 1. \tag{4.4}$$

Note that, the effect of MAI can be reduced when using $\ddot{M}$-ary PPM, $\ddot{M} > 2$ [198]. This, however, results in relatively poor bandwidth efficiency and increases the complexity of signal transmission at both Tx and Rx and the required speed of electronics, as mentioned in Chapter 2. Therefore, we consider the BPPM modulation in this work, as mentioned previously. Note that, here, each BPPM slot duration equals $F\,T_c$.

## 4.4 Performance Evaluation of BPPM O-CDMA Signaling

As mentioned previously, from a system design point of view, we consider asynchronous transmission from different users, which results in reduced implementation complexity. That is, each CN sends its data asynchronously to the AP. We are hence concerned by the near-far problem, which has been the subject of extensive research for CDMA-based RF systems [199, 200], e.g., in the context of the 3rd generation of cellular mobile networks. Here, in order to simplify the system performance analysis, we make the assumption of chip synchronous transmission. This corresponds the worst case, regarding MAI, and provides an upper bound on the system performance [201].

### 4.4.1 BER Analysis

As shown in Fig. 4.2, BPPM symbols are composed of two ON and OFF slots. Here, without loss of generality, we assume that '0' and '1' information bits are mapped to (OFF, ON) and (ON, OFF) BPPM symbols, respectively. With BPPM O-CDMA, each slot of a given user is multiplied by its SC code, as illustrated in Fig. 4.2. For the synchronous transmission case, the ON chips of two OOCs (satisfying $\lambda_a$=$\lambda_c$= 1) cannot overlap on more than one chip position. For two different users, there are $K^2$ possible ways of overlapping between $K$ ON chips of the two corresponding OOCs.

Then, given the OOC length $F$, the probability that an interfering user's ON chips of a BPPM slot overlap with those of a desired user is given by [164, 185]:[1]

$$q = \frac{K^2}{2F}, \tag{4.5}$$

where the factor 1/2 is the probability that the interfering user sends a one in the first BPPM slot and a zero in the second BPPM slot. For a total number of $\mathscr{L}$ users, the probability $P_i(\ell)$ that $\ell$ users interfere with a desired user's signal follows a binomial distribution that can be expressed as [185, 201]:

$$P_i(\ell) = \binom{\mathscr{L}-1}{\ell} q^{\ell} (1-q)^{\mathscr{L}-1-\ell} \quad ; \quad 0 \le \ell \le \mathscr{L}-1. \tag{4.6}$$

The overall probability of interference occurrence $P_i$ is then:

$$P_i = \begin{cases} P_i(\ell) & ; \ \ell = 0 \\ \sum_{\ell=1}^{\mathscr{L}-1} P_i(\ell) & ; 1 \le \ell \le \mathscr{L}-1. \end{cases} \tag{4.7}$$

The first step of the decoding process is to correlate the received signal with the corresponding OOC code over the BPPM slot duration. Let us denote by $\chi_1$ and $\chi_2$ the correlator outputs corresponding to the first and the second BPPM slots, respectively. For demodulation, these outputs are compared to make a decision on the transmitted bit (the DeMod block in Fig. 4.3). A detection error occurs if $\chi_2 > \chi_1$, when the transmitted data bit is '1', or if $\chi_1 > \chi_2$, otherwise. Assuming equally likely transmitted bits, the bit error probability $P_E$, or in other words the BER, is given by [202]:

$$\begin{aligned} P_E &= \tfrac{1}{2} P_i \Big[ P_E(\text{error}|'0') + P_E(\text{error}|'1') \Big] \\ &= \tfrac{1}{2} P_i \Big[ \text{Prob}(\chi_1 \ge \chi_2|'0') + \text{Prob}(\chi_2 \ge \chi_1|'1') \Big], \end{aligned} \tag{4.8}$$

where 1/2 is the probability of the transmitted bit '1' or '0' and, for instance, $P_E(\text{error}|'0')$ denotes the error probability conditioned to the transmission of a bit '0'. Logically, we have $P_E(\text{error}|'0') = P_E(\text{error}|'1')$.

To analyze the worst MAI case, in addition to the assumption of synchronous chip transmission, we consider the case where the desired user transmits a bit '0', represented by the (OFF, ON) BPPM symbol, and all the $\mathscr{L}-1$ interferers transmit bit '1', i.e., the (ON, OFF) BPPM symbol. This allows to evaluate the upper bound on the conditional probability. Concerning the Rx noise, the corresponding generated photoelectrons at the PD output over an O-CDMA chip time $T_c$ has a Poisson distribution [203]. Concerning the correlator output at each BPPM slot, the resulting Poisson distribution with a relatively large mean can be well approximated by a Gaussian distribution. Let us denote by $I_1$ and $I_2$, and $\sigma_1^2$ and $\sigma_2^2$, the means and variances of the correlator outputs cor-

[1] Note that the probability of interference between two OOCs with either OOK or BPPM modulations is the same [164].

responding to the first and second BPPM slots, respectively. We have:

$$\begin{aligned} I_1 &= KI_d + KI_a + \sum_{j=1}^{\mathscr{L}-1} I_{Ij}, \\ I_2 &= KI_d + KI_a + KI_r, \\ \sigma_1^2 &= K\sigma_{I_d}^2 + K\sigma_{I_a}^2 + \sum_{j=1}^{\mathscr{L}-1} \sigma_{I_{Ij}}^2 + K\sigma_T^2, \\ \sigma_2^2 &= K\sigma_{I_d}^2 + K\sigma_{I_a}^2 + K\sigma_{I_r}^2 + K\sigma_T^2. \end{aligned} \tag{4.9}$$

Here, $I_d$ and $I_a$ denote the dark current noise and the ambient current noise, $I_r$ is the photo-current corresponding to the desired user's chip, and $I_{Ij}$ is the photo-current corresponding to the $j^{\text{th}}$ interfering user's ON chips. The factor $K$ in $I_1$ and $I_2$ is due to the correlation with the OOC, which has weight $K$. We have:

$$I_r = \frac{q_e \eta P_{r,d}}{h\nu}, \quad I_{Ij} = \frac{q_e \eta P_{r,j}}{h\nu}, \tag{4.10}$$

where $\nu$ is the light frequency, $\eta$ is the PD quantum efficiency, and $h$ is the Plank's constant. Also, $P_{r,d}$ is the received power from the desired user and $P_{r,j}$ is the received power from the $j^{\text{th}}$ interferer. The corresponding variances are [204]:

$$\begin{cases} \sigma_{I_d}^2 = 2\, q_e\, I_d\, B, \\ \sigma_{I_a}^2 = 2\, q_e\, I_a\, B, \\ \sigma_{I_r}^2 = 2\, q_e\, I_r\, B, \\ \sigma_{I_{Ij}}^2 = 2\, q_e\, I_{Ij}\, B. \end{cases} \tag{4.11}$$

Remember that, $B$ denotes the transmission bandwidth (i.e., minimum required bandwidth of Rx low-pass filter) and $q_e$ is the electron charge. Also, $\sigma_T^2$ in (4.9) stands for the Rx thermal noise variance, defined as [204]:

$$\sigma_T^2 = \frac{4\, K_B\, T_r\, B}{R_L}, \tag{4.12}$$

where $T_r$ is the equivalent noise temperature, $K_B$ denotes Boltzman's constant and $R_L$ is the load resistance of the Rx TIA.

Note that, given that the correlation with the OOC consist of the summation of signals corresponding to non-zero weights, the noise at the correlator output can be assumed to follow a Gaussian distribution. Consequently, we can write [202]:

$$\begin{aligned} \text{Prob}(\chi_1 \geq \chi_2 | '0') = &\int_{-\infty}^{\infty} \frac{1}{\sqrt{2\pi\sigma_1^2}} \exp^{-(x-I_1)^2/2\sigma_1^2} \\ &\times \int_{-\infty}^{x} \frac{1}{\sqrt{2\pi\sigma_2^2}} \exp^{-(y-I_2)^2/2\sigma_2^2}\, dy\, dx, \end{aligned} \tag{4.13}$$

The BER for the case of the absence of MAI can be calculated by setting $\ell = 0$ in (4.6) and $P_{r,j} = 0$ in (4.10).

**Table 4.1:** Parameters used for numerical simulations.

| Parameter | Symbol | Value |
|---|---|---|
| Max. number of users | $\mathscr{L}$ | 4 |
| Transmission bandwidth | $B$ | 10 MHz |
| Target BER | $\mathrm{BER_{th}}$ | $10^{-3}$ |
| Room dimension | — | $8 \times 8 \times 3\,\mathrm{m}^3$ |
| CN height | $h_{\mathrm{CN}}$ | 1.4 m |
| Tx orientation angle | $\theta_{tx}$ | -90° – 90° |
| Walls reflection coefficient [205] | $\rho$ | 0.8 |
| No. of reflecting surface elements | — | 100 /m$^2$ |
| Patient minimum speed | $V_{\mathrm{min}}$ | 0.2 m/s |
| Patient maximum speed | $V_{\mathrm{max}}$ | 0.6 m/s |
| Pause time | $\mathscr{T}_p$ | 1 sec |
| LED wavelength | $\lambda$ | 880 nm |
| LED semiangle at half power [52] | $\phi_{1/2}$ | 60° |
| OOC code | — | (49,4,1,1) |
| OOC length | $F$ | 49 |
| OOC weight | $K$ | 4 |
| PD quantum efficiency [206] | $\eta$ | 0.66 |
| PD active area | $A_{\mathrm{PD}}$ | 1 cm$^2$ |
| TIA load resistance | $R_L$ | 10 kΩ |
| Rx dark current [207] | $I_d$ | 10 nA |
| Rx noise temperature | $T_r$ | 300 K |
| Rx FOV | $\psi_c$ | 75° |
| Ambient current noise [208] | $I_a$ | 490 µA |

## 4.5 Performance Analysis

We present here a set of numerical results to study the performance of an extra-WBAN link using BPPM O-CDMA signaling. Simulation parameters are summarized in Table 4.1. In particular, to reduce the probability of LOS blockage, we consider a relatively wide beam at the Tx, i.e., $\phi_{1/2}$ = 60° corresponding to $m = 1$, and a relatively large Rx FOV, i.e., $\psi_c$ = 75°. Also, by default and unless otherwise mentioned, one single AP is considered, placed at the center of the ceiling. As mentioned before, the body has a rather little impact on the link performance for relatively low data-rate applications, provided that the $P_{\mathrm{out}}$ requirement is limited to about $10^{-2}$ [66]. Therefore, to simplify channel modeling and to reduce the simulation time, the impact of the patient's body is not taken into account in our study, assuming that a $P_{\mathrm{out}}$ of $10^{-2}$ would be adequate to achieve the required QoS for the considered WBAN applications.

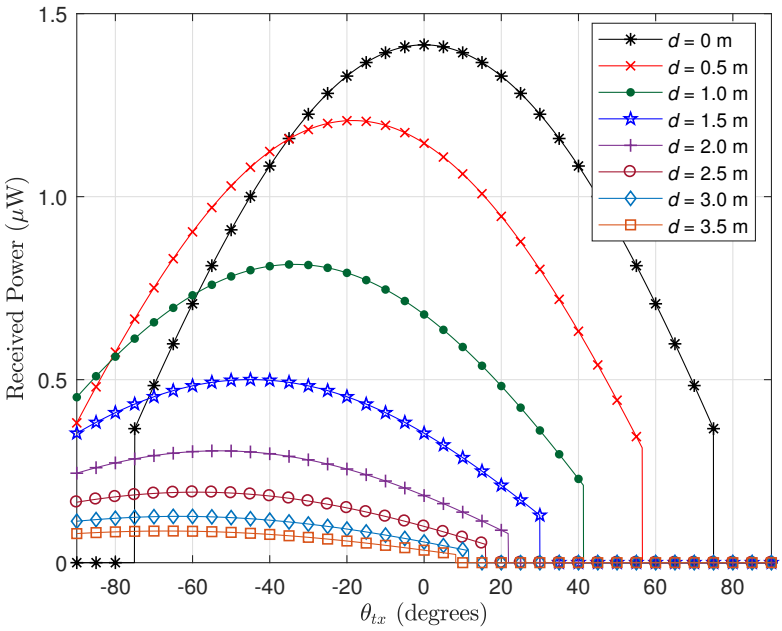


**Figure 4.4:** Impact of Tx orientation on the LOS outage for distances $d$ from the room center, $P_{t(\text{opt})}$= 100 mW. Only the LOS path is taken into consideration.

### 4.5.1 Effect of Tx Orientation on the Received Power

Let us first consider a single Tx in the room, i.e., the case of no MAI, and see the effect of random orientations of the Tx. As a link outage can most possibly occur due to LOS blockage, we study the effect of Tx random orientations on the received power by neglecting the diffuse link. Figure 4.4 shows the received optical power at the AP versus $-90° \leq \theta_{tx} \leq 90°$ for different Tx distances $d$ from the room center assuming a 100 mW transmit power. As seen from the figure, for too large $\theta_{tx}$, the LOS between the Tx and the AP is lost, resulting in zero received power (remember that we neglect the diffuse link). For $d = 0$, the received power falls to zero for $|\theta_{tx}|$ larger than the Rx FOV. Logically, random orientation of the CN can have a more detrimental impact on the link performance as the Tx moves from the center of the room to the corner. For instance, for $d = 3.5$ m, the LOS is lost for $\theta_{tx} > 8°$ only.

Let us now consider the effect of Tx random orientation $-90° \leq \theta_{tx} \leq 90°$ on the detected received optical power at the AP. We have presented in Fig. 4.5 the minimum and maximum detectable received power versus $d$, considering the cases of LOS and LOS+1$^{\text{st}}$-order reflections and for different transmit power levels $P_{t(\text{opt})}$. As expected, the minimum and maximum received powers decrease with increasing $d$ when taking only the LOS into account. However, when taking the 1$^{\text{st}}$-order reflections into account, the maximum received power increases slightly as the distance $d$ increases due to the decreasing path length of the first-order reflections from the walls.

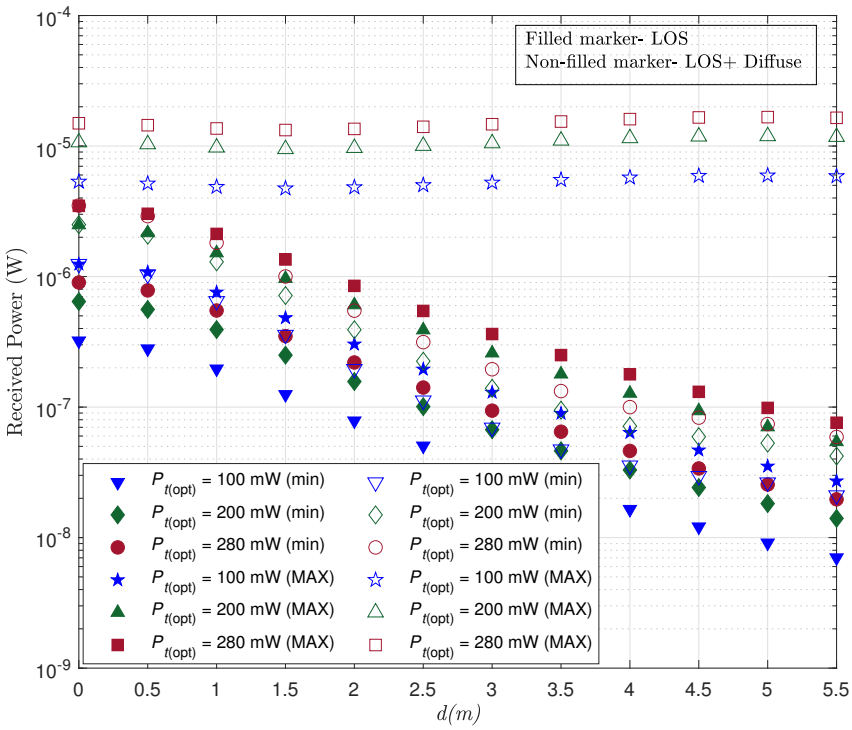


**Figure 4.5:** Impact of Tx orientation on the minimum (min) and maximum (MAX) detectable received power for distances $d$ from the room center. LOS and LOS+1$^{st}$-order reflections are taken into consideration.

### 4.5.2 MAI Effect on Link Performance

To focus on the MAI effect, we again consider only the LOS link by neglecting the diffuse link. We start by considering some special scenarios for a desired user and three interfering users. First, we consider the scenario where all the three interferers are at the same position at the room center, and change the desired user's position from $d = 0$ to 5.7 m, i.e., from the center of the room to the corner, as shown in Fig. 4.6. These two positions correspond to the least and most MAI, respectively.

#### 4.5.2.1 Fixed Tx Orientation

At first, we assume that all Txs are oriented towards the ceiling i.e., $\theta_{tx} = 0$, regardless of their position. For a given $d$, the BER is calculated from (4.8). The BER plots of the desired user are presented in Fig. 4.7 for different transmit power levels $P_{t(\text{opt})}$, which is set equal for all users. As expected, the BER increases as the desired user moves towards the room corner, where it undergoes the worst MAI due to the so-called near-far problem. At the most favorable position, i.e., at the room center $d = 0$, the link performance is practically limited by the least MAI (with no near-far problem) and noise. As expected, a better performance is obtained by increasing the transmit

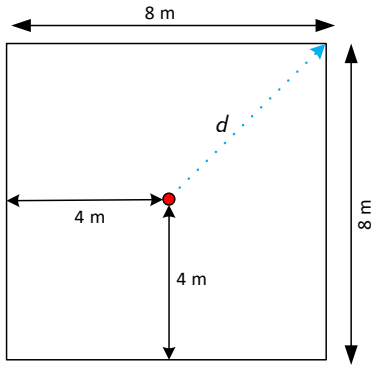


**Figure 4.6:** Trajectory of the displacement of the desired user from $d = 0$ (room center) to $d = 5.7$ m (room corner).

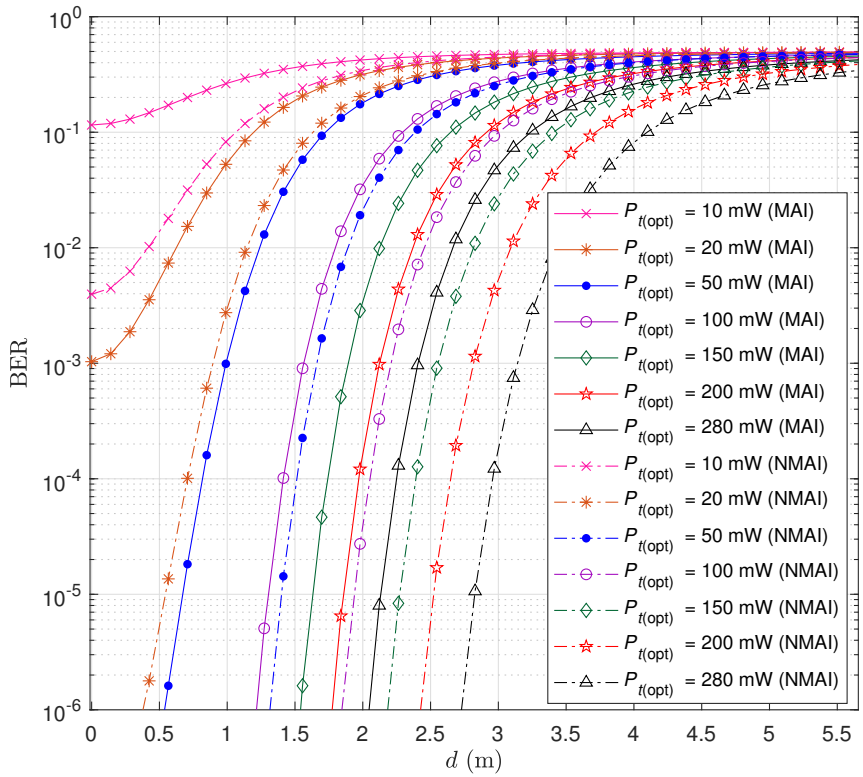


**Figure 4.7:** BER versus the horizontal distance $d$ of the desired user from the AP for different transmit powers. MAI represents the case where the three other users are located at the same position at the room center. NMAI stands for no-MAI. Only the LOS path is taken into consideration.

power. As benchmark, and in order to elucidate the MAI effect, we have also shown in Fig. 4.7 the BER plots for the no-MAI case, denoted by NMAI. Note that, for NMAI case, the increase in BER with $d$ is due to decrease in the received signal-to-noise-ratio (SNR), as it can be seen in Fig. 4.4 for $\theta_{tx} = 0$.

#### 4.5.2.2 Random Tx Orientation

Now we consider the effect of random Tx orientation for the same scenario as in the previous subsection. For this, we generate for every user $10^6$ Gaussian-distributed random values for yaw $\alpha$, pitch $\beta$, and roll $\gamma$ angles in the intervals of (-180°, 180°), (-60°, 60°) and (-60°, 60°), respectively. Given the random channel, we consider as performance metric the outage probability $P_{\text{out}}$, calculated considering $\text{BER}_{\text{th}} = 10^{-3}$. The $P_{\text{out}}$ plots are presented in Fig. 4.8 for different transmit powers $P_{t(\text{opt})}$. As expected, $P_{t(\text{opt})}$ increases as the desired user moves from the center of the room to the corner since there is a higher probability of losing the LOS, see Fig. 4.4. In fact, at the center, the performance is mainly affected by decreased SNR due to random orientations of the Tx, as shown in Fig. 4.5. Again, with increased $P_{t(\text{opt})}$, a lower $P_{\text{out}}$ is achieved for both MAI and no-MAI (NMAI) scenarios. However, almost the same results are obtained for $P_{t(\text{opt})} \geq 200$ mW (results are not shown for the sake of presentation clarity), which means that the limiting factor resulting in link outage is LOS blockage (rather than decreased SNR).

#### 4.5.2.3 Accounting for Non-LOS Contribution

So far, to show the impact of Tx orientation, we only considered LOS contribution to signal propagation. We now take into account non-LOS propagation by considering $1^{\text{st}}$-order reflections, which correspond to the major contribution from diffuse propagation. Higher-order reflections are neglected to avoid considerably increased simulation time. We consider that each wall is composed of a set of Lambertian reflecting surface elements, with 100 elements per square meter, which is sufficient for accurate channel estimation [123, 209].

We have shown the resulting $P_{\text{out}}$ plots in Fig. 4.9 for the same scenarios as in Fig. 4.8. We can notice the significant difference between the results of these two figures which signifies the substantial role of the diffuse link in the case of LOS blockage due to random Tx orientations. For instance, for $P_{t(\text{opt})} = 50$ mW at $d = 1$ m and MAI case, $P_{\text{out}}$ is around 0.6 from Fig. 4.8, whereas it is lower than 0.05 from Fig. 4.9. We also notice a leveling effect in $P_{\text{out}}$ as $d$ increases, irrespective of $P_{t(\text{opt})}$. This is due to the fact that the power received from the first-order reflections increases with increasing $d$, as the corresponding path length (reflections from walls) decreases, whereas the probability of LOS blockage increases (as shown in Figs. 4.4 and 4.5). Note that, at the extreme room corner, the calculated $P_{\text{out}}$ from the simulations steeply increases to one, which is due to considering only $1^{\text{st}}$-order reflections in our simulations. To obtain more accurate simulations, higher-order reflections need to be taken into account, which will considerably increase the simulation time. Nevertheless, such user positions are very unlikely to occur in practice, due to the

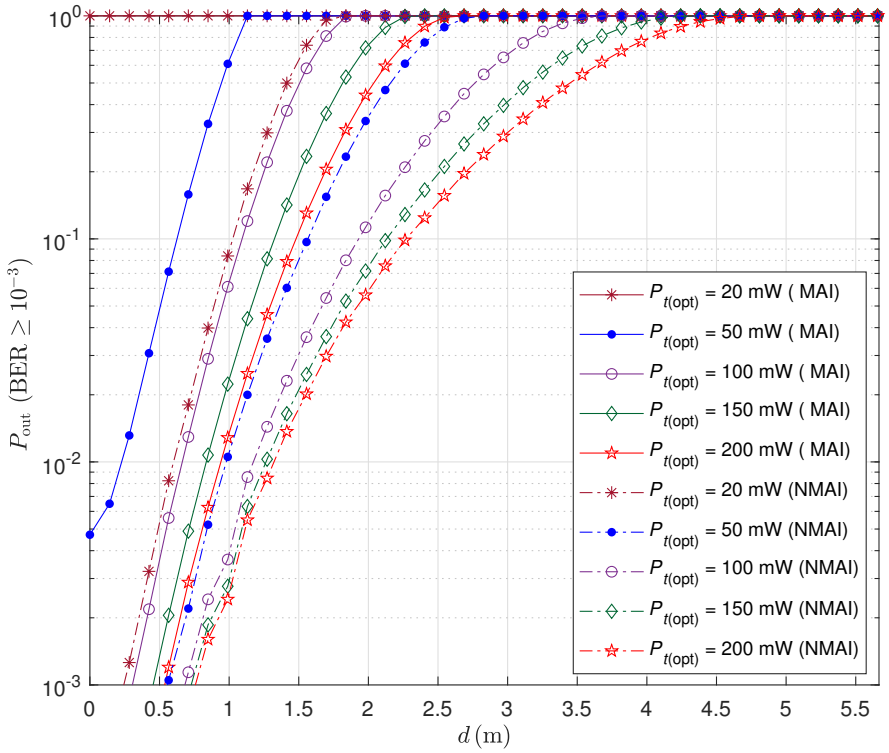


**Figure 4.8:** Outage probability versus the horizontal distance of the desired user from the AP for different transmit powers. MAI represents the case where the three other users are located at the same position at the room center. The three interferers and the desired user are oriented randomly at their positions. Only the LOS path is taken into consideration.

user's body volume. For this reason, we have excluded these values ($d \gtrsim 5.5$ m) in Fig. 4.9 and the subsequent figures.

In order to better see the impact of MAI, we have shown in Fig. 4.10 $P_{\text{out}}$ plots versus $d$ for different numbers of users $\mathscr{L}$, for $P_{t(\text{opt})} = 50$ mW and the MAI configuration as in Figs. 4.8 and 4.9, taking into account both LOS and LOS+1$^{\text{st}}$-order reflections. Note that, $\mathscr{L} = 1$ corresponds to NMAI case. As expected, $P_{\text{out}}$ degrades with increased number of interferers.

#### 4.5.2.4 Accounting for Random User Movements

Up to now, we considered fixed interferers' positions (in the center of the room, i.e., the worst MAI case) to better see the impact of MAI and random Tx orientations. In order to investigate the actual effect of MAI in a more practical scenario, we consider now randomly moving interferers according to the ORWP model (see in Chapter 2, Section 2.3.2) for a given position of a desired user. The speed variation interval and the pause time for the ORWP model are specified in Table 4.1. As before, we change the position of the desired user from the center of the room to the corner. Results are presented in the Fig. 4.11, where we have generated $10^6$ random positions of the

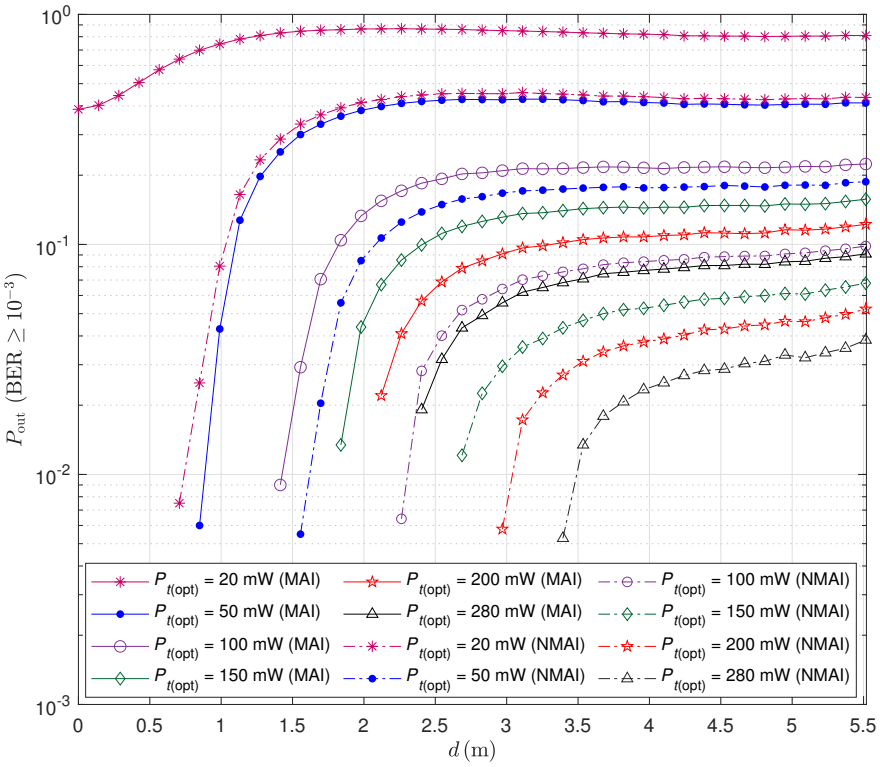


**Figure 4.9:** Outage probability versus the horizontal distance of the desired user from the AP, taking into account LOS and 1st-order reflections. MAI represents the case where the three other users are located at the same position at the room center. The three interferers and the desired user are oriented randomly at their positions.

interferers, as well as $10^6$ random orientations for the main user and the interferers. Compared with the case in Fig. 4.9, here we observe a slightly less destructive MAI effect on the desired user's link performance. This could be expected as in the present case, we consider randomly moving interferers where the MAI effect will be less significant overall, in particular, for relatively small $d$. Also, the worst MAI case in Fig. 4.9 (where the interferers and the desired user are all located at the room center) does not happen here since the interferers are considered to move randomly in the room.

### 4.5.3 Interest of Using Multiple APs

So far we showed how significantly the existence of a LOS between the Tx and the AP can improve the link performance. Indeed, we concluded that link outages mostly occur due to Tx random orientations, where the LOS is lost and the received signal (from reflections) is too weak. One efficient technique to reduce this "fading" effect is to employ spatial diversity by using multiple APs. To evaluate the obtained performance improvement, we consider the case of two and four APs placed symmetrically on the ceiling, as shown in Fig. 4.12. We perform equal gain combining

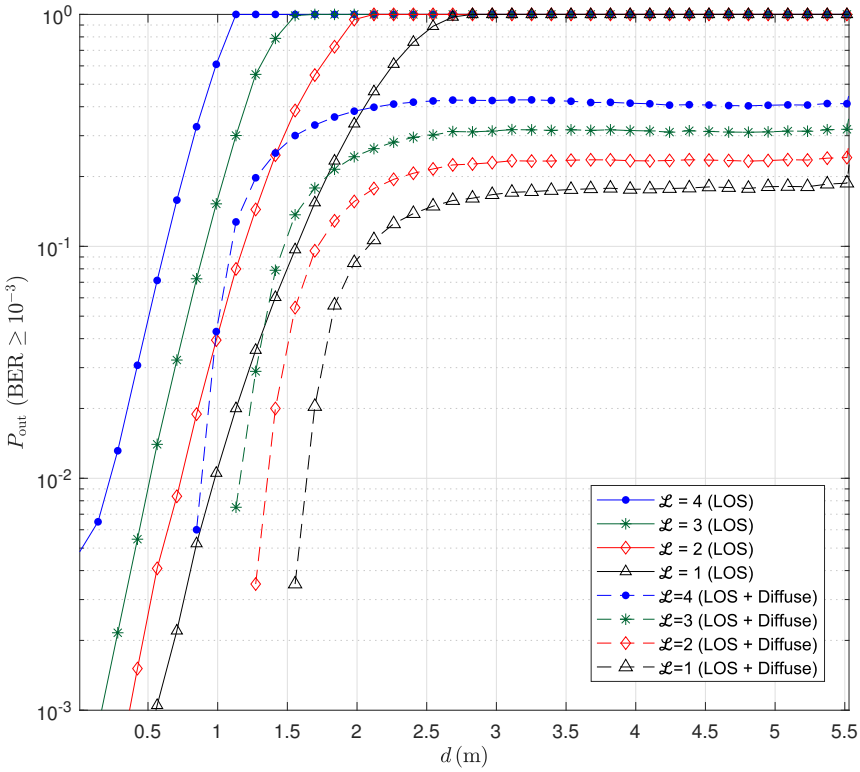


**Figure 4.10:** Outage probability versus the horizontal distance of the desired user from the AP for different numbers of users $\mathscr{L}$. Interferers are located at the same position at the room center. $P_{t(\text{opt})} = 50$ mW. The three interferers and the desired user are oriented randomly at their positions.

(EGC) on the signals received on the APs, assuming their perfect synchronization. Note that EGC provides performance close to the optimal maximal-ratio combining, while having a lower implementation complexity [199]. The assumption of perfect time synchronization is quite logical in this context: considering a maximum data-rate of 100 Kbps and the OOC code length of 49, the slot duration of the BPPM O-CDMA signal is about 100 ns. So, even a path length difference of 5 m between the Tx and the two APs in Fig. 4.12(a) would result in a maximum delay difference of about 15 ns, which can be effectively neglected.

We have presented the $P_{\text{out}}$ plots in Figs. 4.13 and 4.14 for the cases of 2 and 4 APs with and without MAI, respectively. By comparing these results with Fig. 4.11, we notice firstly that for relatively large $d$ where the $P_{\text{out}}$ degrades due to low received signal power, here spatial diversity helps improve the signal quality and the link $P_{\text{out}}$. Here, as illustrated in Fig. 4.12, the shortest distance between the desired Tx and an AP is $d \approx 1.4$ and 2.8 m for the cases of 2 and 4 APs, respectively, at which we notice the lowest $P_{\text{out}}$ for a given $P_{t(\text{opt})}$. Therefore, as the desired user moves from the center of the room to the corner, $P_{\text{out}}$ decreases at first, due to the decreasing distance between the Tx and an AP. Then, as the distance between the Tx and the AP increases, $P_{\text{out}}$ increases. This explains the non-monotonic trend of $P_{\text{out}}$ plots in Figs. 4.13 and 4.14 with $d$. Note that as explained

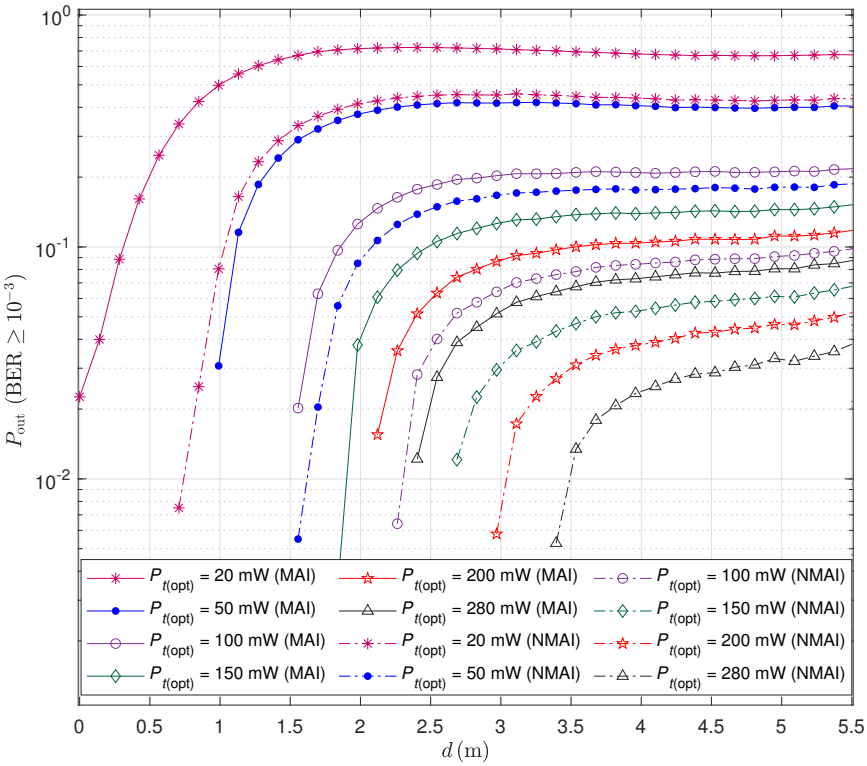


**Figure 4.11:** Outage probability versus the horizontal distance of the desired user from the AP, taking into account LOS and 1st-order reflections. The three interferers are randomly moving and oriented based on the ORWP mobility model inside the room; the desired user is randomly oriented at each position.

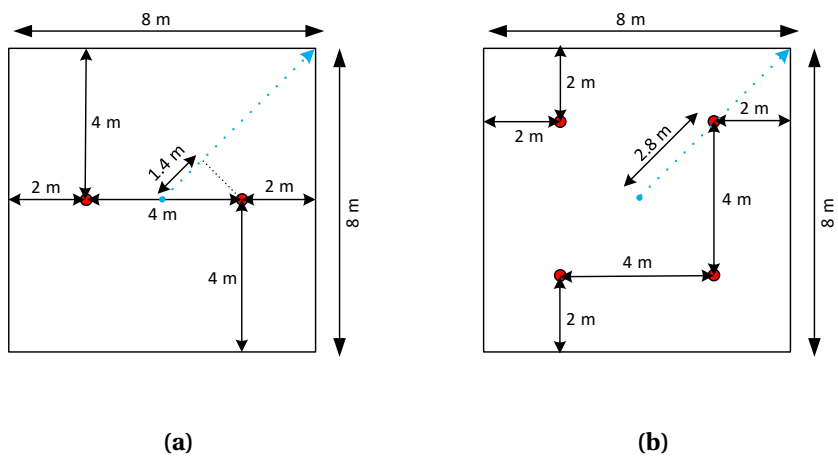


**Figure 4.12:** Arrangements of APs on the ceiling for the room size $(8 \times 8 \times 3)$ m$^3$: (a) case of 2 APs, (b) 4 APs. Here, dotted blue line represents the horizontal distance $d$ from the center of the room.

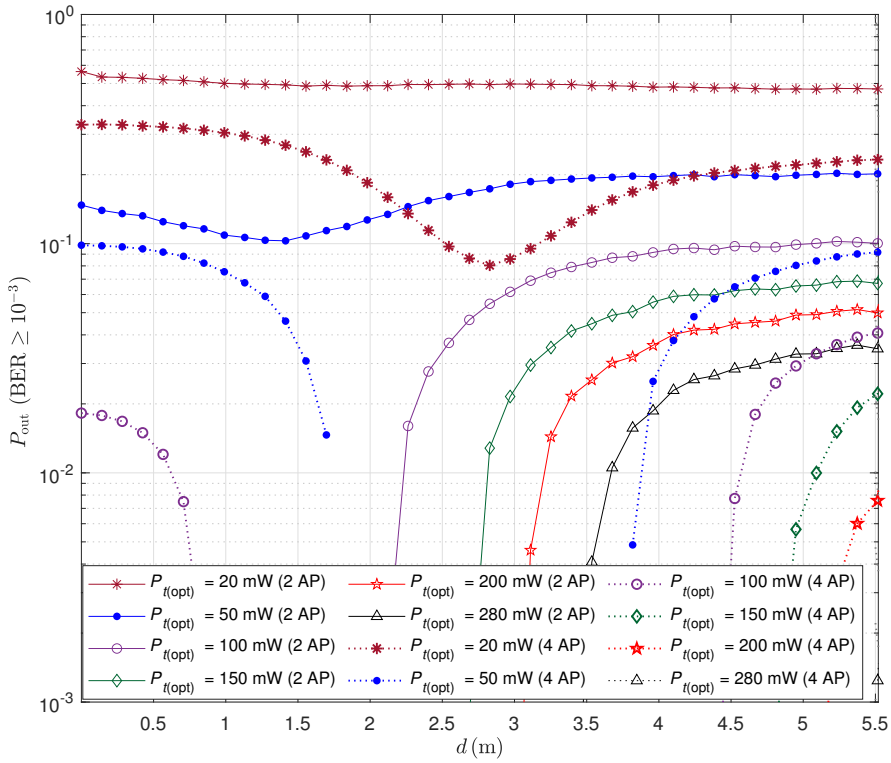


**Figure 4.13:** Outage probability versus the horizontal distance of the desired user from the center of the room for the 2 and 4 AP configurations, considering LOS+1$^{\text{st}}$-order reflections. Three randomly moving and oriented interferers based on the ORWP mobility model; randomly oriented desired user at each position.

previously in Subsection 4.5.2.3, the results at the extreme corner are excluded from these figures.

Lastly, we consider a realistic scenario where all users move randomly according to the ORWP model (with random speed and pause time) inside the room and random Tx orientations. $P_{\text{out}}$ plots are presented in Fig. 4.15 for different $P_{t(\text{opt})}$ and for the cases of 1, 2, and 4 APs when only LOS or LOS and 1$^{\text{st}}$-order reflections are considered for signal propagation. The interesting result is that the contribution of the diffuse link (i.e., non-LOS) becomes much more significant by increasing the number of APs. It is quite marginal for the case of a single AP, which is consistent with the results of Fig. 4.11. This substantial improvement for the case of multiple APs can be explained by a globally shorter path length to at least one AP from the 1$^{\text{st}}$-order reflection when the LOS is lost.

## 4.6 Chapter Summary and Discussions

In this chapter, we investigated the performance of BPPM O-CDMA based uplink extra-WBAN signal transmission for multi-user medical applications. We studied the impact of Tx orientation and changing positions of the users (both the desired user and the interferers) with respect to the AP, according to a realistic ORWP mobility model, and evaluated the effect of MAI on a desired

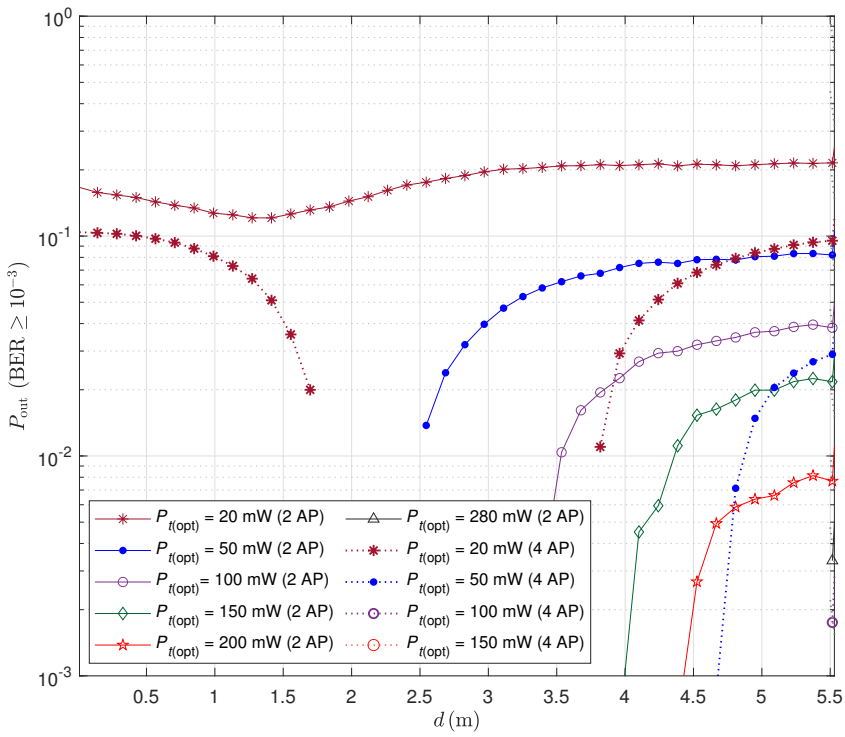


**Figure 4.14:** Outage probability versus the horizontal distance of the desired user from the center of the room for the 2 and 4 AP configurations for the case of NMAI. The desired user is oriented randomly at each position. LOS+1$^{\text{st}}$-order reflections are considered.

user performance. For this, we considered two cases where only the LOS or the LOS plus 1$^{\text{st}}$-order reflections were taken into account. In our analysis, for the sake of simplicity of analytical derivations, we considered the case of chip synchronous transmission, which corresponds the worst MAI conditions.

We showed that random Tx orientations have a more detrimental effect on the link performance (i.e., link outage due to LOS blockage) as the distance between the AP and the CN increases. We showed the substantial improvement in the link performance by using several APs in the room, albeit the increased system implementation complexity. In the meanwhile, we elucidated the important contribution of the 1$^{\text{st}}$-order reflections in the link performance.

Considering a relatively large number of users, as mentioned earlier, in O-CDMA, the required code length increases with the increased number of users, resulting in implementation complexity. For instance, assuming the number of users $\mathscr{L} = 10$, the minimum required OOC code length should be 901 (calculated using (4.3) and (4.4)), which will result in a significant increase in the required transmission bandwidth. Thus, in this context, we propose the use of OFDMA-based schemes. However, as we have shown in Chapter 3, O-OFDMA requires the use of HS in order to obtain a real TD signal, resulting in increased hardware complexity. In the next chapter, we will present the proposed new technique, i.e., O-ROFDMA, where no HS is imposed. Moreover, we

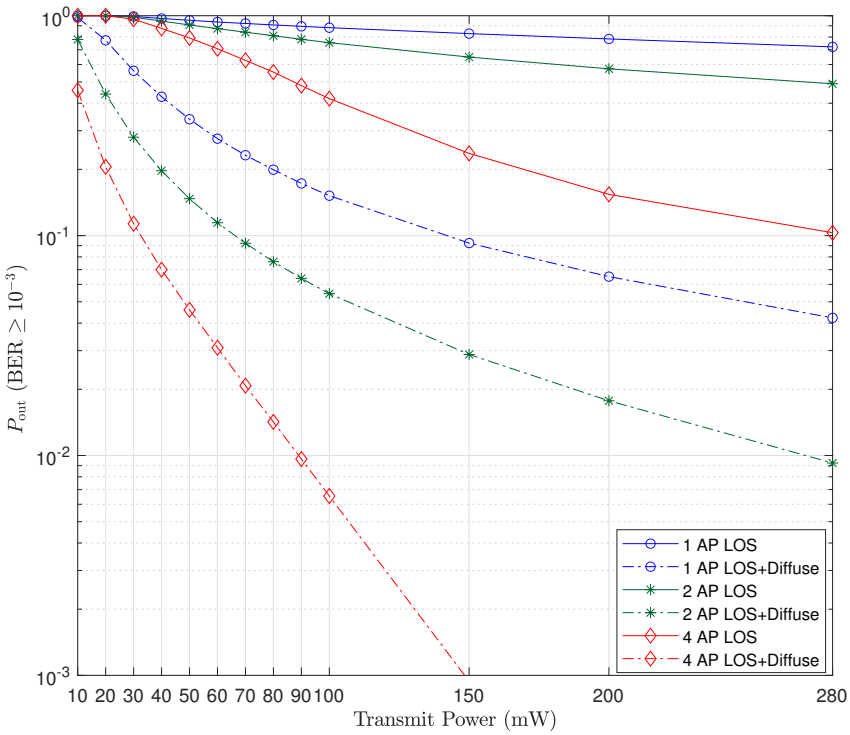


**Figure 4.15:** Outage probability versus the transmit power $P_{t(\text{opt})}$ with randomly moving and oriented desired user and interferers for the cases of one, two, and four APs based on the ORWP mobility model. Two cases of LOS and LOS+ 1$^{\text{st}}$-order reflections are considered.

will investigate the performance and computational complexity of the scheme, as compared to its O-OFDMA and O-SCFDMA counterparts for an emergency waiting room scenario.

# Chapter 5

# Energy-Efficient O-OFDMA Scheme for Medical Extra-WBANs

**Contents**


**5.1 Introduction** . . . . . **77**
**5.2 System Description** . . . . . **78**
5.2.1 General Assumptions . . . . . 78
**5.3 Description of the Proposed MA Scheme** . . . . . **80**
5.3.1 DCO-ROFDMA . . . . . 81
5.3.2 ACO-ROFDMA . . . . . 82
5.3.3 Setting DC Bias and Clipping . . . . . 82
**5.4 Performance Analysis** . . . . . **83**
5.4.1 Parameter Specification and Performance Metrics . . . . . 83
5.4.1.1 PAPR . . . . . 84
5.4.1.2 Transmit Power and Electrical Energy . . . . . 84
5.4.1.3 Spectral Efficiency . . . . . 84
5.4.2 PAPR Analysis . . . . . 84
5.4.3 BER Performance . . . . . 85
5.4.3.1 DCO Signaling . . . . . 85
5.4.3.2 ACO Signaling . . . . . 86
5.4.4 Electrical Power Efficiency . . . . . 88
**5.5 Elucidating MAI effect** . . . . . **88**
**5.6 Complexity Analysis** . . . . . **90**
**5.7 Chapter Summary** . . . . . **94**


## 5.1 Introduction

In this chapter, we propose a MA scheme for extra-WBAN uplink, which does not need to apply the HS constraint to the FD signal, which is an extension of the scheme introduced in [210]. Note that other already proposed HS-free O-OFDM solutions typically transmit data by juxtaposing real

and imaginary parts in the TD [211, 212]. With our new scheme, called O-ROFDMA, only the real part of the TD signal is transmitted. We show the advantage of this scheme compared with O-OFDMA and O-SCFDMA in terms of PAPR, BER, power efficiency, and computational complexity. For this, we take into account the limited DR of the LED and evaluate the performance of these schemes for both DCO and ACO signaling, in particular, due to MAI. The superior performance of ACO-ROFDMA is demonstrated by studying its outage probability taking into account random Tx orientations for an emergency waiting room scenario.

In Section 5.2, we present the system description in the context of the emergency waiting room scenario. Next, Section 5.3 describes in detail the proposed O-ROFDMA scheme. Afterwards, Sections 5.4 presents the performance analysis results of O-ROFDMA in order to study PAPR, BER, electrical power efficiency, and MAI effect. At first, we investigate the performance of the scheme compared to its O-OFMDA and O-SCFDMA counterparts. We show that O-ROFDMA has nearly the same performance as the O-OFDMA scheme. Meanwhile, we investigate the electrical power efficiency of ACO and DCO signaling in terms of electrical transmit power, showing the superiority of ACO signaling. The effect of MAI on the ACO-ROFDMA scheme is then evaluated in the presence and absence of random Tx orientations. Next, Section 5.6 discusses the computational complexity of the schemes. Lastly, Section 5.7 concludes the chapter.

## 5.2 System Description

### 5.2.1 General Assumptions

An illustration of a typical emergency waiting room scenario in hospital with potentially up to sixteen patients inside is shown in Fig. 5.1. IR extra-WBAN links send medical information from the patients to an AP placed on the ceiling.

For the sake of simplicity and to focus on the performance of MA schemes, we consider only a single AP, i.e., a single-cell with radius of $r_{\text{cell}}$. For larger spaces, multiple APs can be used in a multi-cell [213, 214] or a single-cell [215] architecture. CNs are assumed to transmit the medical data at a rate of 500 Kbps for the extra-WBAN link, which satisfies the requirement of most health monitoring sensors, e.g., temperature, blood pressure, ECG, and SPO2, presented in Chpater 1.

At the Tx (i.e., CN) side, we consider the use of low-power IR LEDs (having a relatively wide beam), due to eye-safety issues given the relatively large number of patients in the emergency waiting room. We consider a commercial IR LED as in [216], with a wavelength of 850 nm and maximum radiant intensity of 6.4 mW/sr. Considering the simultaneous transfer of data from sixteen patients, the CNs equipped with such LEDs meet the IEC eye-safety requirement, see Chapter 2.

We assume that each CN is perfectly time synchronized with the AP. Note that RF OFDMA requires multi-user time and frequency synchronization (with all users) in order to avoid MAI and near-far problems, this is usually referred to as initial ranging [217]. However, the inherent absence of a carrier in O-OFDMA removes the need for frequency synchronization [218]. On the other

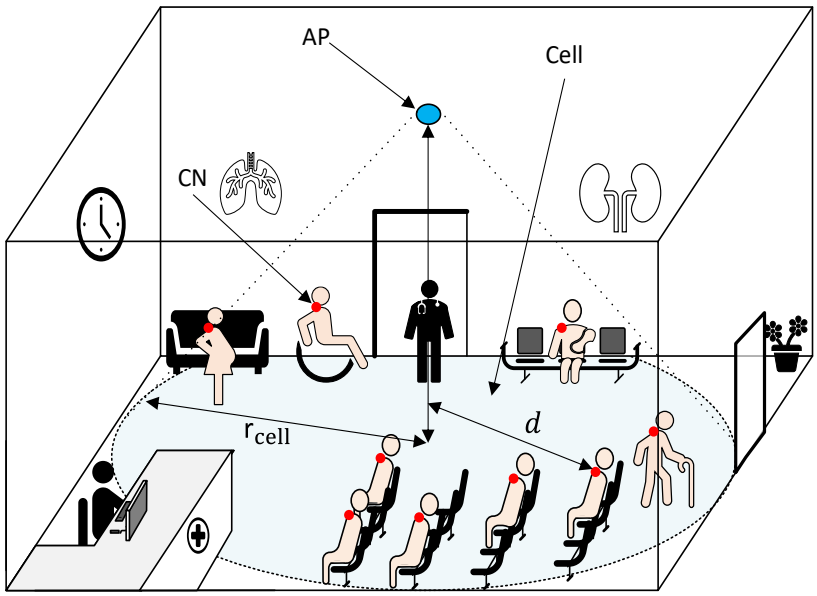


**Figure 5.1:** Illustration of a health monitoring system in an emergency waiting room scenario by using IR extra-WBAN uplink for multiple patients, each one with a CN on the shoulder (the red bullet). A single AP is considered, placed on the ceiling. Here, $d$ is the distance between the patient (i.e., the CN) and the cell center.

hand, a number of timing synchronization methods are reported in the literature [218–221], which are mainly based on the transmission of training sequences, also used to acquire the channel state information (CSI)[1]. We assume that the AP has a perfect knowledge of the CSI of all CNs.

We consider only the LOS link and neglect the non-LOS components for the sake of simulations simplicity. Indeed, given the relatively large dimensions of the emergency waiting room that we consider here, the contribution of non-LOS propagation to the received signal is rather negligible.

Given the transmit optical power $P_{t(\text{opt})}$ and the PIN PD responsivity $\mathscr{R}$, for the considered LOS link, the received photo-current is [49]:

$$i_{\mathfrak{r}} = \mathscr{R} H_{\text{LOS}} P_{t(\text{opt})}. \tag{5.1}$$

Given the load resistance of the Rx TIA by $R_L$, the received electrical power $P_{\mathfrak{r}}$:

$$P_{\mathfrak{r}} = i_{\mathfrak{r}}^2 R_L. \tag{5.2}$$

Considering a PIN PD at the AP, the background and thermal noises are the dominant noise sources, which can be modeled as zero-mean additive white Gaussian [103] with the one sided noise PSD $N_0$ as follows [49]:

$$N_0 \approx 4K_B T_r / R_L + 2q_e I_a, \tag{5.3}$$

[1]Training sequences from each CN can be sent to the AP in the uplink, based on which the estimated CSI at the AP is sent to the CNs via the downlink (which typically benefits from a higher SNR). Different wavelengths can be used for the uplink and downlink to avoid interference, e.g., VL can be used in the downlink.

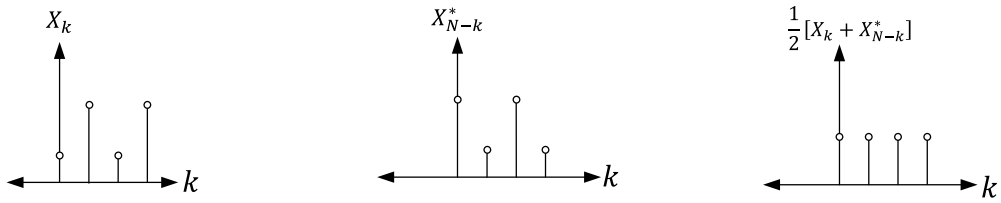


**(a)** Real-valued FD signal **(b)** Complex conjugate & reversed **(c)** Aliasing in recovered signal

**Figure 5.2:** FD aliasing in a recovered signal from the real part of its IFFT output: (a) Real-valued subcarriers in a FD signal, where the total number of subcarriers $N$= 4, (b) The complex conjugate and time-reveresed version of the FD signal, (c) The FFT output signal taking into account only the real part, showing FD aliasing.

## 5.3 Description of the Proposed MA Scheme

As mentioned previously, in our proposed ROFDMA scheme, only the real part of the TD signal (after IFFT) is transmitted, hence removing the need for HS. Let us first explain the theoretical foundation of recovering a FD signal from the real part of its IFFT. Consider the FD symbols $X_k$ after subcarrier mapping without imposing HS, and the corresponding TD signal $x_{n'}$, $n' = 0, 1 \ldots, N-1$. We have [222]:

$$\begin{cases} \frac{1}{2}\left[X_k + X^*_{N-k}\right] \xrightarrow{\text{IFFT}} \Re\{x_{n'}\} \\ \frac{1}{2}\left[X_k - X^*_{N-k}\right] \xrightarrow{\text{IFFT}} j\Im\{x_{n'}\}. \end{cases} \tag{5.4}$$

Here, $X^*_{N-k}$ refers to the complex conjugate and time-reversed version of $X_k$. Also, $\Re\{\cdot\}$ and $\Im\{\cdot\}$ stand for the real and imaginary parts, respectively. Given (5.4), it is obvious that recovering $X_k$ from the real part of $x_{n'}$ alone is not possible without the imaginary part. This is due to the complex-conjugate term $X^*_{N-k}$ that overlaps with the subcarriers $X_k$ and causes FD aliasing, as illustrated in Fig. 5.2.

The effect of aliasing can be avoided by padding a zero at the begining of the symbol frame $X_k$ and an adequate number of zeros (at least $N$) at the end [223][2]. This increases the number of subcarriers for IFFT to $\mathcal{N} \geq 2N+1$. Based on this, Fig. 5.3 illustrates the reconstruction of the FD signal from the real part of the TD signal. Given the real-valued FD symbols $X_k$ in Fig. 5.3a, the symbols $\tilde{X}_{\hat{k}}$ of the extended frame (with zero padding, in Fig. 5.3b) are given by:

$$\tilde{X}_{\hat{k}} = \begin{cases} 0 & ;\ \hat{k} = 0, \\ X_{\hat{k}-1} & ;\ \hat{k} = 1, 2 \ldots, N, \\ 0 & ;\ \hat{k} = N+1, \ldots, \mathcal{N}-1. \end{cases} \tag{5.5}$$

[2]Note that, it is essential to pad a zero at the beginning of the frame if the signal is complex-valued [223].

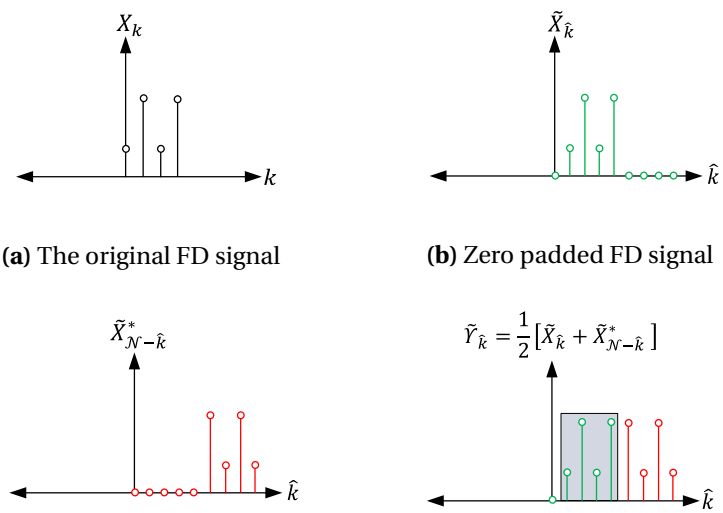


**(a)** The original FD signal

**(b)** Zero padded FD signal

**(c)** Complex conjugate & reversed

**(d)** FFT output

**Figure 5.3:** Recovering a FD signal from the real part of its zero-padded IFFT output: (a) Real-valued subcarriers in a FD signal, where the total number of subcarriers $N = 4$, (b) The FD signal is extended to $2N+1$ by adding zero-padded subcarriers, (c) The complex conjugate subcarriers of the zero-padded FD signal are mapped in reverse-order, (d) The FFT output of the signal taking into account only the real part, showing no FD aliasing. The shaded region shows the recovered signal $X_k$.

Due to zero padding, there will be no FD aliasing between the complex conjugate and time-reversed version of the signal $\tilde{X}_{\hat{k}}$ (see Fig. 5.3c), allowing the correct recovery of the original signal $X_k$, as it can be seen in Fig. 5.3d.

### 5.3.1 DCO-ROFDMA

Figure 5.4 shows the block diagram of DCO-ROFDMA signaling. The mapped subcarriers $X_k$ in the FD signal are zero-padded (before the IFFT block) instead of imposing HS[3] as in (5.5). Then, only the real part of the TD signal, i.e., $\Re\{x_n\}$ block in Fig. 5.4, is prepared for the transmission and follows the same steps described for DCO-OFDMA in Chapter 3.

At the Rx side, the signal processing steps are similar to those of DCO-OFDMA up to the FFT block. The FD signal $\tilde{Y}_{\hat{k}}$ is recovered by performing FFT only on $\Re\{x_n\}$, as shown in Fig. 5.3d, given by:

$$\tilde{Y}_{\hat{k}} = \begin{cases} X_{\hat{k}-1} & ;\ \hat{k} = 1, 2, \ldots, N, \\ X^*_{\mathcal{N}-1-\hat{k}} & ;\ \hat{k} = N+1, \ldots, \mathcal{N}-1, \\ 0 & ;\ \text{elsewhere.} \end{cases} \tag{5.6}$$

[3]Note that, in order to keep the same spectral efficiency as for the conventional MA schemes which employs HS, we add one extra zero at the end of the frame $\tilde{X}_{\hat{k}}$ such that $\mathcal{N} = 2N+2$.

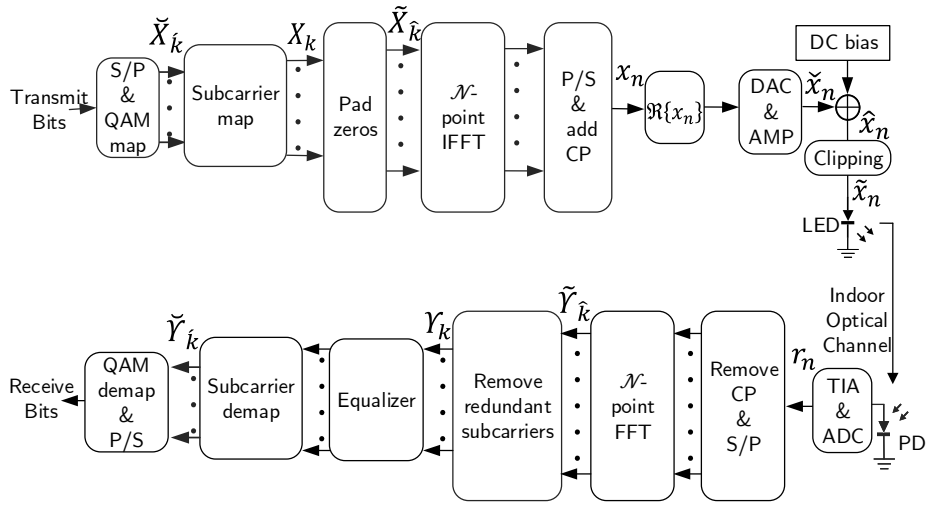


**Figure 5.4:** Block diagram of the DCO-ROFDMA signaling scheme.

After the FFT block in Fig. 5.4, the transmitted symbols from $\Upsilon_k$ are recovered such that:

$$\Upsilon_k = \tilde{\Upsilon}_k; \quad k = 1, 2, \ldots, N. \tag{5.7}$$

Then, channel equalization, subcarrier- and QAM-demapping are performed in order to recover the transmit bits.

### 5.3.2 ACO-ROFDMA

In ACO-ROFDMA, after zero padding, the transmit symbols $\tilde{X}_{\hat{k}}$ before the IFFT block have the same frame structure as explained for ACO-OFDMA except that only even subcarriers are used to transmit data:

$$\tilde{X}_{\hat{k}} = \Big[0, 0, X_0, 0, X_1, 0, \ldots, X_{N-1}, 0, \underbrace{0, \ldots, 0}_{(2N+2)\text{ times}}\Big].$$

The rest of the processing steps are the same as described for DCO-ROFDMA. Note that, in contrast to the scheme presented in [210], it is essential to transmit information in the even subcarriers to ensure orthogonal cardinal sine (sinc) shape.

### 5.3.3 Setting DC Bias and Clipping

In practice, a DC bias is added to the TD signal in order to adapt the signal to the LED DR [120]. We consider a commercial LED model HDN1102W-TR, with the I-V characteristics shown in Fig. 5.5 [216]. Note that the LED operates almost linearly within the voltage range of 1.38 to 1.62 V. For the sake of simplicity, we consider the approximate linearized characteristics in our analysis, (the red plot in the figure).[4] Considering these lower and upper clipping levels, we set $\mathscr{B}_{\text{DC}}$= 1.38 V for ACO schemes. For DCO schemes, we set $\mathscr{B}_{\text{DC}}$ to the mid point between the upper and lower

[4]Note that a digital predistorter can be employed at the Tx to reduce the effect of LED non-linearity [224].

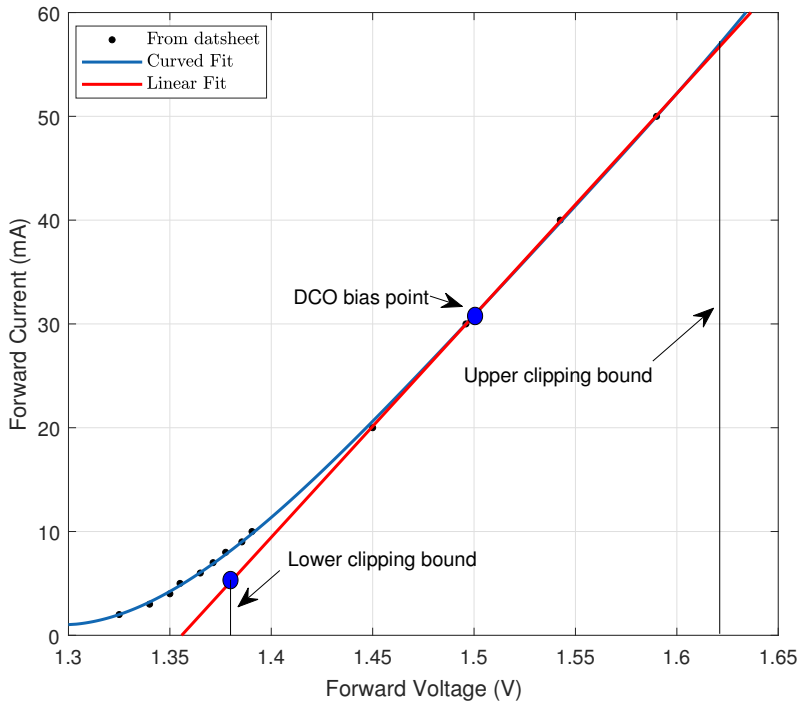


**Figure 5.5:** I-V characteristics of the LED, HDN1102W-TR [216].

clipping bounds, i.e., 1.5 V, to affect the TD signal equally. The part of electrical transmit power corresponding to the DC bias equals 7 mW and 46.2 mW for ACO and DCO schemes, respectively.

## 5.4 Performance Analysis

### 5.4.1 Parameter Specification and Performance Metrics

We present here a set of numerical results to study the performance of the proposed O-ROFDMA scheme for extra-WBANs in the emergency waiting room scenario. We consider the number of patients $\mathscr{L} = 16$ and bit rate $R_b = 500$ Kbps per user. Also, $\mathscr{M} = 4$ subcarriers per user are considered with the total number of subcarriers $N = 64$. The other simulation parameters are summarized in Table 5.1, where the LED parameters correspond to the I-V characteristics in Fig. 5.5. Note that we consider 8-bit ADC and DAC and the presented numerical results take into account the corresponding quantization noise. Also, unless otherwise specified, for the sake of simulation simplicity, the CNs are considered to point straight upward (towards the ceiling), i.e., $\theta_{tx} = 0$ in Fig. 2.6. Remember that, interleaved subcarrier mapping is applied to each user symbols, as described in Chapter 3.

#### 5.4.1.1 PAPR

The signal PAPR is considered here as the ratio between the peak electrical power of the TD signal (before clipping) to its average power defined as $E\{x_n^2\}$. The PAPR performance is typically studied by considering its complementary cumulative distribution function (CCDF) [225], defined as the probability that the PAPR exceeds a target value, $\text{PAPR}_0$.

#### 5.4.1.2 Transmit Power and Electrical Energy

The link performance is evaluated in terms of the average BER as a function of the electrical transmit power $P_{t(\text{elec})} = E\{\tilde{x}_n^2\}$ or the electrical SNR per bit, $E_{b(\text{elec})}/N_0$, where $E_{b(\text{elec})} = P_{t(\text{elec})}/R_b$. Note, $P_{t(\text{elec})} = P_{t(\text{opt})}/\wp$ with $\wp$ being the electrical-to-optical power conversion efficiency of the LED. As mentioned earlier, for random link scenarios (e.g., the case of randomly-oriented Txs, presented later), the outage probability, i.e., $P_{\text{out}}$, is considered.

#### 5.4.1.3 Spectral Efficiency

Due to the limited modulation bandwidth (BW) of the LED, an important parameter is the required BW per user, which depends on the signaling scheme. Considering $M$-QAM constellation, the spectral efficiencies of DCO and ACO schemes are [119]:

$$\Gamma_{\text{DCO}} = \frac{\log_2(M)N}{\mathcal{N} + \mathcal{N}_{\text{CP}}}, \quad \Gamma_{\text{ACO}} = \frac{\log_2(M)N}{2\mathcal{N} + \mathcal{N}_{\text{CP}}} \quad \text{(bps/Hz)}. \tag{5.8}$$

Remember that $\mathcal{N} = 2N + 2$ with $N$ the number of mapped subcarriers. As ACO schemes use only half of the subcarriers, the corresponding spectral efficiency will be half of the corresponding DCO scheme, keeping the same constellation size and number of subcarriers. To make a fair comparison between DCO and ACO-based schemes, we fix the spectral efficiency by setting $M$ accordingly. The spectral efficiencies per user are then given by $\Gamma_{\text{DCO}}/\mathcal{L}$ and $\Gamma_{\text{ACO}}/\mathcal{L}$, with the corresponding required BWs per user as:

$$B_{\text{DCO}} = \frac{R_b}{\Gamma_{\text{DCO}}/\mathcal{L}} = \frac{R_b\mathcal{L}}{\Gamma_{\text{DCO}}}, \quad B_{\text{ACO}} = \frac{R_b\mathcal{L}}{\Gamma_{\text{ACO}}}. \tag{5.9}$$

### 5.4.2 PAPR Analysis

Let us first compare the PAPR of the proposed O-ROFDMA scheme with O-OFDMA and O-SCFDMA. Results are shown in Fig. 5.6 for 16-QAM modulation for the case of DCO signaling and different numbers $\mathcal{M}$ of data carrying symbols. We notice that the PAPR performances of DCO-ROFDMA and DCO-OFDMA are almost the same, while being largely outperformed by DCO-SCFDMA, as expected. Also, as expected, PAPR increases with increased $\mathcal{M}$. Given the typically small number of symbols $\mathcal{M}$ for low data-rate medical applications, we can conclude that the signal PAPR remains relatively low. Note that for low CCDF values, the PAPR is almost the same regardless of the constellation size, in particular, for small $\mathcal{M}$ (results not shown).

**Table 5.1:** Parameters used for numerical simulations.

| Parameter | Symbol | Value |
|---|---|---|
| Max. number of users | $\mathscr{L}$ | 16 |
| Data-rate per user | $R_b$ | 500 Kbps |
| Cell radius | $r_{\text{cell}}$ | 3 m |
| CN height | $h_{\text{CN}}$ | 1 m |
| AP height | $h_{\text{AP}}$ | 3 m |
| LED wavelength [216] | $\lambda$ | 850 nm |
| LED semi-angle at half power | $\phi_{1/2}$ | 60° |
| LED BW [216] | — | 20 MHz |
| Power conversion efficiency [216] | $\wp$ | 0.8 |
| Tx orientation angle intervals | $\theta_{tx}$ | -60°–60° |
| PD responsivity | $\mathscr{R}$ | 0.6 A/W |
| PD active area | $A_d$ | 1 cm$^2$ |
| Rx FOV | $\psi_c$ | 70° |
| TIA resistor value | $R_L$ | 50 Ω |
| Background noise current [226] | $I_a$ | 200 µA |
| Rx noise temperature | $T$ | 300 K |
| No. of mapped subcarriers | $N$ | 64 |
| Subcarriers allocated per user | $\mathscr{M}$ | 4 |
| CP length | $\mathscr{N}_{\text{CP}}$ | 2 |
| DAC/ADC | — | 8 bits |
| DC-bias, DCO | $\mathscr{B}_{\text{DC(DCO)}}$ | 1.50 V |
| DC-bias, ACO | $\mathscr{B}_{\text{DC(ACO)}}$ | 1.38 V |
| Upper clipping | — | 1.62 V |
| Lower clipping | — | 1.38 V |
| Target BER | $\text{BER}_{\text{th}}$ | $10^{-3}$ |

### 5.4.3 BER Performance

To study the BER performance, we consider the most limiting case of maximum channel attenuation, i.e., when all users are placed at the cell edge, corresponding to $d = 3$ m from the center of the cell (see Fig. 5.1).

#### 5.4.3.1 DCO Signaling

In this case, given $\mathscr{L} = 16$ and $\mathscr{M} = 4$, $\mathscr{N} = 130$ after imposing the HS. Then, considering the data-rate per user $R_b = 500$ Kbps, we analyze the BER performance for 4-QAM, 16-QAM and 64-QAM constellations, corresponding to the spectral efficiencies $\Gamma_{\text{DCO}} \approx 1, 2$ and 3 bps/Hz, and the required transmission BW $B_{\text{DCO}} = 8, 4$ and 2.67 MHz, respectively. Figure 5.7 shows the BER performance versus $E_{b(\text{elec})}/N_0$ for different QAM orders, where we have fixed $P_{t(\text{elec})}$ to 48 mW, which ensures a low BER for DCO schemes, as we will later show in Subsection 5.4.4. We notice that the BER performances of DCO-OFDMA and DCO-ROFDMA are almost the same, while being out-

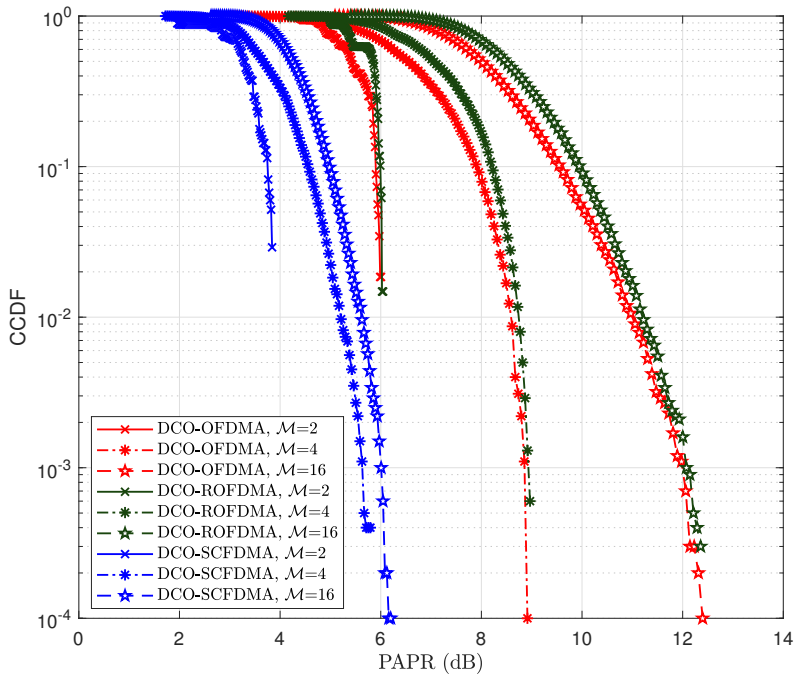


**Figure 5.6:** CCDF plots of PAPR for DCO-OFDMA, DCO-SCFDMA and DCO-ROFDMA schemes, considering different numbers of data-carrying symbols $\mathcal{M}$ per user and the 16-QAM constellation.

performed by DCO-SCFDMA, particularly, for 64-QAM. This is due to the relatively low PAPR in SCFDMA, resulting in low clipping noise.

#### 5.4.3.2 ACO Signaling

In this case, considering the same $R_b$ and QAM constellation size as for DCO schemes, the required transmission BWs are $B_{\text{ACO}} = 16, 8$ and 5.33 MHz, corresponding to the spectral efficiencies $\Gamma_{\text{ACO}} \approx 0.5, 1$ and 1.5 bps/Hz, respectively. Note that $B_{\text{ACO}}$ values are still below the considered LED BW of 20 MHz. Here, $\mathcal{N} = 258$ and $P_{t(\text{elec})}$ is set to 23 mW. In comparison to the DCO schemes, the required value of $P_{t(\text{elec})}$ decreases in ACO schemes due to the relatively low DC biasing, as explained in Subsection 5.4.4. Note that a BER comparison between ACO and DCO schemes does not make sense here, given the different $P_{t(\text{elec})}$ considered. Figure 5.8 shows the corresponding BER performances where we notice nearly the same performance for ACO-OFDMA and ACO-ROFDMA, while ACO-SCFDMA outperforms both for 64-QAM, as expected. For reduced $\Gamma_{\text{ACO}} \approx 0.5$ bps/Hz, lower SNRs are reasonably required to attain a target BER.

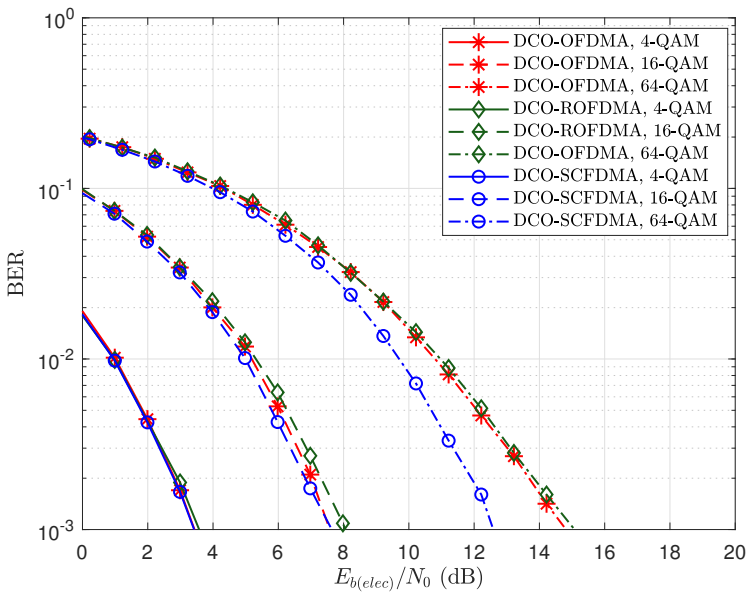


**Figure 5.7:** BER performance comparison of different DCO schemes, considering the spectral efficiency of ≈ 1 bps/Hz (4-QAM), 2 bps/Hz (16-QAM) and 3 bps/Hz (64-QAM) for the average electrical transmit power $P_{t(\text{elec})} = 48$ mW. The patients are considered to be placed at a distance of $d = 3$ m from the AP (at the cell edge).

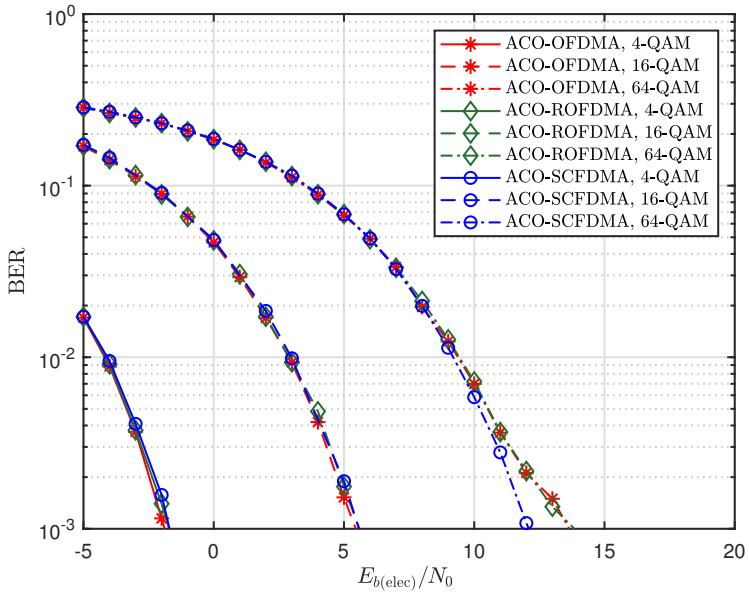


**Figure 5.8:** BER performance comparison of different ACO schemes, considering the spectral efficiency of ≈ 0.5 bps/Hz (4-QAM), 1 bps/Hz (16-QAM) and 1.5 bps/Hz (64-QAM) for the average electrical transmit power $P_{t(\text{elec})} = 23$ mW. The patients are considered to be placed at a distance $d = 3$ m from the AP.

### 5.4.4 Electrical Power Efficiency

Let us define the electrical power efficiency as the required $P_{t(\text{elec})}$ to achieve a target BER. We consider the same scenario as the previous subsection, where the users are placed at the same position at a distance $d = 3$ m. BER plots of the different considered schemes are compared in Fig. 5.9 for the spectral efficiency of $\approx 1$ bps/Hz, where 16-QAM and 4-QAM constellations are considered for ACO and DCO schemes, respectively. Here, $P_{t(\text{elec})}$ is changed by varying the amplitude of $x_n$ (see Fig. 5.4) taking into account $\mathscr{B}_{\text{DC}}$. To focus on the effect of signal clipping, we set relatively high $E_{b(\text{elec})}/N_0 = 15$ dB, which should potentially result in a low BER, as seen in Fig. 5.8.

One can notice the BER degradation at relatively large $P_{t(\text{elec})}$ due to the clipping noise.[5] Also, the ACO schemes require approximately 35 mW less $P_{t(\text{elec})}$ to obtain a target BER, compared to DCO schemes. The performance of SCFDMA is close to those of OFDMA and ROFDMA for both DCO and ACO signaling. Meanwhile, as expected, due to the low PAPR, SCFDMA is less impacted by clipping noise for relatively large $P_{t(\text{elec})}$.
Remember from Subsection 5.3.3 that, due to the added DC bias, the minimum required $P_{t(\text{elec})}$ for ACO and DCO schemes is 7 and 46.2 mW, respectively. The slope of the BER at relatively low $P_{t(\text{elec})}$ that is noticed for ACO schemes is due to the effect of the quantization noise due to the ADC at very low *effective* signal powers (i.e., excluding the part of the power related to $\mathscr{B}_{\text{DC}}$). This effect is rather negligible for a small constellation size, i.e., the case of DCO-schemes with 4-QAM. At the aforementioned $P_{t(\text{elec})}$ where the *effective* signal power equals zero, BER = 0.5.

Let us now compare the performance of ACO schemes for spectral efficiencies of $\approx 1$ and $\approx 0.5$ bps/Hz, as shown in Fig. 5.10. As expected, a lower $P_{t(\text{elec})}$ is required to attain a target BER for a lower spectral efficiency, which is due to using a smaller constellation size at the cost of increased signal BW. Moreover, for 4-QAM constellation ($\Gamma_{\text{ACO}} \approx 0.5$ bps/Hz) clipping noise affects the link performance for relatively large $P_{t(\text{elec})}$, while ACO-SCFDMA showing its superior performance due to the lower PAPR.

## 5.5 Elucidating MAI effect

To elucidate the effect of MAI, lets focus on ACO-ROFDMA as an appropriate transmission scheme due to its lower transmit power requirement (as shown in the results of Fig. 5.9). Figures 5.11a and 5.11b show the BER performances of a desired user with different distances $d$ from the cell center for $\Gamma_{\text{ACO}} \approx 0.5$ and 1 bps/Hz, respectively. The other 15 users are placed at the cell center (hence, potentially causing the maximum MAI), and the same $P_{t(\text{elec})}$ is set to all users. We have also presented as benchmark the BER plots for the case where there is only the desired user in the cell, indicated by NMAI. Obviously, the BER degrades by increasing $d$ due to the decrease in

[5] To go more into detail, the BER leveling effect around 0.3 that we observe at relatively high transmit powers for ACO schemes is due to signal clipping of "outer points" in the 16-QAM constellation. When $P_{t(\text{elec})}$ is increased too much (not shown in the figure), the BER jumps to 0.5 as all 16-QAM constellations points get clipped. Also, note that increasing too much the amplitude of $x_n$ does not necessarily result in an increase in $P_{t(\text{elec})}$, as this latter relies on the symbols after clipping.

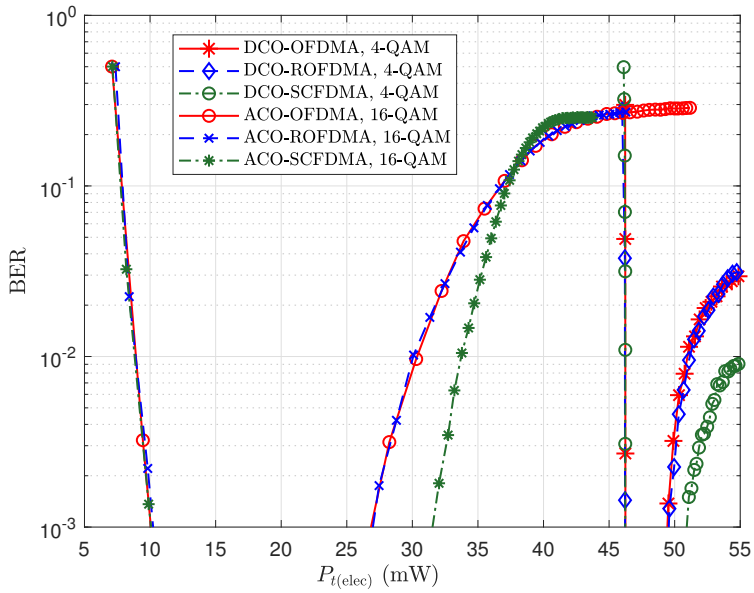


**Figure 5.9:** BER performance comparison between ACO and DCO schemes with respect to different average electrical transmit power $P_{t(\text{elec})}$ for a fixed $E_{b(\text{elec})}/N_0 = 15$ dB and the spectral efficiency of $\approx 1$ bps/Hz. Here, 16-QAM and 4-QAM constellation is considered with $\mathscr{M} = 4$ for ACO and DCO schemes, respectively. The patients are placed at the same position at a distance $d = 3$ m from the AP.

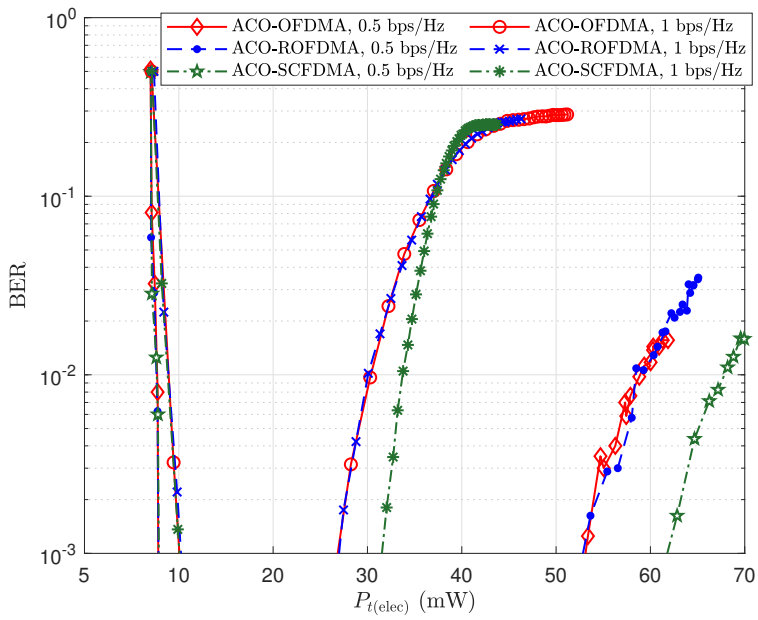


**Figure 5.10:** BER performance comparison of ACO schemes for the spectral efficiency of $\approx 0.5$ bps/Hz (4-QAM, $\mathscr{M} = 4$) and $\approx 1$ bps/Hz (16-QAM, $\mathscr{M} = 4$) with respect to different average electrical transmit power $P_{t(\text{elec})}$, for a fixed $E_{b(\text{elec})}/N_0 = 15$ dB. The patients are placed at a distance $d = 3$ m, where the CN is pointed straight towards the ceiling.

the Rx SNR. The important observation is the difference between MAI and NMAI cases as one would expect no performance degradation when considering multiple users. This is, in fact, due to signal clipping, which affects the orthogonality between users' signals. The degradation is more noticeable for increased $d$ due to the well-known near-far problem.

To clarify this, consider the case of two users with 4-QAM modulation with rectangular pulse shaping on the TD signal at the Tx. After applying ACO-ROFDMA, the spectra of the two users' signals should normally be in the form of two orthogonal sincs, as illustrated in Fig. 5.12a. However, when signal clipping is applied at the Tx, this orthogonality is lost due to the *spectral regrowth* in the adjacent subcarriers, see Fig. 5.12b. As a result, signal reception is effectively affected by MAI, which is more pronounced at relatively high transmit powers, for larger constellation sizes, and with increasing $d$, as can be seen from Fig. 5.11.

For the sake of completeness, consider now the more realistic case of random Tx orientations. (So far, we have considered that all Txs are pointing toward the ceiling in order to avoid costly simulations and to focus on the performance study of the MA schemes.) For this, the $\theta_{tx}$ of the CNs in Fig. 2.6 are generated randomly according to a zero-mean Gaussian distribution, while being limited to the interval $(-60°, 60°)$. Nevertheless, still only the LOS contribution is taken into account, which is justified by the considered large room dimensions, and hence, the rather negligible contribution of non-LOS links. Based on $10^5$ random orientations for all users, $P_{\text{out}}$ results as a function of $d$ are shown in Fig. 5.13 for the cases of MAI and NMAI, considering $\text{BER}_{\text{th}} = 10^{-3}$. $P_{t(\text{elec})}$ is set to 23 mW, corresponding to a low BER, based on the results of Fig. 5.11. For the case of 4-QAM with NMAI, $P_{\text{out}}$ is less than $10^{-3}$ and the corresponding plot is not shown. As expected, $P_{\text{out}}$ increases as the user moves from the center of the cell to the edge due to the higher probability of losing the LOS link. Given that the required $P_{\text{out}}$ for WBAN application is about $10^{-2}$ [215], this is achieved for $d \lesssim 1.5$ m and $d \lesssim 1.4$ m for 4-QAM and 16-QAM cases, respectively. In practice, given the large dimensions of the emergency waiting room, multiple APs should be employed in order to increase the link robustness [215].

## 5.6 Complexity Analysis

To evaluate the computational complexity of the considered signaling schemes, we focus on the complexity of realizing the $\mathcal{N}$-point IFFT/FFT for a number $\mathcal{N}$ of mapped subcarriers, as well as the extra $\mathcal{M}$-point FFT/IFFT used in O-SCFDMA.

The computational complexity of IFFT/FFT is determined by arithmetic operations, i.e., real additions and multiplications, called floating-point operations (FLOPs) [227]. Considering $\mathcal{N}$-point FFT/IFFT ($\mathcal{N}$ is the power of a radix), the use of Cooley-Tukey method in developing a higher-order radix FFT/IFFT algorithm is rather efficient in terms of the number of FLOPs [228]. Further, the development of split-radix algorithms, e.g., the radix-2/4 and radix-2/8, achieves a lower FLOP count [227, 229]. Without loss of generality, we consider a radix-2 algorithm, for the sake of simplicity, where an $\mathcal{N}$-point FFT/IFFT requires approximately $5\mathcal{N}\log_2(\mathcal{N})$ arithmetic

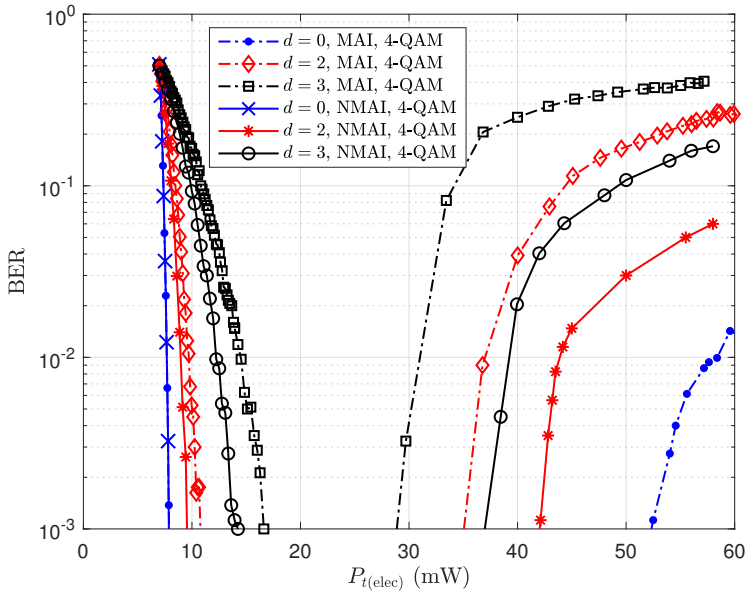


**(a)** $\Gamma_{\text{ACO}} \approx 0.5$ bps/Hz, (4-QAM, $\mathscr{M} = 4$)

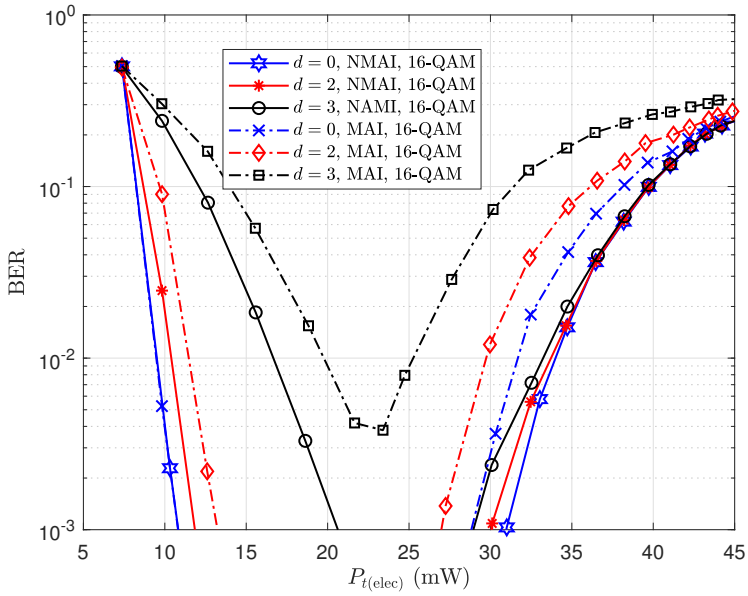


**(b)** $\Gamma_{\text{ACO}} \approx 1$ bps/Hz (16-QAM, $\mathscr{M} = 4$)

**Figure 5.11:** BER versus the average electrical transmit power $P_{t(\text{elec})}$ for different distance $d$ of the desired user from the center of the cell: (a) considering $\Gamma_{\text{ACO}} \approx 0.5$ bps/Hz, (4-QAM, $\mathscr{M} = 4$) (b) $\Gamma_{\text{ACO}} \approx 1$ bps/Hz (16-QAM, $\mathscr{M} = 4$). MAI is the case where the fifteen other patients are positioned at the cell center. NMAI refers to the no-MAI.

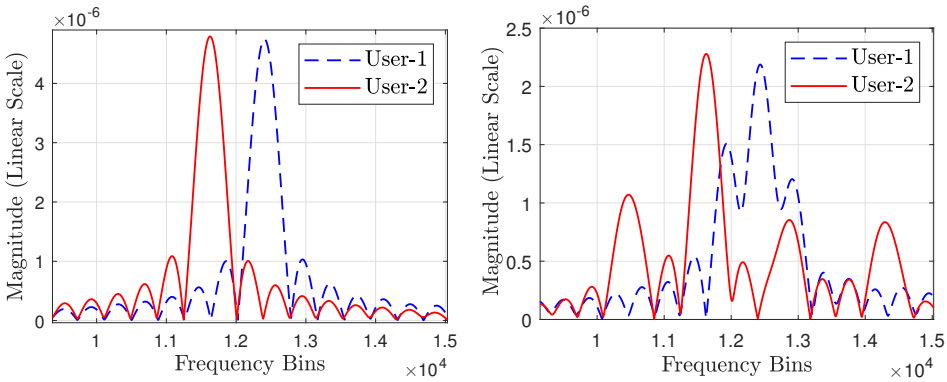


**(a)** Before upper clipping **(b)** After upper clipping

**Figure 5.12:** Spectral magnitude of ACO-ROFDMA signals for the case of two users: (a) Without signal clipping, (b) With the effect of clipping noise.

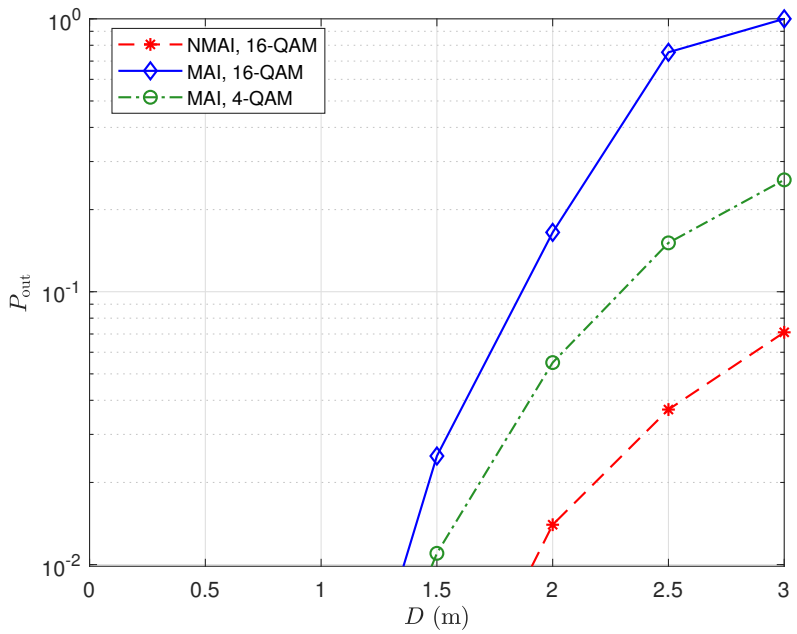


**Figure 5.13:** $P_{\text{out}}$ performance of ACO-ROFDMA due to random Tx orientation for different distance $d$ of the desired user and $\Gamma_{\text{ACO}} \approx 1$ bps/Hz (16-QAM, $\mathscr{M} = 4$).

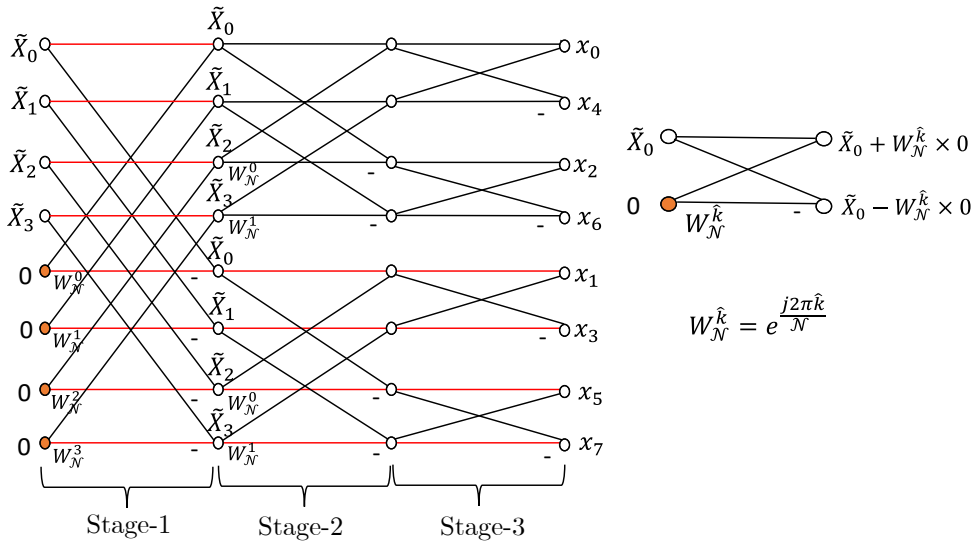


**Figure 5.14:** Illustration of a radix-2 IFFT algorithm for a length $\mathcal{N}$=8, considering the DCO-ROFDMA scheme. $W_{\mathcal{N}}^{\hat{k}}$ is the so-called "twiddle factor" [222].

**Table 5.2:** Computational complexity of different MA schemes.

| MA Scheme | Tx | Rx |
|---|---|---|
| DCO-OFDMA | $5\mathcal{N}\log_2(\mathcal{N})$ | $5\mathcal{N}\log_2(\mathcal{N})$ |
| DCO-SCFDMA | $5\mathcal{M}\log_2(\mathcal{M})+$ $5\mathcal{N}\log_2(\mathcal{N})$ | $5\mathcal{N}\log_2(\mathcal{N})+$ $5\mathcal{M}\log_2(\mathcal{M})$ |
| DCO-ROFDMA | $5\frac{\mathcal{N}}{2}\log_2(\frac{\mathcal{N}}{2})$ | $5\mathcal{N}\log_2(\mathcal{N})$ |

operations [228].

At the Tx, however, for the O-ROFDMA scheme, the FLOP count is reduced by a factor of 2 due to applying padded zeros in the last $\mathcal{N}$ subcarriers. Figure 5.14 illustrates an example of radix-2 IFFT algorithm for the DCO-ROFDMA, considering $\mathcal{N} = 8$. At Stage-1, given a zero in one of the symbols in a butterfly of length 2, no arithmetic operation is required, and the outputs follow the input symbols. Therefore, the first half of symbols are in fact identical copies of the second-half symbols, see Stage-2 in Fig. 5.14. As a result, no arithmetic operation is required for half of the symbols (shown in red color), thus, reducing the computational complexity by a factor of 2. The computational complexity of the considered DCO schemes at the Tx and Rx is given in Table 5.2. Remember that ACO schemes require twice more subcarriers compared to DCO schemes.

Figure 5.15 shows the complexity analysis in terms of number of arithmetic operations required in different ACO and DCO schemes. In order to make a fair comparison between the schemes, we consider the same data-rate $R_b$. As expected, the required number of arithmetic operations increases with increased number of data-carrying symbols $\mathcal{M}$. O-ROFDMA and O-SCFDMA have, respectively, the lowest and highest complexity. Moreover, note that the number

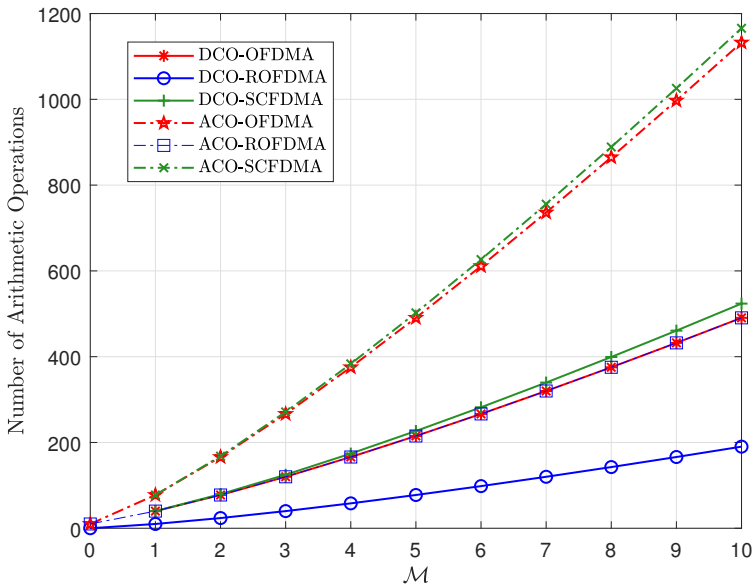


**Figure 5.15:** Complexity analysis of different schemes in terms of required number of arithmetic operations at the Tx versus the number of data-carrying symbols $\mathcal{M}$; $\mathcal{N} = \mathcal{M}\mathcal{L}$ with $\mathcal{L} = 16$.

of arithmetic operations required by ACO-ROFDMA is equal to that for DCO-OFDMA. In fact, the computational complexity of O-ROFDMA is half of that for O-OFDMA.

## 5.7 Chapter Summary

We proposed a HS-free O-ROFDMA scheme which transmits only the real part of the time-domain signal for the uplink extra-WBANs in an emergency waiting room scenario. We investigated the proposed scheme in terms of energy efficiency and computational complexity. More specifically, taking into account the parameters of realistic opto-electronic components, we studied the BER performance of DCO-ROFDMA and ACO-ROFDMA, compared with O-OFDMA and O-SCFDMA counterparts. In particular, we demonstrated the effect of induced MAI due to signal clipping, resulting in a loss of orthogonality between the signals of different users. Focusing then on ACO-ROFDMA as a more appropriate scheme due to its better energy efficiency (despite the requirement of a larger BW), we investigated the impact of MAI under fixed and randomly oriented Txs. We further showed that, thanks to the reduced computational complexity of O-ROFDMA, compared with O-OFDMA, a significant reduction in the Tx (CN) energy consumption can be achieved for medical WBANs.

# Chapter 6

# Experimental Implementation of O-CDMA for Medical Extra-WBANs

**Contents**


**6.1 Introduction** . . . . . **95**
**6.2 System Description** . . . . . **96**
6.2.1 General Assumptions . . . . . 96
6.2.2 General Principles of OOK O-CDMA . . . . . 96
6.2.3 OOK O-CDMA Rx Structure . . . . . 97
6.2.4 Digital Design Concept on Tx/Rx Synchronization . . . . . 98
6.2.4.1 Tx . . . . . 99
6.2.4.2 Rx . . . . . 99
**6.3 Implemetation** . . . . . **99**
6.3.1 Overall Architecture of O-CDMA System . . . . . 99
6.3.2 AFE Design . . . . . 100
6.3.3 CN Digital HW Design . . . . . 100
6.3.4 AP Digital HW Design . . . . . 101
**6.4 Experimental Results** . . . . . **102**
6.4.1 Validation of Digital Design . . . . . 103
6.4.2 Validation of O-CDMA System . . . . . 103
**6.5 Chapter Summary** . . . . . **106**


## 6.1 Introduction

In Chapters 4 and 5, we proposed O-CDMA and O-ROFDMA schemes for the hospital ward and emergency waiting room scenarios, respectively, and evaluated their performances for medical extra-WBANs. In this chapter, we take into account the proposed O-CDMA scheme for hospital ward scenario and develop a PoC for the uplink. We investigate the implementation of an O-CDMA system for medical extra-WBANs based on IR signals. First, we compare different possible O-CDMA Rx architecture to select the most suitable one in our application, given the requirements

of low implementation complexity, and the constraints imposed by near-far problem and the MAI effect. Then, we implement the selected O-CDMA Rx structure on an FPGA and propose an AFE for the transmission and reception of the optical signals. Finally, we evaluate the performance of the implemented system in managing the MAI in terms of BER and frame-error-rate (FER).

The remainder of the chapter is organized as follows. In Section 6.2 we describe O-CDMA based systems, including system architecture, different O-CDMA Rx structure, and digital design concepts. Meanwhile, we demonstrate the advantages of the correlator with a hard-limiter (CHL) Rx structure in terms of implementation complexity and MAI resistance. Next, Section 6.3 presents the implementation details of the AFEs and FPGA prototypes. We also present the computational complexity of the digital hardwares (HWs) in terms of number of logic resources required to implement. Experimental verification and results are presented in Section 6.4. At first, we validate our digital prototypes by transferring signals over wired links, and then analyze the system's performance through the use of optical wireless links in terms of BER and FER. Lastly, the main conclusions of this chapter are drawn in Section 6.5.

## 6.2 System Description

In this section, we define the configurations, e.g., number of users, data-rate, and describe the principle of considered O-CDMA system and its design concepts for the experimental implementation.

### 6.2.1 General Assumptions

We consider the case of four patients in a hospital ward scenario as in chapter 4, sending their health monitoring data via their respective CN to a single AP placed in the center of the ceiling. Each CN, placed on the patient's shoulder to minimize the probability of LOS blocking, transmits its OOC-coded data asynchronously to the AP. In other words, transmission takes place without any synchronization between different CNs.

We assume that the data-rate requirement of each CN is less than 100 Kbps. Given this relatively low data-rate and for the sake of implementation simplicity, we use the simple OOK modulation. Also, we assume that there is always a LOS link between the Tx and the Rx, and hence, neglect the effect of multiple reflections.

### 6.2.2 General Principles of OOK O-CDMA

As we have described in Chapter 3, in O-CDMA signaling scheme, at the Tx side, each bit of an user is at first multiplied by an assigned OOC and then transmitted through the optical channel. To recover the received data of a specific user, the received signals at the PD are at first correlated with the corresponding assigned OOC. Unlike BPPM O-CDMA, the output of each correlator is then compared with a predefined threshold $C_{\mathrm{Th}}$, as illustrated in Fig 6.1. The resulting signal is

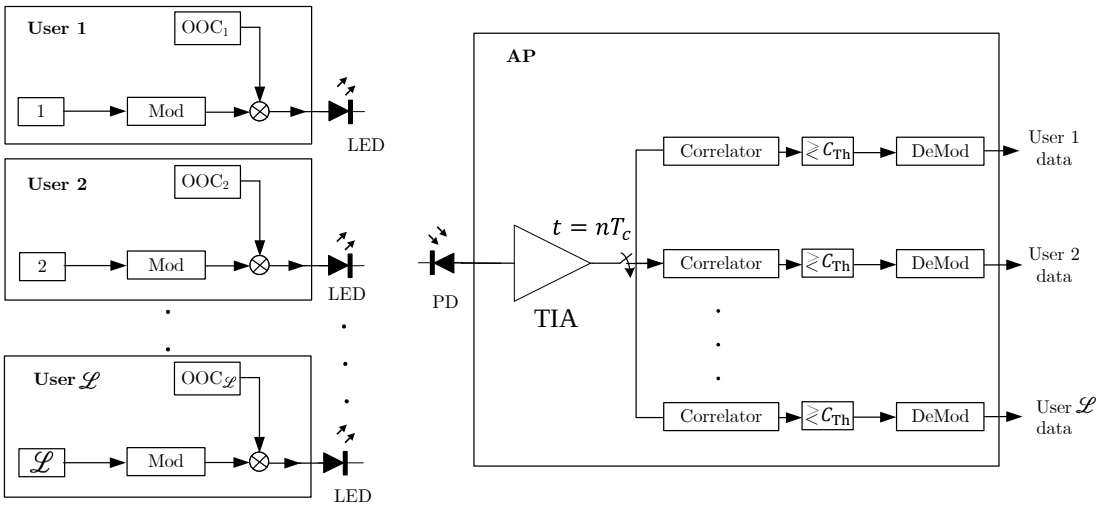


**Figure 6.1:** Block diagram of the OOK O-CDMA based extra-WBAN system; Blocks Mod and DeMod stand for modulator and demodulator. Signal sampling at the TIA output is done at sampling period of $T_c$.

then demodulated to recover the transmitted bits of each user.

In an OOK O-CDMA system with OOC codes, error-free data recovery is possible despite MAI, if $C_{\text{Th}}$ satisfies the following condition [185, 197]:

$$C_{\text{Th}} > \mathscr{L} - 1. \tag{6.1}$$

### 6.2.3 OOK O-CDMA Rx Structure

O-CDMA's performance highly depends on the type of Rx structure used to detect and retrieve data. The three most viable Rx structures for OWCs are correlator, chip-level detector (CLD), and CHL [159].

A correlator or correlation Rx is the simplest Rx structure, see Fig. 6.2a. It consists of a low pass filter and an ADC with a sampling rate at least equal to the chip time. The sampled chips are correlated with the desired user's OOC code, and the output is then compared with an optimal threshold $C_{\text{Th}}$ to detect a bit '0' or '1'. Correlation Rx suffers from the MAI and the near-far problem [159].

The CLD is based on the power of each chip collected by the PD, which is compared to an optimal threshold [230]. It also consists of a filter and an ADC as shown in Fig. 6.2b. Each arm in the figure is used to detect one pulsed (i.e., ON ) chip. Finally, all the values from each arm are added and compared with the weight $K$ to detect the transmit bits. The performance of the CLD is better than that of the correlation Rx [230]. However, it also suffers from near-far problem [230].

In a CHL Rx, a HL is added before the correlator [159], which clips the received signals at a defined level of threshold voltage, and hence converts the signals into binary sequences. Sampling takes place right after the HL with a locally generated clock with frequency at least equal to the

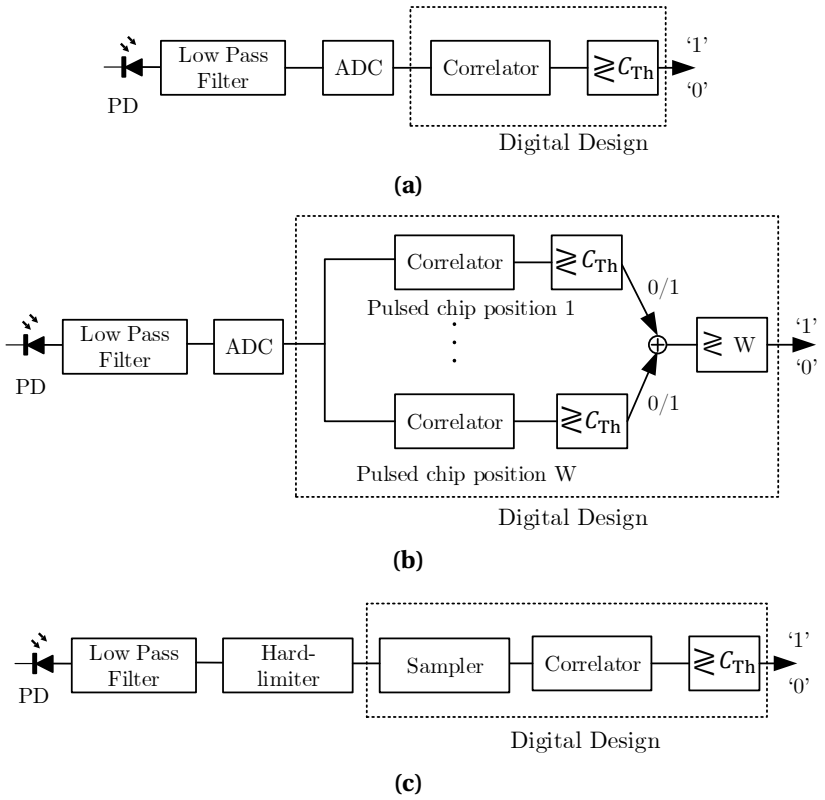


**Figure 6.2:** Different types of Rx structures (a) Correlation Rx: Based on a simple correlator, (b) CLD: The correlation is done based on the received power of each chip, (c) CHL: An HL is added before a simple correlator.

chip rate, see Fig. 6.2c. Therefore, the sampler of a CHL Rx does not require an ADC and can be directly implemented on an FPGA, which significantly reduces its implementation complexity. The main interest of CHL is that it minimizes the MAI effect by restricting the voltage at the same level for all users [201, 231]. Furthermore, the near-far problem is reduced because the defined threshold voltage ensures reception of balanced signals from near and far users. Here, due to its lower implementation complexity and its resilience to MAI and the near-far problem, we consider to use CHL.

### 6.2.4 Digital Design Concept on Tx/Rx Synchronization

As stated in Section 6.2, CNs transmit their OOC-coded data to the AP without any synchronization between them. However, at the AP side, it is crucial to have bit-level synchronization between the corresponding Tx-Rx pairs in order to recover the data of each user properly. This bit-level synchronization relies on mechanisms implemented on both the Tx and the Rx sides as explained in the following.

**(a)** CN

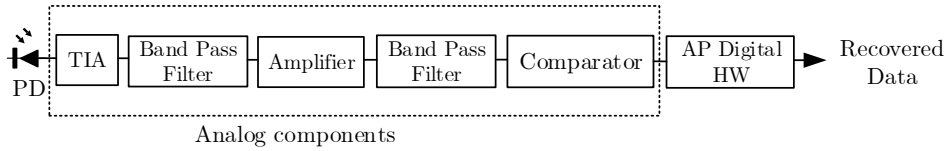


**(b)** AP

**Figure 6.3:** Overall architectures of (a) a CN (Tx) and (b) the AP (Rx) with a focus on the main AFE blocks.

#### 6.2.4.1 Tx

On the Tx side, training patterns are added before transmitting OOC-coded information bits, enabling the Rx to synchronize its code with the corresponding Tx, provided that the Rx has full knowledge of the training pattern sent. The length of the training pattern depends on the type of synchronization algorithm used by the Rx [159].

#### 6.2.4.2 Rx

The synchronization process in an O-CDMA Rx is realized by an acquisition and tracking (AT) circuit, as in RF-based CDMA Rxs [199, 232]. Initial phase synchronization is done at the acquisition stage with a precision better than half of the chip duration $T_c$. Three kinds of acquisition algorithms are proposed for use in OWC, namely simple serial search, multiple shift, and matched filter [159]. The tracking circuit is the second step of the synchronization process. It is used for fine tuning, based on the generation of half-chip early and late replicas of the data. Correlation is then done with each replica and compared with a threshold $C_{\text{Th}}$ to ensure synchronization.

In practice, it is shown that the matched filter algorithm is preferable to the other approaches as it requires a smaller number of training patterns and a shorter mean acquisition time [159]. Thus, we consider this solution in our design.

## 6.3 Implemetation

### 6.3.1 Overall Architecture of O-CDMA System

As explained in Section 6.2.1, our O-CDMA based extra-WBAN system consists of four patients, each with a CN attached on the shoulder, and an AP at the center of the room ceiling. The architectures of a CN and the AP are shown in Figs. 6.3(a) and 6.3(b), respectively. Both the CN and AP are composed of two main parts: the digital HW for generation or recovery of the O-CDMA data stream, and the AFE for transmission or reception of the optical signals. In the subsequent subsections, we discuss the implementation details of the AFE and the digital HWs.

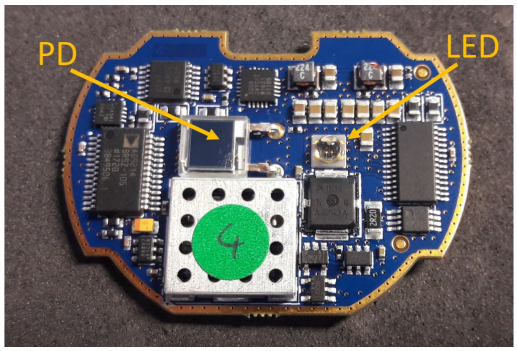


**Figure 6.4:** The off-the-shelf AFE board for IR optical transmission and reception.

### 6.3.2 AFE Design

On the CN side, the role of the AFE is to transmit the OOC-coded data stream generated by the digital HW circuitry through the use of a LED. Since this data stream is a binary sequence, we use a simple LED driver based on a MOSFET switch, see Fig. 6.3(a).

On the AP side, as represented in Fig. 6.3(b), the AFE consists of a PD followed by a TIA to convert the received photo-current into a voltage. The resulting signal is then passed through a first band-pass filter to filter out noises generated by the ambient light and the TIA (i.e., the thermal noise), followed by a voltage amplifier and a second band-pass filter to center the signal around 0 V. Finally, we employ a comparator as a zero-crossing detector, rather than a conventional HL, in order to boost the positive part of the signal to a fixed level (here, to 3.2 V) while setting the negative part of the signal to 0 V. This way, the AFE output signal meets the input/output standard LVCMOS 3.2 V of our FPGA board.

In practice, both the transmission and reception AFEs are implemented on a single board, as represented on Fig. 6.4. The LED operates at 940 nm with a semi-angle at half power of 60°. The Tx 3 dB modulation BW is 9 MHz. On the Rx side, the 3 dB BW is 15 MHz and the overall Rx gain considering TIA and amplifier is 62 dB. The PD has a 26.4 mm$^2$ active surface, a 0.6 A/W sensitivity at 940 nm and a full angle at half-sensitivity of 120°.

### 6.3.3 CN Digital HW Design

In the CN digital HW, the serial data stream is encoded with the corresponding OOC code. Here, without loss of generality, we consider $L = 8$ data bits per transmitted packet in addition to $L_p = 3$ training bits (which are set to one) as preamble for synchronization purpose. The corresponding block diagram is shown in Fig. 6.5.

First, the serial data stream is passed through a serial-to-parallel shift register ("SIPO" block in Fig. 6.5) in order to form the payload of the O-CDMA data frame. The SIPO block is followed by a dual clock first-input first-output (FIFO) memory block. Note that in digital system design, FIFOs are used to transfer data between two different clock domains [233]. Here, the FIFO is used to transfer data from the local clock domain (i.e., clock for sensors data) to the chip clock domain.

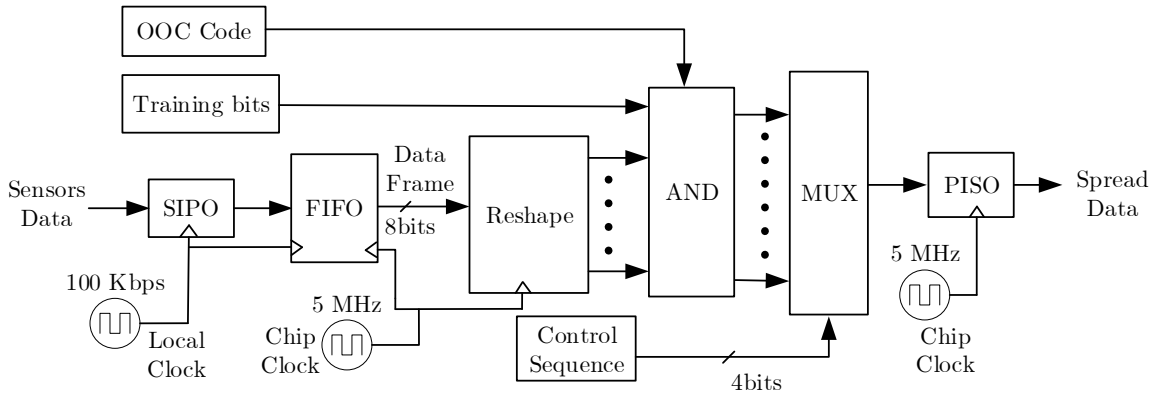


**Figure 6.5:** Conceptual block diagram of CN digital HW based on O-CDMA for extra-WBAN links. SIPO, PISO, and MUX stand for serial-in parallel-out, parallel-in serial-out shift register, and multiplexer, respectively.

Each data bit then has to be multiplied by the OOC. By considering a maximum of four users, we deduce from Equations (4.3) and (4.4) that the OOC length has to be at least $F = 49$. Since the input data rate is assumed to be 100 Kbps, see Section 6.2.1, the chip clock rate at which the OOC-coded data have to be sent is set to 5 MHz. In practice, the multiplication with the SC is done by an AND logic gate. Therefore, each bit of the payload is first duplicated $F$ times by the "Reshape" block and then passed through an AND gate to apply the OOC. Note that the training bits are also OOC-coded to avoid MAI from other users (see Fig. 6.5). These $L_p$ sequences are added to the beginning of the frame by the aid of a multiplexer (the "MUX" block), controlled by the "Control Sequence" block. Finally, a parallel-to-serial shift register ("PISO" block in Fig. 6.5) converts the OOC-coded data frames to serial spread data, which are then transferred to the Tx AFE.

### 6.3.4 AP Digital HW Design

The architecture of the AP digital HW for detecting the data of a given user is represented in Fig. 6.6. The same architecture is used for every user. As it can be seen, the data are first sampled ("Sampler" block in Fig. 6.6). The sampling process is done in the digital domain with a locally generated sampling clock $CK(t)$ of frequency 5 MHz. From a digital design point of view, synchronization failure is very common when sampling an asynchronous input with respect to a clock, that is when the asynchronous input (i.e., spread data) changes during the set up time of the clock [234]. To deal with this problem, we used three cascaded flip-flops (FFs) inside the sampler.

After sampling, at first, acquisition is performed in the "AV" block. This latter searches the training patterns by matched filter algorithm, as described in [159], and obtains initial time reference of the received spread data with a precision better than half of the chip duration $T_c$. Then the received spread data is sent to the verification stage in the "AV" block to detect false alarms (due to MAI and/or noise) by comparing with a predefined threshold. If a false alarm is detected, then the "AV" block starts performing acquisition again. Otherwise, the *Acquisition Performed* flag is set to

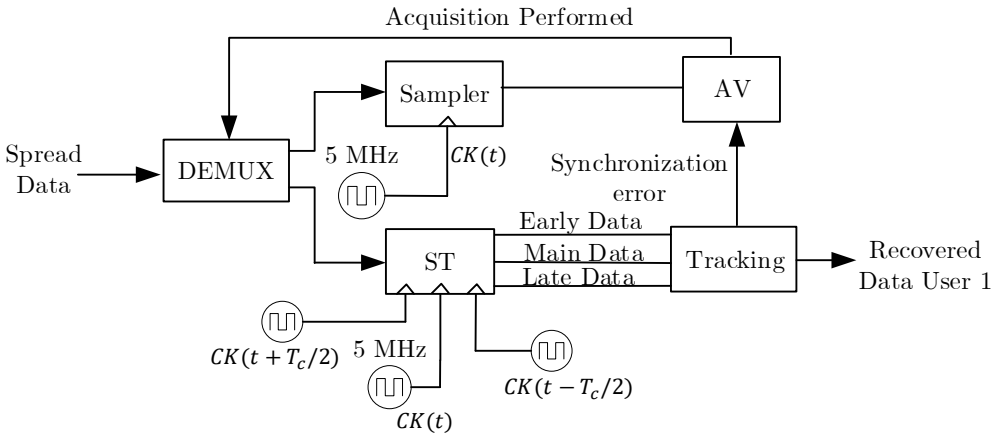


**Figure 6.6:** Conceptual block diagram of AP digital HW based on O-CDMA corresponding to one user. Here, AV stands for acquisition and verification. The "ST" block generates early and late replicas of the spread data.

high (see Fig. 6.6). This latter, in fact, activates acquisition or tracking process of the de-multiplexer ("DEMUX" block).

Afterwards, the tracking circuit starts more precise synchronization using the so-called early-late technique. To do this, the "ST" block generates early and late versions of the data, sampled by the shifted clocks $CK(t-T_c/2)$ and $CK(t+T_c/2)$, respectively. These replicas of the data are correlated with the OOC code, and the outputs of the correlators are then compared with the main data (i.e., the data that is sampled with the clock $CK(t)$) to obtain tracked spreading data. Meanwhile, if the outputs of the correlators are less than the threshold $C_{\text{Th}}$, a synchronization error signal is sent to the "AV" block to start a new acquisition.

## 6.4 Experimental Results

To implement our O-CDMA digital HW, we consider the case of two CNs (Txs), transmitting their data simultaneously to a single AP (Rx). We have assigned the codewords $\{0,1,4,14\}$ and $\{0,2,7,26\}$ to the CNs, where each number represents the position of '1' in the sequence of the OOC $(49,4,1,1)$ code. We then implemented the full digital HWs described in Section 6.3, on Xilinx® Zynq series 7z020 FPGAs. We have summarized the design synthesis results from the Xilinx® Vivado design suite in Table 6.1. As expected, the Tx remains quite simple to implement, with an estimated on-chip power consumption of 0.752 W. Note that when implemented on an ASIC (Application-Specific Integrated Circuit), the power consumption can be considerably reduced [235].

We have carried out the experimental validation of the proposed O-CDMA system in two steps. First, we verified that the digital HW algorithms were functional, which is described in Subsection IV-A. Then, we experimentally analyzed the performance of the whole system, as explained in Subsection IV-B.

**Table 6.1:** Logic resources required at CN. LUT and BUFGCTRL stand for look-up table and global clock buffer.

| Logic | Number of Resources |
|---|---|
| LUTs | 95 |
| LUTs as Memory | 22 |
| LUTs as Logic | 73 |
| FFs | 255 |
| BUFGCTRL | 2 |

### 6.4.1 Validation of Digital Design

A design implemented on an FPGA is usually validated functionally by performing a post-implementation simulation on the EDA (Electronic Design Automation) simulator. This, however, does not guarantee the behavior of the design in the real HW. Therefore, a built-in IP (intellectual property) core called integrated logic analyzer (ILA) is used to analyze and debug the system in real time after HW implementation.

Here, both Tx digital HWs are implemented on the same FPGA board, and the Rx digital HW is implemented on another FPGA board. In order to transmit OOC-coded data streams from both Txs with a single FPGA, we simply generated the two streams independently and then added them with an OR gate. This way, on the CN side, the FPGA had a single data output containing the signals from both users. This output was connected with a wire to the input of the second FPGA embedding the AP digital HW. Consequently, the transmission channel between the CN and the AP could be considered as very low noise and thus not being the source of performance degradation. This allowed us to evaluate the performance of the digital HW algorithms.

The real-time timing diagrams in Fig. 6.7 are captured from FPGA's ILA through a JTAG cable. We transferred known pattern of frames from Tx1 (i.e., $33_{16}$ and $cc_{16}$) and Tx2 (i.e., $0f_{16}$ and $3c_{16}$) repeatedly to compare the recovered data after correlation. In Fig. 6.7(a), the transmitted data sequences from Tx1 and Tx2 are denoted by $sp_out_tx1$ and $sp_out_tx2$, respectively. These spread data generated from Txs are passed through the OR gate and transferred by the port $sp_out_comb$.

The data received by the AP, denoted by $spc_in$, are sampled by a locally generated clock, as seen in Fig. 6.7(b). The frames recovered by the Rx are defined as $dout_rec1$ and $dout_rec2$, where frames are valid if and only if $dout_valid_1$ and $dout_valid_2$ are set to high level for Tx1 and Tx2, respectively. We observed that under the considered "ideal" conditions (i.e., without any noise) the transmitted data bits were recovered from both users without any MAI error.

### 6.4.2 Validation of O-CDMA System

In order to validate the whole O-CDMA system, we replaced the OR gate and wired channel by the AFEs. Figure 6.8 shows the experimental setup, where the main parameters are given in Table 6.2.

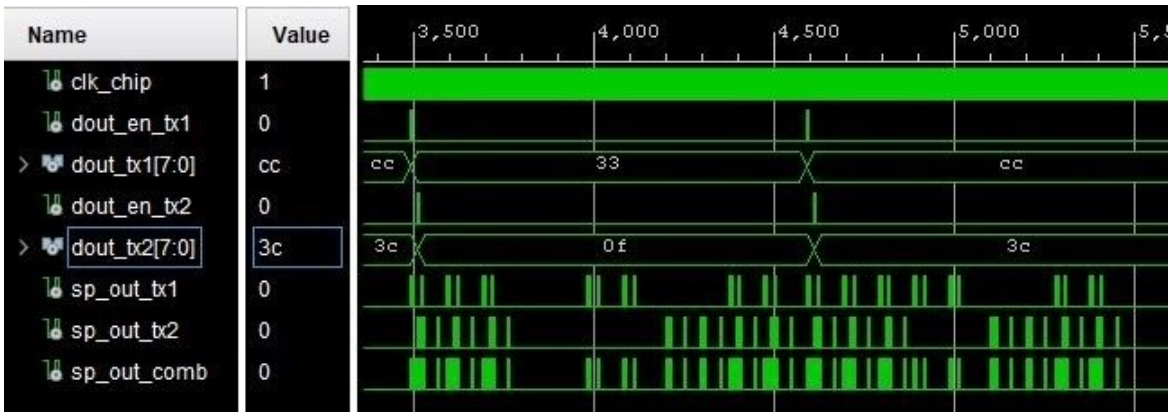


**(a)** Txs

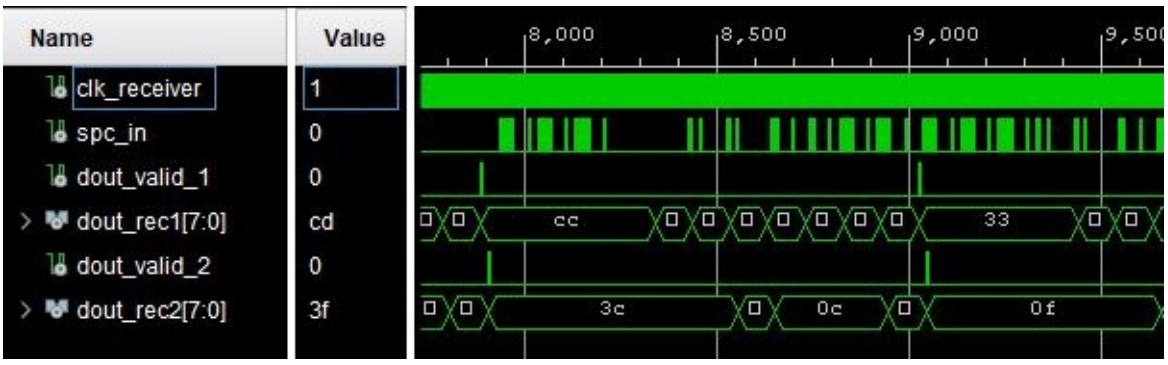


**(b)** Rx

**Figure 6.7:** Txs and Rx timing diagrams captured through ILA for the case of wired transmission link: (a) Txs send spread data through an OR logic by the port $sp_out_comb$, (b) transmitted data of both Txs are recovered by the Rx.

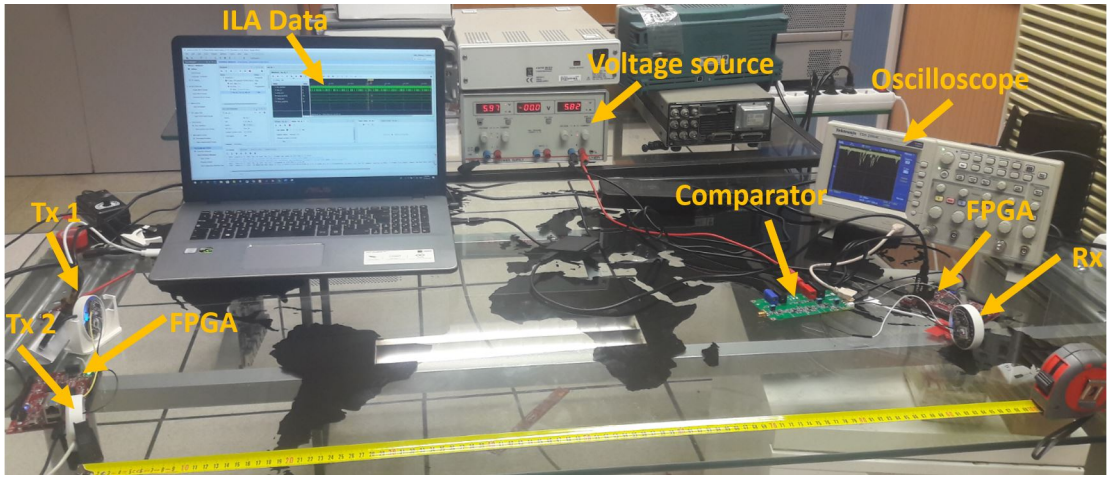


**Figure 6.8:** Experimental setup. Here, Txs are placed at a distance of 1 m from the Rx.

Both Tx AFEs are placed at a distance of 20 cm from each other and driven by the same FPGA. The measured average transmit power of the IR LED is about 16 mW, that is well bellow the eye-safety requirement [52]. Note that, we have $K = 4$ ON pulse for the SC length $L = 49$.

**Table 6.2:** Parameters used in the experiment.

| Parameter | Value |
|---|---|
| OOC code | (49,4,1,1) |
| Number of users | 2 |
| Threshold | 4 |
| CN1 OOC code | {0,1,4,14} |
| CN2 OOC code | {0,2,7,26} |
| Tx 3 dB modulation BW | 9 MHz, |
| Rx 3 dB reception BW | 15 MHz, |
| O-CDMA required BW | 5 MHz |
| Rx maximum gain | 62 dB |
| PD active area | 26.4 $mm^2$ |
| PD responsivity | 0.6 A/W |
| Rx full angle at half-sensitivity | 120° |
| LED wavelength | 940 nm |
| LED average transmit power | 16 mW |
| LED semiangle at half power | 60° |

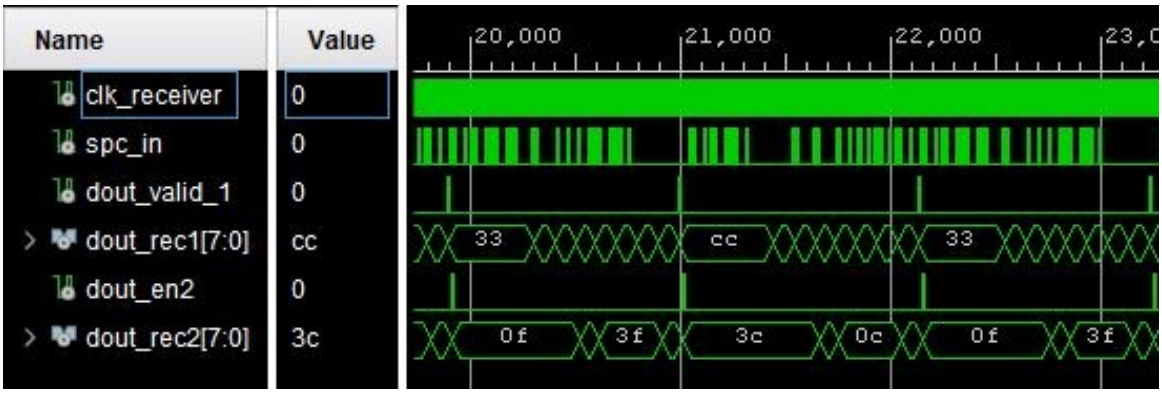


**Figure 6.9:** Recovered data from the two Txs which are positioned at a distance of 20 cm from the Rx. The data were read through the built-in ILA of FPGA via a JTAG port.

First, we verified the behavior of the O-CDMA system at short distance. Figure 6.9 shows the frames recovered at the Rx when it is placed at a distance of 20 cm from the Txs. As in Fig. 6.7(a), we can see that the data being sent by both Txs are recovered completely. Then, we varied the distance $Z$ between the Txs and the Rx from 20 cm to 1 m and processed the data captured from the ILA with MATLAB® in order to extract the BER and FER with respect to the distance, as shown in Fig. 6.10. We notice that, logically, as the distance $Z$ increases, the BER increases due to decreased received power. Remember from Fig. 6.3(b) that the comparator acts as a zero-crossing detector, which outputs a 3.2 V level if the signal is positive, and 0 V otherwise. Therefore, when the signal is weak and noisy, there might be unexpected zero-crossings leading to an unstable output signal and, eventually, to bit errors.

Moreover, we see from Fig. 6.10 that the performances of the two Txs are not exactly the same.

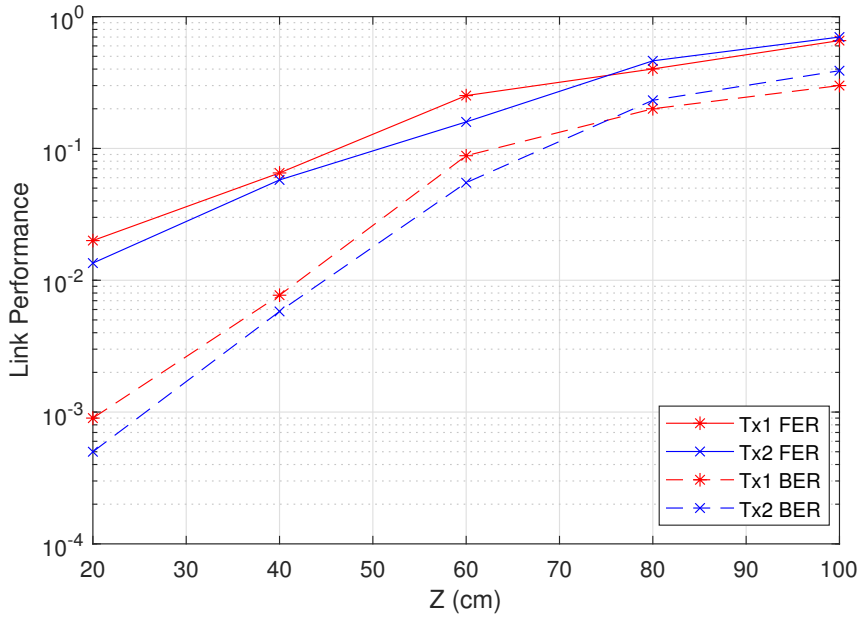


**Figure 6.10:** Measured BER and FER from experiments, where distance $Z$ between the Txs and the Rx was varied from 20 cm to 1 m.

This is because in our set-up Txs were not exactly at the same distance from the Rx and did not have exactly the same angle of emission with respect to the Rx. This could be considered as a slight form of the near-far problem, which is not mitigated here, as expected for a CHL Rx since we use a comparator instead of a true HL. Indeed, the comparator output is sensitive to the received power level.

## 6.5 Chapter Summary

In this chapter, we proposed digital HW architectures for the CN and the AP for the case of extra-WBAN uplinks. The O-CDMA technique was considered to address the multi-user feature of such applications. We also considered AFE design mainly based on CHL while accounting for ease of integration of the AFE part with the digital HW circuitry. Moreover, we implemented the low-complexity digital HW part on the programmable logic. For the case of two users (i.e., two Txs), firstly, we verified the error-free signal reception on a high SNR system (i.e., using a wired link), and then studied the performance of the system with wireless links in terms of BER and FER for different SNR values (i.e., varied link distance). However, the performance of the system can be improved using error-correcting codes.

# Chapter 7

# Conclusions and Perspectives

**Contents**


7.1 Conclusions . . . . . 107
7.2 Perspectives for Future Work . . . . . 108


## 7.1 Conclusions

Real-time health monitoring of patients is crucial to detect any deterioration in the patients' health conditions and to prevent inappropriate treatments. Such e-Health solutions can be enabled by employing wearable health monitoring sensors on the patient body to collect and transmit medical data through the use of WBANs. For data transmission in medical WBANs, OWC is a license-free promising technology that offers features of inherent security and immunity against EMI, compared to the RF counterpart. Within this context, managing multiple users transmitting their medical data simultaneously requires the use of appropriate MA techniques, with the constraints of low power consumption and high link reliability. In particular, mobility of patients and random Tx orientations can impair the optical link performance significantly. In this thesis, we developed and proposed suitable MA techniques for different medical WBAN scenarios and investigated their performance taking into account realistic system parameters.

For this purpose, we first defined the optical link configurations based on IR transmission for medical WBAN scenarios and presented their channel modeling approach in Chapter 2. Then, in order to consider link impairments resulting from mobility, we developed a realistic mobility model that included random Tx orientations during patient movements. Next, in Chapter 3, we proposed an O-CDMA scheme for a typical hospital ward scenario with a relatively small number of patients, due to its advantages of relaxed synchronization requirements and implementation simplicity. On the other hand, to manage a relatively large number of users, we investigated the use of O-OFDMA based schemes.

In Chapter 4, we investigated the performance of the proposed O-CDMA scheme using the developed ORWP mobility model in Chapter 2. We focused on analyzing BER and $P_{\text{out}}$ performances

by changing users' positions in a typical hospital ward scenario, while showing the detrimental impact of random Tx orientations. We showed the MAI effect on the O-CDMA link performance taking into account contributions from both LOS and non-LOS reflections. Lastly, to address the resulting performance degradation, we proposed the use of multiple AP arrangements and demonstrated the performance improvement through simulation results.

In Chapter 5, taking into account the requirement of relatively large number of patients in an emergency waiting room scenario, we proposed a new O-OFDMA based solution called O-ROFDMA. Unlike the conventional O-OFDMA, we did not apply HS constraints to the FD signal, and only real part of the OFDMA TD signal is transmitted. First, we investigated the performance of the scheme taking into account limited DR of the LED compared to the O-OFDMA and O-SCFDMA schemes for both ACO and DCO signaling cases. We showed that O-ROFDMA has nearly the same performance as O-OFDMA in terms of PAPR and BER, although outperformed by O-SCFDMA at the cost of increased computational complexity, in particular, for larger signal constellation size. Then, we studied the performance of the ACO-ROFDMA scheme taking into account random Tx orientations for an emergency waiting room scenario, where we demonstrated the effect of MAI due to clipping noise. Furthermore, we showed that O-ROFDMA offers a reduced computational complexity of factor 2 compared to O-OFDMA.

Lastly, in Chapter 6, we developed FPGA prototypes of the proposed O-CDMA system in Chapter 4 for medical extra-WBANs and tested the performance of the implemented system. This was made possible, thanks to the support from Oledcomm Co. for providing experimental equipment and analog front-ends under the framework of the H2020 ITN Vision project. We first validated the prototypes design by considering an ideal link, and then measured the performances in terms of BER and FER by changing the Txs distance.

## 7.2 Perspectives for Future Work

This thesis was devoted to proposing and developing suitable MA solutions for optical medical WBANs by focusing on the performance investigation of the proposed schemes considering limitations arising from patients' mobility and random Tx orientations. The work presented in this thesis addressed the majority of the goals outlined in Chapter 1. However, several aspects remain to be investigated for future work as described in the following.

We demonstrated the effect of MAI due to the near-far problem in O-CDMA scheme but did not consider any MAI mitigation technique. As a future research direction, it would be interesting to investigate the efficiency of using a HL device prior to the correlator, as suggested in [132], to reduce the MAI effect by limiting the interference level. Studying the practical interest of power control at the Tx to reduce the near-far problem is another interesting direction for future work. Note that, this issue is widely considered in the context of RF CDMA [236] .

As concerns the investigation of the proposed O-ROFDMA scheme in Chapter 5, we considered only the LOS link and did not consider user mobility. Studying the effect of multipath reflections in

more realistic scenarios while taking into account mobility is another interesting direction. On the other hand, uplink synchronization is a critical requirement for OFDMA-based schemes, which is usually done by estimating CSI using training sequences. Further investigation should be carried out by taking into account synchronization errors due to mobility and random Tx orientations, which might affect the system's performance. Moreover, future work can investigate the effectiveness of diversity combining techniques for multiple AP arrangements to increase the network coverage for large indoor spaces, such as an emergency waiting room. Another future research direction would be investigating the low-complexity code-domain NOMA techniques for optical WBANs.

As for experimental studies in Chapter 6, due to limitation of the available optical front-ends, we were not able to test the MAI in depth for the O-CDMA case considering a larger number of users. Moreover, we did not implement the proposed O-ROFDMA scheme in real HWs and investigate the performance in a real-time OWC transmission set-up. Further work should be carried out to test the performance of the MA schemes in real hospital settings.

Concerning extra-WBAN downlink communication, which we did not consider in the thesis, the battery-powered Rx requires a low-complexity MA solution. Recently, a low-complexity Rx based on analog multi-band carrierless amplitude and phase modulation has been proposed for VLC-based IoT connectivity in the downlink in [237]. This work can be further extended as an MA solution for the downlink extra-WBAN network. Moreover, proposing efficient MAC layer solutions addressing the case of optical intra- and extra-WBANs is an interesting research direction.

# Appendix A

# Incident angle on the Reflecting Surface

The incident angle $\upsilon$ on the reflecting surface can be calculated by employing the trigonometry of the rectangular triangles, which depends on the elevation angle $\theta_{tx}$ and azimuth angle $\omega_{tx}$. For this, we define a point $C$ intesecting the normal vector $\boldsymbol{n}'_{\text{Tx}}$, as shown in the Fig. A.1.

Denoting the coordinates of the Tx by $T(x_T, y_T, z_T)$ and reflecting surface element by $E_\iota(x_E, y_E, z_E)$, we have:

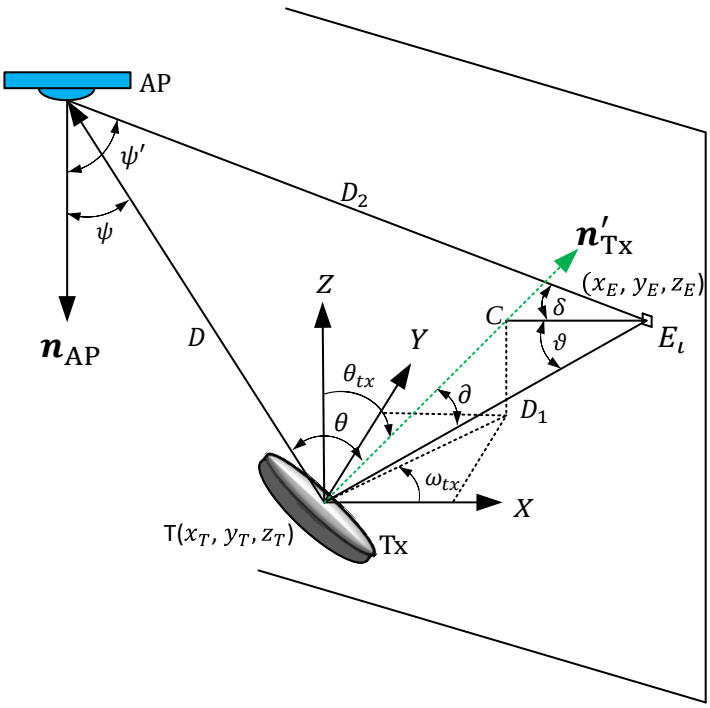


**Figure A.1:** LOS and diffuse link with randomly oriented Tx. The incident angle $\upsilon$ is determined by applying trigonometry of the rectangular coordinates.

$$\cos(\upsilon) = \frac{\left|\overrightarrow{TC}\right|^2 + \left|\overrightarrow{TE_\iota}\right|^2 - \left|\overrightarrow{E_\iota C}\right|^2}{2\left|\overrightarrow{TC}\right|\left|\overrightarrow{TE_\iota}\right|}, \tag{A.1}$$

where

$$\left|\overrightarrow{TC}\right|^2 = \tan^2(\theta_{tx})(z_T - z_E)^2, \tag{A.2}$$

$$\left|\overrightarrow{TE_\iota}\right|^2 = (x_T - x_E)^2 + (y_T - y_E)^2 + (z_T - z_E)^2, \tag{A.3}$$

$$\left|\overrightarrow{E_\iota C}\right|^2 = \left(x_E - x_T + \frac{\cos(\omega_{tx})}{\cot(\theta_{tx})}(z_T - z_E)\right)^2 + \left(y_E - y_T + \frac{\sin(\omega_{tx})}{\cot(\theta_{tx})}(z_T - z_E)\right)^2. \tag{A.4}$$

# Appendix B

# O-CDMA Acquasition and Verfication Block

As described in Chapter 6, we used a matched filter algorithm in order to perform acquisition of the sampled spread data for O-CDMA. The digital design concept of the acquisition and verification, i.e., the "AV" block is presented in Fig. B.1. The serial spread data is fed into a shift-register containing $F$ FFs. Provided that the sampling rate is equal to the chip rate, the FFs outputs corresponding to the position of ON chips are fetched into an adder. The resulting output is compared with the predefined threshold. Finally, if the comparator output is greater than the threshold, an acquisition performed signal is generated after passing through the "verification" block.

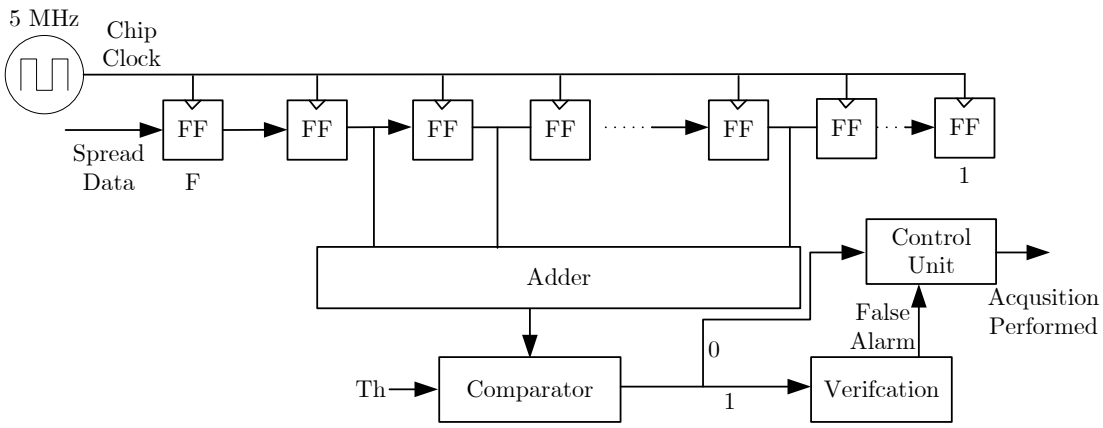


**Figure B.1:** Digital design concept of the "AV" block employing matched-filter algorithm. Here, Th refers to the threshold.

# List of Figures


1.1 The e-Health paradigm (reproduced from [6]). . . . . 11

1.2 Different WBAN application scenarios. . . . . 12

1.3 Communication architecture of a typical WBAN composed of intra-WBAN, extra-WBAN, and beyond-WBAN. . . . . 13

1.4 Illustration of different types of signal interference in medical WBANs. . . . . 16

1.5 Examples of OWC applications in indoor and outdoor scenarios. . . . . 17

2.1 General representation of a typical OWC system. . . . . 25

2.2 Spectral responses of a white LED, IR LEDs with center wavelengths of 830 nm, 870 nm, and 950 nm, and a typical PIN PD, reproduced from [70]. . . . . 26

2.3 Link configurations for indoor optical extra-WBANs: (a) directed LOS, (b) non-LOS, (c) hybrid link. The Tx is placed on the shoulder of the patient. . . . . 30

2.4 Example of bit-symbol mapping in OOK and 8-PPM signaling scheme. . . . . 32

2.5 Illustration of a typical LOS link configuration between a CN and the AP. $x$ and $y$ represent the coordinates of the CN with respect to the room center, i.e., the AP position. . . . . 34

2.6 LOS and diffuse link with randomly oriented Tx. Here, $\theta_{tx}$ denotes the elevation angle, $\omega_{tx}$ is the azimuth angle, and $\boldsymbol{n}_{\text{AP}}$ and $\boldsymbol{n}'_{\text{Tx}}$ stand for the normal vectors corresponding to the AP and Tx, respectively. . . . . 35

2.7 Orientations of a Tx: (a) reference orientation, when the reference coordinate system $XYZ$ and the actual Tx coordinate system $x'y'z'$ are aligned, (b) Pitch rotation, the Tx rotation around the $X$ axis with angle $\beta$, (c) Roll rotation, the Tx rotation around the $Y$ axis with angle $\gamma$, (d) Yaw rotation, the Tx rotation around the $Z$ axis with angle $\alpha$. . . . . 36

2.8 Illustration of RWP mobility model for a node within a confined area. . . . . 38

3.1 Resource allocation by FDMA considering three users in the uplink where each user is assigned a unique frequency band. . . . . 43

3.2 Resource allocation by TDMA in the uplink. Here, three users transmit data at their assigned time slots. . . . . 44

3.3 Resource allocation by CDMA considering three users in the uplink. Each user is assigned a unique SC. . . . . 45

3.4 Resource allocation by OFDMA considering two users in the uplink. Here, $S_1$ and $S_2$ refer to the symbol 1 and symbol 2, respectively. . . . . 46

3.5 Resource allocation by SCFDMA considering two users in the uplink. Here, $S_1$ and $S_2$ refer to the symbol 1 and symbol 2, respectively. . . . . 47

3.6 Resource allocation by a typical power-domain NOMA considering two users in the uplink. At the Rx, SIC is performed to distinguish desired user signal based on the difference in received channel gains. . . . . 48

3.7 Bitstream mapping by SCMA considering six users for the uplink. Each user's bitstreams are mapped to four orthogonal sparse codes from the assigned codebook. . . . . 49

3.8 Typical block diagram of O-CDMA for two users in the uplink. Blocks Mod and DeMod stand for modulator and demodulator, respectively. . . . . 50

3.9 Typical block diagram of O-CDMA signaling based on WH and PN sequences for two users. 51

3.10 Block diagram of the DCO-OFDMA signaling scheme. . . . . 52

3.11 An example of interleaved subcarrier mapping and localized subcarrier mapping for the case of three users, each having three symbols denoted by $S_0$, $S_1$, and $S_2$. . . . . 53

3.12 Block diagram of the DCO-SCFDMA signaling scheme. . . . . 54

4.1 Illustration of a typical hospital ward scenario using an IR based extra-WBAN with multiple patients, each one having a CN (the red bullet on the shoulder). Here, 4 APs are considered, placed on the ceiling. . . . . 59

4.2 Example of frame structure of BPPM O-CDMA signaling. . . . . 60

4.3 Block diagram of the proposed O-CDMA based extra-WBAN system; Blocks Mod and DeMod stand for modulator and demodulator. Signal sampling at the trans-impedance amplifier output is done at sampling period of $T_c$, the chip duration. . . . . 60

4.4 Impact of Tx orientation on the LOS outage for distances $d$ from the room center, $P_{t(\text{opt})}$= 100 mW. Only the LOS path is taken into consideration. . . . . 65

4.5 Impact of Tx orientation on the minimum (min) and maximum (MAX) detectable received power for distances $d$ from the room center. LOS and LOS+1$^{\text{st}}$-order reflections are taken into consideration. . . . . 66

4.6 Trajectory of the displacement of the desired user from $d = 0$ (room center) to $d = 5.7$ m (room corner). . . . . 67

4.7 BER versus the horizontal distance $d$ of the desired user from the AP for different transmit powers. MAI represents the case where the three other users are located at the same position at the room center. NMAI stands for no-MAI. Only the LOS path is taken into consideration. 67

4.8 Outage probability versus the horizontal distance of the desired user from the AP for different transmit powers. MAI represents the case where the three other users are located at the same position at the room center. The three interferers and the desired user are oriented randomly at their positions. Only the LOS path is taken into consideration. . . . . 69

4.9 Outage probability versus the horizontal distance of the desired user from the AP, taking into account LOS and 1st-order reflections. MAI represents the case where the three other users are located at the same position at the room center. The three interferers and the desired user are oriented randomly at their positions. . . . . 70

4.10 Outage probability versus the horizontal distance of the desired user from the AP for different numbers of users $\mathscr{L}$. Interferers are located at the same position at the room center. $P_{t(\text{opt})}$ = 50 mW. The three interferers and the desired user are oriented randomly at their positions. 71

4.11 Outage probability versus the horizontal distance of the desired user from the AP, taking into account LOS and 1st-order reflections. The three interferers are randomly moving and oriented based on the ORWP mobility model inside the room; the desired user is randomly oriented at each position. . . . . 72

4.12 Arrangements of APs on the ceiling for the room size $(8 \times 8 \times 3)$ m$^3$: (a) case of 2 APs, (b) 4 APs. Here, dotted blue line represents the horizontal distance $d$ from the center of the room. . . 72

4.13 Outage probability versus the horizontal distance of the desired user from the center of the room for the 2 and 4 AP configurations, considering LOS+1st-order reflections. Three randomly moving and oriented interferers based on the ORWP mobility model; randomly oriented desired user at each position. . . . . 73

4.14 Outage probability versus the horizontal distance of the desired user from the center of the room for the 2 and 4 AP configurations for the case of NMAI. The desired user is oriented randomly at each position. LOS+1st-order reflections are considered. . . . . 74

4.15 Outage probability versus the transmit power $P_{t(\text{opt})}$ with randomly moving and oriented desired user and interferers for the cases of one, two, and four APs based on the ORWP mobility model. Two cases of LOS and LOS+ 1st-order reflections are considered. . . . . 75

5.1 Illustration of a health monitoring system in an emergency waiting room scenario by using IR extra-WBAN uplink for multiple patients, each one with a CN on the shoulder (the red bullet). A single AP is considered, placed on the ceiling. Here, $d$ is the distance between the patient (i.e., the CN) and the cell center. . . . . 79

5.2 FD aliasing in a recovered signal from the real part of its IFFT output: (a) Real-valued subcarriers in a FD signal, where the total number of subcarriers $N$= 4, (b) The complex conjugate and time-reveresed version of the FD signal, (c) The FFT output signal taking into account only the real part, showing FD aliasing. . . . . 80

5.3 Recovering a FD signal from the real part of its zero-padded IFFT output: (a) Real-valued subcarriers in a FD signal, where the total number of subcarriers $N = 4$, (b) The FD signal is extended to $2N+1$ by adding zero-padded subcarriers, (c) The complex conjugate subcarriers of the zero-padded FD signal are mapped in reverse-order, (d) The FFT output of the signal taking into account only the real part, showing no FD aliasing. The shaded region shows the recovered signal $X_k$. . . . . 81

5.4 Block diagram of the DCO-ROFDMA signaling scheme. . . . . 82

5.5 I-V characteristics of the LED, HDN1102W-TR [216]. . . . . 83

5.6 CCDF plots of PAPR for DCO-OFDMA, DCO-SCFDMA and DCO-ROFDMA schemes, considering different numbers of data-carrying symbols $\mathscr{M}$ per user and the 16-QAM constellation. 86

5.7 BER performance comparison of different DCO schemes, considering the spectral efficiency of ≈ 1 bps/Hz (4-QAM), 2 bps/Hz (16-QAM) and 3 bps/Hz (64-QAM) for the average electrical transmit power $P_{t(\text{elec})} = 48$ mW. The patients are considered to be placed at a distance of $d = 3$ m from the AP (at the cell edge). . . . . 87

5.8 BER performance comparison of different ACO schemes, considering the spectral efficiency of ≈ 0.5 bps/Hz (4-QAM), 1 bps/Hz (16-QAM) and 1.5 bps/Hz (64-QAM) for the average electrical transmit power $P_{t(\text{elec})} = 23$ mW. The patients are considered to be placed at a distance $d = 3$ m from the AP. . . . . 87

5.9 BER performance comparison between ACO and DCO schemes with respect to different average electrical transmit power $P_{t(\text{elec})}$ for a fixed $E_{b(\text{elec})}/N_0 = 15$ dB and the spectral efficiency of ≈ 1 bps/Hz. Here, 16-QAM and 4-QAM constellation is considered with $\mathscr{M} = 4$ for ACO and DCO schemes, respectively. The patients are placed at the same position at a distance $d = 3$ m from the AP. . . . . 89

5.10 BER performance comparison of ACO schemes for the spectral efficiency of ≈ 0.5 bps/Hz (4-QAM, $\mathscr{M} = 4$) and ≈ 1 bps/Hz (16-QAM, $\mathscr{M} = 4$) with respect to different average electrical transmit power $P_{t(\text{elec})}$, for a fixed $E_{b(\text{elec})}/N_0 = 15$ dB. The patients are placed at a distance $d = 3$ m, where the CN is pointed straight towards the ceiling. . . . . 89

5.11 BER versus the average electrical transmit power $P_{t(\text{elec})}$ for different distance $d$ of the desired user from the center of the cell: (a) considering $\Gamma_{\text{ACO}} \approx 0.5$ bps/Hz, (4-QAM, $\mathscr{M} = 4$) (b) $\Gamma_{\text{ACO}} \approx 1$ bps/Hz (16-QAM, $\mathscr{M} = 4$). MAI is the case where the fifteen other patients are positioned at the cell center. NMAI refers to the no-MAI. . . . . 91

5.12 Spectral magnitude of ACO-ROFDMA signals for the case of two users: (a) Without signal clipping, (b) With the effect of clipping noise. . . . . 92

5.13 $P_{\text{out}}$ performance of ACO-ROFDMA due to random Tx orientation for different distance $d$ of the desired user and $\Gamma_{\text{ACO}} \approx 1$ bps/Hz (16-QAM, $\mathscr{M} = 4$). . . . . 92

5.14 Illustration of a radix-2 IFFT algorithm for a length $\mathscr{N}$=8, considering the DCO-ROFDMA scheme. $W_{\mathscr{N}}^{\hat{k}}$ is the so-called “twiddle factor" [222]. . . . . 93

5.15 Complexity analysis of different schemes in terms of required number of arithmetic operations at the Tx versus the number of data-carrying symbols $\mathscr{M}$; $\mathscr{N} = \mathscr{M}\mathscr{L}$ with $\mathscr{L} = 16$. . . . 94

6.1 Block diagram of the OOK O-CDMA based extra-WBAN system; Blocks Mod and DeMod stand for modulator and demodulator. Signal sampling at the TIA output is done at sampling period of $T_c$. . . . . 97

6.2 Different types of Rx structures (a) Correlation Rx: Based on a simple correlator, (b) CLD: The correlation is done based on the received power of each chip, (c) CHL: An HL is added before a simple correlator. . . . . 98

6.3 Overall architectures of (a) a CN (Tx) and (b) the AP (Rx) with a focus on the main AFE blocks. 99

6.4 The off-the-shelf AFE board for IR optical transmission and reception. . . . . 100

6.5 Conceptual block diagram of CN digital HW based on O-CDMA for extra-WBAN links. SIPO, PISO, and MUX stand for serial-in parallel-out, parallel-in serial-out shift register, and multiplexer, respectively. . . . . 101

6.6 Conceptual block diagram of AP digital HW based on O-CDMA corresponding to one user. Here, AV stands for acquisition and verification. The "ST" block generates early and late replicas of the spread data. . . . . 102

6.7 Txs and Rx timing diagrams captured through ILA for the case of wired transmission link: (a) Txs send spread data through an OR logic by the port $sp_out_comb$, (b) transmitted data of both Txs are recovered by the Rx. . . . . 104

6.8 Experimental setup. Here, Txs are placed at a distance of 1 m from the Rx. . . . . 104

6.9 Recovered data from the two Txs which are positioned at a distance of 20 cm from the Rx. The data were read through the built-in ILA of FPGA via a JTAG port. . . . . 105

6.10 Measured BER and FER from experiments, where distance $Z$ between the Txs and the Rx was varied from 20 cm to 1 m. . . . . 106

A.1 LOS and diffuse link with randomly oriented Tx. The incident angle $\upsilon$ is determined by applying trigonometry of the rectangular coordinates. . . . . 111

B.1 Digital design concept of the "AV" block employing matched-filter algorithm. Here, Th refers to the threshold. . . . . 113

# List of Tables

1.1 Frequency bands and their bandwidths of IEEE 802.15.6 PHY layers [15]. . . . . 11
1.2 Data-rate and QoS requirements for some popular medical WBAN sensors, reproduced from [33]. . . . . 14

2.1 Typical characteristics of the different PD technologies, reproduced from [97, 98]. . . . . 28

3.1 Main features of different code-domain NOMA schemes, reproduced from [178]. . . . . 49

4.1 Parameters used for numerical simulations. . . . . 64

5.1 Parameters used for numerical simulations. . . . . 85
5.2 Computational complexity of different MA schemes. . . . . 93

6.1 Logic resources required at CN. LUT and BUFGCTRL stand for look-up table and global clock buffer. . . . . 103
6.2 Parameters used in the experiment. . . . . 105

# Bibliography


[1] World Health Organization, *World health statistics 2019: monitoring health for the SDGs, sustainable development goals*, World Health Organization, 2019.

[2] P. K. Plunkett, D. G. Byrne, T. Breslin, K. Bennett, and B. Silke, "Increasing wait times predict increasing mortality for emergency medical admissions," *European Journal of Emergency Medicine*, vol. 18, pp. 192–196, Aug. 2011.

[3] World Health Organizations, "Report of the WHO-China Joint Mission on Coronavirus Disease 2019 (COVID-19)," Tech. Rep., Feb 2020.

[4] S. M. A. Iqbal, I. Mahgoub, E. Du, M. A. Leavitt, and W. Asghar, "Advances in healthcare wearable devices," *npj Flexible Electronics*, vol. 5, no. 1, pp. 1–14, April 2021.

[5] T. Wu, F. Wu, J. Redouté, and M. R. Yuce, "An autonomous wireless body area network implementation towards IoT connected healthcare applications," *IEEE Access*, vol. 5, pp. 11413–11422, June 2017.

[6] P. Pawar, V. Jones, B-. J. F. van Beijnum, and H. Hermens, "A framework for the comparison of mobile patient monitoring systems," *Journal of Biomedical Informatics*, vol. 45, no. 3, pp. 544–556, Mar. 2012.

[7] C. Crico, C. Renzi, N. Graf, A. Buyx, H. Kondylakis, L. Koumakis, and G. Pravettoni, "mHealth and telemedicine apps: in search of a common regulation," *Ecancermedicalscience*, vol. 12, July 2018.

[8] X. Ding, D. Clifton, N. Ji, N. H. Lovell, P. Bonato, W. Chen, X. Yu, Z. Xue, T. Xiang, X. Long, K. Xu, X. Jiang, Q. Wang, B. Yin, G. Feng, and Y. T. Zhang, "Wearable sensing and telehealth technology with potential applications in the coronavirus pandemic," *IEEE Reviews in Biomedical Engineering*, vol. 14, pp. 48–70, May 2020.

[9] H. Oh, C. Rizo, M. Enkin, and A. Jadad, "What is eHealth (3): A systematic review of published definitions," *Journal of Medical Internet Research*, vol. 7, no. 1, pp. e1, Feb. 2005.

[10] A. Ali, Y. Ming, S. Chakraborty, and S. Iram, "A comprehensive survey on real-time applications of WSN," *Future Internet*, vol. 9, no. 4, pp. 77, Nov. 2017.

[11] E. Jovanov and A. Milenkovic, "Body area networks for ubiquitous healthcare applications: Opportunities and challenges," *Journal of Medical Systems*, vol. 35, no. 5, pp. 1245–1254, April 2011.

[12] D. P. Tobón, T. H. Falk, and M. Maier, "Context awareness in WBANs: a survey on medical and non-medical applications," *IEEE Wireless Communications*, vol. 20, no. 4, pp. 30–37, Sep. 2013.

[13] H. Cao, V. Leung, C. Chow, and H. Chan, "Enabling technologies for wireless body area networks: A survey and outlook," *IEEE Communications Magazine*, vol. 47, no. 12, pp. 84–93, Dec. 2009.

[14] T. G. Zimmerman, "Personal area networks: Near-field intrabody communication," *IBM Systems Journal*, vol. 35, no. 3.4, pp. 609–617, 1996.

[15] "IEEE standard for local and metropolitan area networks - part 15.6: Wireless body area networks," *IEEE Std 802.15.6-2012*, pp. 1–271, Feb. 2012.

[16] H. Fernández-López, P. Macedo, J. A. Afonso, J. H. Correia, and R. Simões, "Performance evaluation of a zigbee-based medical sensor network," in *3rd International Conference on Pervasive Computing Technologies for Healthcare*, Apr. 2009, pp. 1–4, London, UK.

[17] G. Lo, S. González-Valenzuela, and V. C. M. Leung, "Automatic identification and placement verification of wearable wireless sensor nodes using atmospheric air pressure distribution," in *IEEE Consumer Communications and Networking Conference (CCNC)*, Apr. 2012, pp. 32–33, Las Vegas, NV.

[18] M. N. Deylami and E. Jovanov, "A distributed scheme to manage the dynamic coexistence of IEEE 802.15.4-based health-monitoring WBANs," *IEEE Journal of Biomedical and Health Informatics*, vol. 18, no. 1, pp. 327–334, Aug. 2014.

[19] J. Wannenburg and R. Malekian, "Body sensor network for mobile health monitoring, a diagnosis and anticipating system," *IEEE Sensors Journal*, vol. 15, no. 12, pp. 6839–6852, Aug. 2015.

[20] M. F. A. Rasid and B. Woodward, "Bluetooth telemedicine processor for multichannel biomedical signal transmission via mobile cellular networks," *IEEE Transactions on Information Technology in Biomedicine*, vol. 9, no. 1, pp. 35–43, Mar. 2005.

[21] E. Rebeiz, G. Caire, and A. F. Molisch, "Energy-delay tradeoff and dynamic sleep switching for bluetooth-like body-area sensor networks," *IEEE Transactions on Communications*, vol. 60, no. 9, pp. 2733–2746, Sept. 2012.

[22] A. Al-Fuqaha, M. Guizani, M. Mohammadi, M. Aledhari, and M. Ayyash, "Internet of Things: A survey on enabling technologies, protocols, and applications," *IEEE Communications Surveys & Tutorials*, vol. 17, no. 4, pp. 2347–2376, June 2015.

[23] S. Kumar and V. K. Chaurasiya, "A strategy for elimination of data redundancy in Internet of Things (IoT) based wireless sensor network (WSN)," *IEEE Systems Journal*, vol. 13, no. 2, pp. 1650–1657, Oct. 2019.

[24] S. Arora, "IoMT (Internet of Medical Things): Reducing cost while improving patient care," *IEEE Pulse*, vol. 11, no. 5, pp. 24–27, Oct. 2020.

[25] E. Selem, M. Fatehy, and S. M. A. El-Kader, "mobTHE (mobile temperature heterogeneity energy) aware routing protocol for WBAN IoT health application," *IEEE Access*, vol. 9, pp. 18692–18705, Jan. 2021.

[26] M. Hämäläinen, L. Mucchi, M. Girod-Genet, T. Paso, J. Farserotu, H. Tanaka, D. Anzai, L. Pierucci, R. Khan, M. M. Alam, and P. Dallemagne, "ETSI SmartBAN architecture: The global vision for smart body area networks," *IEEE Access*, vol. 8, pp. 150611–150625, Aug. 2020.

[27] ETSI, "Smart Body Area Networks (SmartBAN): System Description," *TR 103 394 - V1.1.1*, Jan. 2018.

[28] M. Chen, S. Gonzalez, A. Vasilakos, H. Cao, and V. C. M. Leung, "Body area networks: A survey," *Mobile Networks and Applications*, vol. 16, no. 2, pp. 171–193, Aug. 2010.

[29] B. Latré, B. Braem, I. Moerman, C. Blondia, and P. Demeester, "A survey on wireless body area networks," *Wireless Networks*, vol. 17, no. 1, pp. 1–18, Jan. 2011.

[30] S. Movassaghi, M. Abolhasan, J. Lipman, D. Smith, and A. Jamalipour, "Wireless body area networks: A survey," *IEEE Communications Surveys & Tutorials*, vol. 16, no. 3, pp. 1658–1686, Mar. 2014.

[31] A. Darwish and A. E. Hassanien, "Wearable and implantable wireless sensor network solutions for healthcare monitoring," *Sensors*, vol. 11, no. 6, pp. 5561–5595, May 2011.

[32] O. Haddad, M. A. Khalighi, S. Zvanovec, and M. Adel, "Channel characterization and modeling for optical wireless body-area networks," *IEEE Open Journal of the Communications Society*, vol. 1, pp. 760–776, June 2020.

[33] O. Haddad and M. A. Khalighi, "Enabling communication technologies for medical wireless body-area networks," in *Global LiFi Congress (GLC)*, June 2019, pp. 1–5, Paris, France.

[34] M. Shu, D. Yuan, C. Zhang, Y. Wang, and C. Chen, "A MAC protocol for medical monitoring applications of wireless body area networks," *Sensors*, vol. 15, no. 6, pp. 12906–12931, June 2015.

[35] E. Agrell and M. Secondini, "Information-theoretic tools for optical communications engineers," in *IEEE Photonics Conference (IPC)*, Sept. 2018, pp. 1–5, Reston, VA.

[36] R. Cavallari, F. Martelli, R. Rosini, C. Buratti, and R. Verdone, "A survey on wireless body area networks: Technologies and design challenges," *IEEE Communications Surveys & Tutorials*, vol. 16, no. 3, pp. 1635–1657, Mar. 2014.

[37] A. Bachir, M. Dohler, T. Watteyne, and K. K. Leung, "MAC essentials for wireless sensor networks," *IEEE Communications Surveys & Tutorials*, vol. 12, no. 2, pp. 222–248, Apr. 2010.

[38] M. U. Rehman, I. Uddin, M. Adnan, A. Tariq, and S. Malik, "VTA-SMAC: variable traffic-adaptive duty cycled sensor MAC protocol to enhance overall QoS of S-MAC protocol," *IEEE Access*, vol. 9, pp. 33030–33040, Feb. 2021.

[39] S. M. Demir, F. Al-Turjman, and A. Muhtaroğlu, "Energy scavenging methods for WBAN applications: A review," *IEEE Sensors Journal*, vol. 18, no. 16, pp. 6477–6488, June 2018.

[40] H. Liu, F. Hu, S. Qu, Z. Li, and D. Li, "Multipoint wireless information and power transfer to maximize sum-throughput in WBAN with energy harvesting," *IEEE Internet of Things Journal*, vol. 6, no. 4, pp. 7069–7078, April 2019.

[41] M. S. Hajar, M. O. Al-Kadri, and H. K. Kalutarage, "A survey on wireless body area networks: architecture, security challenges and research opportunities," *Computers & Security*, vol. 104, pp. 102211, Jan. 2021.

[42] M. Toorani, "Security analysis of the IEEE 802.15.6 standard," *International Journal of Communication Systems*, vol. 29, pp. 2471–2489, Feb. 2016.

[43] I. H. Hahn, D. Schnadower, R. J. Dakin, and L. S. Nelson, "Cellular phone interference as a cause of acute epinephrine poisoning," *Annals of Emergency Medicine*, vol. 46, no. 3, pp. 298–299, Sep. 2005.

[44] R. van der Togt, E. Jan van Lieshout, R. Hensbroek, E. Beinat, J. M. Binnekade, and P. J. M. Bakker, "Electromagnetic interference from radio frequency identification inducing potentially hazardous incidents in critical care medical equipment METHODS background," *JAMA*, vol. 299, no. 24, pp. 2884–2890, June 2008.

[45] M. F. Shaik, V. L. N. Komanapalli, and M. M. Subashini, "A comparative study of interference and mitigation techniques in wireless body area networks," *Wireless Personal Communications*, vol. 98, pp. 2333–2365, Oct. 2017.

[46] M. Hernandez and R. Miura, "Coexistence of IEEE Std 802.15.6TM-2012 UWB-PHY with other UWB systems," in *IEEE International Conference on Ultra-Wideband*, Sept. 2012, pp. 46–50, Syracuse, NY.

[47] G. Ahmed, S. U. Islam, M. Shahid, A. Akhunzada, S. Jabbar, M. K. Khan, M. Riaz, and K. Han, "Rigorous analysis and evaluation of specific absorption rate (SAR) for mobile multimedia healthcare," *IEEE Access*, vol. 6, pp. 29602–29610, May 2018.

[48] Z. Ghassemlooy, W. Popoola, and S. Rajbhandari, *Optical Wireless Communications: System and Channel Modelling with MATLAB*, CRC Press, Inc., 2nd edition, 2019.

[49] Z. Ghassemlooy, L. N. Alves, S. Zvanovec, and M. A. Khalighi, Eds., *Visible Light Communications: Theory and Applications*, CRC-Press, 2017.

[50] H. Haas, L. Yin, Y. Wang, and C. Chen, "What is LiFi?," *Journal of Lightwave Technology*, vol. 34, no. 6, pp. 1533–1544, Mar. 2016.

[51] Emmanuel Ghesquier, "Ces 2019 : le lifi (internet par la lumière) est enfin prêt à se démocratiser," Jan. 2019, Accessed: 2021-9-24.

[52] J. M. Kahn and J. R. Barry, "Wireless infrared communications," *Proceedings of the IEEE*, vol. 85, no. 2, pp. 265–298, Feb. 1997.

[53] B. Béchadergue, L. Chassagne, and H. Guan, "Simultaneous visible light communication and distance measurement based on the automotive lighting," *IEEE Transactions on Intelligent Vehicles*, vol. 4, no. 4, pp. 532–547, Dec. 2019.

[54] M. A. Khalighi and M. Uysal, "Survey on free space optical communication: A communication theory perspective," *IEEE Communications Surveys & Tutorials*, vol. 16, no. 4, pp. 2231–2258, June 2014.

[55] M. A. Khalighi, T. Hamza, S. Bourennane, P. Léon, and J. Opderbecke, "Underwater wireless optical communications using silicon photo-multipliers," *IEEE Photonics Journal*, vol. 9, no. 4, pp. 1–10, July 2017.

[56] C. Shen, Y. Guo, H. M. Oubei, T. K. Ng, G. Liu, K.-H. Park, K.-T. Ho, M.-S. Alouini, and B. S. Ooi, "20-meter underwater wireless optical communication link with 1.5 gbps data rate," *Optics Express*, vol. 24, no. 22, pp. 25502–25509, Oct. 2016.

[57] "H2020-MSCA-ITN VISION," https://www.vision-itn.eu/, 2017, Accessed: 2021-9-24.

[58] F. T. Zuhra, K. B. A. Bakar, A. A. Arain, U. A. Khan, and A. R. Bhangwar, "MIQoS-RP: multi-constraint Intra-BAN, QoS-aware routing protocol for wireless body sensor networks," *IEEE Access*, vol. 8, pp. 99880–99888, May 2020.

[59] C. Massaroni, C. Venanzi, A. P Silvatti, D. L. Presti, P. Saccomandi, D. Formica, F. Giurazza, M. A Caponero, and E. Schena, "Smart textile for respiratory monitoring and thoraco-abdominal motion pattern evaluation," *Journal of Biophotonics*, vol. 11, no. 5, may 2018.

[60] M. A. Meghrazi, Y. Tian, A. Mahnam, P. Bhattachan, L. Eskandarian, S. T. Kakhki, M. R. Popovic, and M. Lankarany, "Multichannel ECG recording from waist using textile sensors," *BioMedical Engineering OnLine*, vol. 19, no. 1, pp. 1–18, June 2020.

[61] O. Haddad, *Channel Modeling and Multiple Access Solutions for Medical Wireless Body-Area Networks based on Optical Wireless Technology*, PhD thesis, École Centrale Marseille, Marseille, France, July 2021.

[62] T. B. Hoang, S. Sahuguède, and A. Julien-Vergonjanne, "Optical wireless network design for off-body-sensor based monitoring," *Wireless Communications and Mobile Computing*, vol. 2019, pp. 13, Sep. 2019.

[63] IEC-62471, "Photobiological safety of lamps and lamp systems," Standard, International Electrotechnical Commission, Geneva, Switzerland, 2008.

[64] Y. Qiu, S. Chen, H. H. Chen, and W. Meng, "Visible light communications based on CDMA technology," *IEEE Wireless Communications*, vol. 25, no. 2, pp. 178–185, Sept. 2018.

[65] W. Wei, C. Wang, J. Yu, N. Cvijetic, and T. Wang, "Optical orthogonal frequency division multiple access networking for the future internet," *IEEE/OSA Journal of Optical Communications and Networking*, vol. 1, no. 2, pp. A236–A246, July 2009.

[66] Behlouli, P. Combeau, S. Sahuguède, A. Julien-Vergonjanne, C. Le Bas, and L. Aveneau, "Impact of physical and geometrical parameters on visible light communication links," in *Advances in Wireless and Optical Communications (RTUWO)*, Nov. 2017, pp. 73–76, Riga, Latvia.

[67] M. H. Chang, D. Das, P.V. Varde, and M. Pecht, "Light emitting diodes reliability review," *Microelectronics Reliability*, vol. 52, no. 5, pp. 762–782, July 2012.

[68] T. Komine and M. Nakagawa, "Fundamental analysis for visible-light communication system using led lights," *IEEE Transactions on Consumer Electronics*, vol. 50, no. 1, pp. 100–107, Feb. 2004.

[69] J. B. Carruther and J. M. Kahn, "Angle diversity for nondirected wireless infrared communication," *IEEE Transactions on Communications*, vol. 48, no. 6, pp. 960–969, June 2000.

[70] S. Dimitrov and H. Haas, *Principles of LED Light Communications: Towards Networked Li-Fi*, Cambridge University Press, Jan. 2015.

[71] F. R. Gfeller and U. Bapst, "Wireless in-house data communication via diffuse infrared radiation," *Proceedings of the IEEE*, vol. 67, no. 11, pp. 1474–1486, Nov. 1979.

[72] J. R. Barry, J. M. Kahn, E. A. Lee, and D.G. Messerschmitt, "High-speed nondirective optical communication for wireless networks," *IEEE Network*, vol. 5, no. 6, pp. 44–54, Nov. 1991.

[73] N. Holonyak, S. F. Bevacqua, C. V. Bielan, F. A. Carranti, B. G. Hess, and S. J. Lubowski, "Electrical properties of Ga(As1-xPx) p-n junctions," *Proceedings of the IEEE*, vol. 51, no. 2, pp. 364–364, Feb. 1963.

[74] S. Nakamura, T. Mukai, and M. Senoh, "High-power GaN p-n junction blue-light-emitting diodes," *Japanese Journal of Applied Physics*, vol. 30, no. Part 2, No. 12A, pp. L1998–L2001, Dec. 1991.

[75] Y. Tanaka, S. Haruyama, and M. Nakagawa, "Wireless optical transmissions with white colored LED for wireless home links," in *11th IEEE International Symposium on Personal Indoor and Mobile Radio Communications (PIMRC)*, Sep. 2000, vol. 2, pp. 1325–1329, London, UK.

[76] Y. Tanaka, T. Komine, S. Haruyama, and M. Nakagawa, "Indoor visible communication utilizing plural white LEDs as lighting," in *12th IEEE International Symposium on Personal, Indoor and Mobile Radio Communications (PIMRC)*, Sep. 2001, vol. 2, pp. 81–85, San Diego, CA.

[77] Y. F. Liu, C. H. Yeh, C. W. Chow, Y. Liu, Y. L. Liu, and H. K. Tsang, "Demonstration of bidirectional LED visible light communication using TDD traffic with mitigation of reflection interference," *Optics Express*, vol. 20, no. 21, pp. 23019–23024, Oct 2012.

[78] Y. Wang, N. Chi, Y. Wang, L. Tao, and J. Shi, "Network architecture of a high-speed visible light communication local area network," *IEEE Photonics Technology Letters*, vol. 27, no. 2, pp. 197–200, Jan. 2015.

[79] A. Sewaiwar, S. Vikramaditya Tiwari, and Yeon H. C., "Mobility support for full-duplex multiuser bidirectional VLC networks," *IEEE Photonics Journal*, vol. 7, no. 6, pp. 1–9, Oct. 2015.

[80] L.-Y. Wei, C.-W. Chow, C.-W. Hsu, and C.-H. Yeh, "Bidirectional visible light communication system using a single VCSEL with predistortion to enhance the upstream remodulation," *IEEE Photonics Journal*, vol. 10, no. 3, pp. 1–7, April 2018.

[81] W. Yuanquan and C. Nan, "A high-speed bi-directional visible light communication system based on RGB-LED," *China Communications*, vol. 11, no. 3, pp. 40–44, Mar. 2014.

[82] M. T. Alresheedi, A. T. Hussein, and J. M. H. Elmirghani, "Uplink design in VLC systems with IR sources and beam steering," *IET Communications*, vol. 11, no. 3, pp. 311–317, Feb. 2017.

[83] H. Haas, L. Yin, C. Chen, S. Videv, D. Parol, E. Poves, H. Alshaer, and M. Sufyan Islim, "Introduction to indoor networking concepts and challenges in LiFi," *Journal of Optical Communications and Networking*, vol. 12, no. 2, pp. A190–A203, Feb. 2020.

[84] H. M. Oubei, C. Li, K.-H. Park, T. K. Ng, M.-S. Alouini, and B. S. Ooi, "2.3 Gbit/s underwater wireless optical communications using directly modulated 520 nm laser diode," *Optics Express*, vol. 23, no. 16, pp. 20743–20748, Aug 2015.

[85] F. Feng, I. H. White, and T. D. Wilkinson, "Free space communications with beam steering a two-electrode tapered laser diode using liquid-crystal SLM," *Journal of Lightwave Technology*, vol. 31, no. 12, pp. 2001–2007, May 2013.

[86] F. Zafar, M. Bakaul, and R. Parthiban, "Laser-diode-based visible light communication: Toward Gigabit class communication," *IEEE Communications Magazine*, vol. 55, no. 2, pp. 144–151, Feb. 2017.

[87] D. Tsonev, D. Videv, and H. Haas, "Towards a 100 Gb/s visible light wireless access network," *Optics Express*, vol. 23, no. 2, pp. 1627–1637, Jan. 2015.

[88] S. Watson, M. Tan, S. P. Najda, P. Perlin, M. Leszczynski, G. Targowski, S. Grzanka, and A. E. Kelly, "Visible light communications using a directly modulated 422 nm GaN laser diode," *Optics Letters*, vol. 38, no. 19, pp. 3792–3794, Oct 2013.

[89] C. Lee, C. Zhang, M. Cantore, R. M. Farrell, S. H. Oh, T. M., J. S. Speck, S. N., J. E. Bowers, and S. P. DenBaars, "4 gbps direct modulation of 450 nm gan laser for high-speed visible light communication," *Optics Express*, vol. 23, no. 12, pp. 16232–16237, June 2015.

[90] A. T. Hussein and J. M. H. Elmirghani, "Mobile multi-gigabit visible light communication system in realistic indoor environment," *Journal of Lightwave Technology*, vol. 33, no. 15, pp. 3293–3307, June 2015.

[91] Z. Wei, S. Zhang, S. Mao, L. Wang, L. Zhang, C.-J. Chen, M.-C. Wu, Y. Dong, L. Wang, Y. Luo, and H. Y. Fu, "Full-duplex high-speed indoor optical wireless communication system based on a micro-LED and VCSEL array," *Optics Express*, vol. 29, no. 3, pp. 3891–3903, Feb. 2021.

[92] IEC-60825-1, "Safety of laser products - part 1: Equipment classification and requirements," Standard, International Electrotechnical Commission, Geneva, Switzerland, 2014.

[93] C. Basu, M. M-. Wollweber, and B. Roth, "Lighting with laser diodes," *Advanced Optical Technologies*, vol. 2, no. 4, pp. 313–321, Aug. 2013.

[94] P. H. Pathak, X. Feng, P. Hu, and P. Mohapatra, "Visible light communication, networking, and sensing: A survey, potential and challenges," *IEEE Communications Surveys Tutorials*, vol. 17, no. 4, pp. 2047–2077, Sept. 2015.

[95] F. Acerbi, G. Paternoster, M. Capasso, M. Marcante, A. Mazzi, V. Regazzoni, N. Zorzi, and A. Gola, "Silicon photomultipliers: Technology optimizations for ultraviolet, visible and near-infrared range," *Instruments*, vol. 3, no. 1, Feb. 2019.

[96] L. Zhang, H. Chun, Z. Ahmed, G. Faulkner, D. O'Brien, and S. Collins, "The future prospects for SiPM-based receivers for visible light communications," *Journal of Lightwave Technology*, vol. 37, no. 17, pp. 4367–4374, June 2019.

[97] J. Wallace, "Photonics Products: Photodiodes: Silicon low-light photodiodes don't miss a photon | Laser Focus World," Sep. 2014.

[98] E. Hergert and S. Piatek, "The WITS$ guide to selecting a photodetector," Tech. Rep., Hamamatsu, May 2017.

[99] O. Haddad, M. A. Khalighi, S. Zvanovec, and M. Adel, "Performance analysis of optical intra-WBAN links," in *International Symposium on Communication Systems, Networks and Digital Signal Processing (CSNDSP)*, July 2020, pp. 1–6, Porto, Portugal.

[100] M. Gao, C. Li, and Z. Xu, "Optimal transmission of VLC system in the presence of LED nonlinearity and APD module saturation," *IEEE Photonics Journal*, vol. 10, no. 5, pp. 1–14, Sep. 2018.

[101] P. Brandl, T. Jukić, R. Enne, K. Schneider-Hornstein, and H. Zimmermann, "Optical wireless APD receiver with high background-light immunity for increased communication distances," *IEEE Journal of Solid-State Circuits*, vol. 51, no. 7, pp. 1663–1673, May 2016.

[102] E. Kamrani, F. Lesage, and M. Sawan, "Low-noise, high-gain transimpedance amplifier integrated with SiAPD for low-intensity near-infrared light detection," *IEEE Sensors Journal*, vol. 14, no. 1, pp. 258–269, Jan. 2014.

[103] F. Xu, M. Khalighi, and S. Bourennane, "Impact of different noise sources on the performance of PIN- and APD-based FSO receivers," in *11th International Conference on Telecommunications (CONTEL)*, June 2011, pp. 211–218, Graz, Austria.

[104] L. Chevalier, S. Sahuguède, and A. Julien-Vergonjanne, "Optical wireless links as an alternative to radio-frequency for medical body area networks," *IEEE Journal on Selected Areas in Communications*, vol. 33, no. 9, pp. 2002–2010, Sept. 2015.

[105] N. Barbot, S. Sahuguède, and A. Julien-Vergonjanne, "Performance of a mobile wireless optical CDMA monitoring system," in *International Symposium on Wireless Communication Systems (ISWCS)*, Aug. 2012, pp. 666–670, Paris, France.

[106] M. Phiri, "Health building note 00-01. General design guidance for healthcare buildings," Tech. Rep., Department of Health (DH), 2014.

[107] L. Chevalier, S. Sahuguède, and A. Julien-Vergonjanne, "Wireless optical technology based body area network for health monitoring application," in *IEEE International Conference on Communications (ICC)*, June 2015, pp. 2863–2868, London, UK.

[108] C. Le Bas, T. B. Hoang, S. Sahuguede, and A. Julien-Vergonjanne, "Lighting fixture communicating in infrared and visible for indoor health monitoring," in *IEEE 19th International Conference on e-Health Networking, Applications and Services (Healthcom)*, Dec. 2017, pp. 1–6, Dalian, China.

[109] O. Haddad, M. A. Khalighi, and S. Zvanovec, "Channel characterization for optical extra-WBAN links considering local and global user mobility," in *Broadband Access Communication Technologies XIV*. Feb. 2020, vol. 11307, pp. 89 – 97, SPIE Photonics West Conference, San Francisco, CA.

[110] A. Kaba, S. Sahuguede, and A. Julien-Vergonjanne, "Investigating the performance of a worn optical wireless device with mobility," in *12th International Symposium on Communication Systems, Networks and Digital Signal Processing (CSNDSP)*, 2020, pp. 1–6, Porto, PT.

[111] A. Kaba, S. Sahuguede, and A. Julien-Vergonjanne, "Channel modeling of an optical wireless body sensor network for walk monitoring of elderly," *Sensors*, vol. 21, no. 9, Apr. 2021.

[112] J. R. Barry, J. M. Kahn, W. J. Krause, E. A. Lee, and D. G. Messerschmitt, "Simulation of multipath impulse response for indoor wireless optical channels," *IEEE Journal on Selected Areas in Communications*, vol. 11, no. 3, pp. 367–379, Apr. 1993.

[113] C. Gabriel, M. A. Khalighi, S. Bourennane, P. Léon, and V. Rigaud, "Investigation of suitable modulation techniques for underwater wireless optical communication," in *International Workshop on Optical Wireless Communications (IWOW)*, Nov. 2012, pp. 1–3, Pisa, Italy.

[114] IRDA SIR data specification, "Serial infrared physical layer specification," Standard, Infrared Data Association, 2001.

[115] S. S. Torkestani, N. Barbot, S. Sahuguede, A. Julien-Vergonjanne, and J. P. Cances, "Performance and transmission power bound analysis for optical wireless based mobile healthcare applications," in *IEEE 22nd International Symposium on Personal, Indoor and Mobile Radio Communications*, Sept. 2011, pp. 2198–2202, Toronto, ON.

[116] F. Xu, M. A. Khalighi, and S. Bourennane, "Efficient channel coding for multipulse pulse position modulation in terrestrial FSO systems," in *Free-Space Laser Communications IX*, Arun K. Majumdar and Christopher C. Davis, Eds. International Society for Optics and Photonics, 2009, vol. 7464, pp. 204 – 215, SPIE.

[117] F. Buchali, R. Dischler, and X. Liu, "Optical OFDM: a promising high-speed optical transport technology," *Bell Labs Technical Journal*, vol. 14, no. 1, pp. 125–146, Spring 2009.

[118] J. B. Carruthers and J. M. Kahn, "Multiple-subcarrier modulation for nondirected wireless infrared communication," *IEEE Journal on Selected Areas in Communications*, vol. 14, no. 3, pp. 538–546, Apr. 1996.

[119] J. Armstrong, "OFDM for optical communications," *Journal of Lightwave Technology*, vol. 27, no. 3, pp. 189–204, Feb. 2009.

[120] T. Essalih, M. A. Khalighi, S. Hranilovic, and H. Akhouayri, "Optical OFDM for SiPM-based underwater optical wireless communication links," *Sensors*, vol. 20, no. 21, Oct. 2020.

[121] A. Al-Kinani, C.-X. Wang, L. Zhou, and W. Zhang, "Optical wireless communication channel measurements and models," *IEEE Communications Surveys & Tutorials*, vol. 20, no. 3, pp. 1939–1962, May 2018.

[122] C. R. Lomba, R. T. Valadas, and A. M. de Oliveira Duarte, "Efficient simulation of the impulse response of the indoor wireless optical channel," *International Journal of Communication Systems*, vol. 13, no. 7-8, pp. 537–549, Nov. 2000.

[123] J. B. Carruthers and P. Kannan, "Iterative site-based modeling for wireless infrared channels," *IEEE Transactions on Antennas and Propagation*, vol. 50, no. 5, pp. 759–765, Aug. 2002.

[124] V. Jungnickel, V. Pohl, S. Nonnig, and C. von Helmolt, "A physical model of the wireless infrared communication channel," *IEEE Journal on Selected Areas in Communications*, vol. 20, no. 3, pp. 631–640, Aug. 2002.

[125] F. J. López-Hernández and M. J. Betancor, "DUSTIN: Algorithm for calculation of impulse response on IR wireless indoor channels," *Electronics Letters*, vol. 33, pp. 1804–1806(2), Oct. 1997.

[126] F. J. López-Hernández, R. Pérez-Jiménez, and A. Santamaría, "Monte Carlo calculation of impulse response on diffuse IR wireless indoor channels," *Electronics Letters*, vol. 34, pp. 1260–1262(2), June 1998.

[127] F. J. López-Hernández, R. Pérez-Jiménez, and A. Santamaría, "Modified Monte Carlo scheme for high-efficiency simulation of the impulse response on diffuse IR wireless indoor channels," *Electronics Letters*, vol. 34, pp. 1819–1820(1), Sept. 1998.

[128] M. I. S. Chowdhury, W. Zhang, and M. Kavehrad, "Combined deterministic and modified Monte Carlo method for calculating impulse responses of indoor optical wireless channels," *Journal of Lightwave Technology*, vol. 32, no. 18, pp. 3132–3148, July 2014.

[129] J. M. Kahn, W. J. Krause, and J. B. Carruthers, "Experimental characterization of non-directed indoor infrared channels," *IEEE Transactions on Communications*, vol. 43, no. 2/3/4, pp. 1613–1623, Feb. 1995.

[130] M. R. Pakravan and M. Kavehrad, "Indoor wireless infrared channel characterization by measurements," *IEEE Transactions on Vehicular Technology*, vol. 50, no. 4, pp. 1053–1073, July 2001.

[131] H. B. Eldeeb, M. Uysal, S. M. Mana, P. Hellwig, J. Hilt, and V. Jungnickel, "Channel modelling for light communications: Validation of ray tracing by measurements," in *12th International Symposium on Communication Systems, Networks and Digital Signal Processing (CSNDSP)*, July 2020, pp. 1–6, Porto,PT.

[132] A. Julien-Vergonjanne, S. Sahuguède, and L. Chevalier, "Optical wireless body area networks for healthcare applications," in *Optical Wireless Communications: An Emerging Technology*, pp. 569–587. Springer International Publishing, 2016.

[133] S. Misra, J. Mahapatro, M. Mahadevappa, and N. Islam, "Random room mobility model and extra-wireless body area network communication in hospital buildings," *IET Networks*, vol. 4, no. 1, pp. 54–64, 2015.

[134] C. Le Bas, S. Sahuguede, and A. Julien-Vergonjanne, "Theoretical and experimental approach for the design of an optical wireless physical activity monitoring system," *International Journal of Wireless Information Networks*, vol. 24, pp. 65–77, Feb. 2017.

[135] S. Long, M. A. Khalighi, M. Wolf, S. Bourenanne, and Z. Ghassemlooy, "Investigating channel frequency selectivity in indoor visible light communication systems," *IET Optoelectronics*, vol. 10, no. 3, pp. 80–88, May 2016.

[136] Y. Qiu, H. H. Chen, and W. X. Meng, "Channel modeling for visible light communications-A survey," *Wireless Communications and Mobile Computing*, vol. 16, no. 14, pp. 2016–2034, 2016.

[137] M. M. Zonoozi and P. Dassanayake, "User mobility modeling and characterization of mobility patterns," *IEEE Journal on Selected Areas in Communications*, vol. 15, no. 7, pp. 1239–1252, Sept. 1997.

[138] D. B. Johnson and D. A. Maltz, *Dynamic Source Routing in Ad Hoc Wireless Networks*, pp. 153–181, Springer US, 1996.

[139] S. Althunibat, O. S. Badarneh, and R. Mesleh, "Random waypoint mobility model in space modulation systems," *IEEE Communications Letters*, vol. 23, no. 5, pp. 884–887, May 2019.

[140] P. Santi, *Group Mobility and Other Synthetic Mobility Models*, Wiley, 2012.

[141] L. Tu, F. Zhang, F. Wang, and X. Wang, "A random group mobility model for mobile networks," in *2009 Symposia and Workshops on Ubiquitous, Autonomic and Trusted Computing*, July 2009, pp. 551–556, Brisbane, QLD, Australia.

[142] X. Hong, M. Gerla, G. Pei, and C-. C. Chiang, "A group mobility model for ad hoc wireless networks," in *ACM International Workshop on Modeling, Analysis and Simulation of Wireless and Mobile Systems*. 1999, pp. 53–60, ACM, New York, NY.

[143] J. Le Boudec and M. Vojnovic, "The random trip model: stability, stationary regime, and perfect simulation," *IEEE/ACM Transactions on Networking*, vol. 14, no. 6, pp. 1153–1166, Dec. 2006.

[144] I. Rhee, M. Shin, S. Hong, K. Lee, S. J. Kim, and S. Chong, "On the levy-walk nature of human mobility," *IEEE/ACM Transactions on Networking*, vol. 19, no. 3, pp. 630–643, June 2011.

[145] D. Mitsche, R. Giovanni, and P. Santi, "The random waypoint mobility model with uniform node spatial distribution," *Wireless Networks*, vol. 20, no. 5, pp. 1053–1066, july 2014.

[146] M. D. Soltani, A. A. Purwita, Z. Zeng, H. Haas, and M. Safari, "Modeling the random orientation of mobile devices: measurement, analysis and LiFi use case," *IEEE Transactions on Communications*, vol. 67, no. 3, pp. 2157–2172, Mar. 2019.

[147] Jack B. Kuipers, *Quaternions and Rotation Sequences : A Primer with Applications to Orbits, Aerospace, and Virtual reality*, Princeton Univ. Press, 1999.

[148] T. Milligan, "More applications of Euler rotation angles," *IEEE Antennas and Propagation Magazine*, vol. 41, no. 4, pp. 78–83, Aug. 1999.

[149] Christian Bettstetter, Hannes Hartenstein, and Xavier Pérez-Costa, "Stochastic properties of the random waypoint mobility model," *Wireless Networks*, vol. 10, no. 5, pp. 555–567, Sept. 2004.

[150] Radhika Ranjan Roy, *Random Waypoint Mobility*, pp. 65–124, Springer US, Boston, MA, 2011.

[151] P. Wang, J. Xiao, and L. Ping, "Comparison of orthogonal and non-orthogonal approaches to future wireless cellular systems," *IEEE Vehicular Technology Magazine*, vol. 1, no. 3, pp. 4–11, Sep. 2006.

[152] M. W. Eltokhey, M. Khalighi, and Z. Ghassemlooy, "Multiple access techniques for VLC in large space indoor scenarios: A comparative study," in *International Conference on Telecommunications (ConTEL)*, July 2019, pp. 1–6, Graz, Austria.

[153] J. Ding, M. Nemati, C. Ranaweera, and J. Choi, "IoT connectivity technologies and applications: A survey," *IEEE Access*, vol. 8, pp. 67646–67673, Apr. 2020.

[154] J. An, N. Q. Pham, and W. Chung, "Multiple bio-monitoring system using visible light for electromagnetic-wave free indoor healthcare," *Optics Communications*, vol. 405, pp. 107–113, Aug. 2017.

[155] D. R. Dhatchayeny, S. Arya, and Y. H. Chung, "Infrared-based multiple-patient monitoring in indoor optical wireless healthcare systems," *IEEE Sensors Journal*, vol. 19, no. 14, pp. 5594–5599, July 2019.

[156] G. Sun, K. Wang, H. Yu, X. Du, and M. Guizani, "Priority-based medium access control for wireless body area networks with high-performance design," *IEEE Internet of Things Journal*, vol. 6, no. 3, pp. 5363–5375, June 2019.

[157] S. Al-Ahmadi, O. Maraqa, M. Uysal, and S. M. Sait, "Multi-user visible light communications: State-of-the-art and future directions," *IEEE Access*, vol. 6, pp. 70555–70571, Nov. 2018.

[158] D. V. Sarwate and M. B. Pursley, "Crosscorrelation properties of pseudorandom and related sequences," *Proceedings of the IEEE*, vol. 68, no. 5, pp. 593–619, May. 1980.

[159] B. M. Ghaffari, M. D. Matinfar, and J. A. Salehi, "Wireless optical CDMA LAN: digital design concepts," *IEEE Transactions on Communications*, vol. 56, no. 12, pp. 2145–2155, Dec. 2008.

[160] B. M. Ghaffari, M. D. Matinfar, and J. A. Salehi, "Wireless optical CDMA LAN: digital implementation analysis," *IEEE Journal on Selected Areas in Communications*, vol. 27, no. 9, pp. 1676–1686, Dec. 2009.

[161] S. Zahedi, J. A. Salehi, and M. Nasiri-Kenari, "A photon counting approach to the performance analysis of indoors wireless infrared CDMA networks," in *IEEE International Symposium on Personal Indoor and Mobile Radio Communications (PIMRC)*, Sept. 2000, vol. 2, pp. 928–932, London, UK.

[162] S. L. Dhomeja, T. B. Oon, and R. Steele, "Performance of non-directed infrared CDMA," in *International Conference on Universal Personal Communications*, Oct. 1998, vol. 1, pp. 453–457, Florence, Italy.

[163] A. Aminzadeh-Gohari and M. R. Pakravan, "Analysis of power control for indoor wireless infrared CDMA communication," in *IEEE International Performance Computing and Communications Conference*, Apr. 2006, pp. 297–302, Phoenix, AZ.

[164] S. Khazraei and M. R. Pakravan, "Power control analysis for indoor wireless infrared CDMA networks using BPPM," in *IEEE International Conference on Telecommunications and Malaysia International Conference on Communications*, May 2007, pp. 402–406, Penang, Malaysia.

[165] J. Armstrong and B. J. C. Schmidt, "Comparison of asymmetrically clipped optical OFDM and DC-biased optical OFDM in AWGN," *IEEE Communications Letters*, vol. 12, no. 5, pp. 343–345, May. 2008.

[166] M. Khalighi, S. Long, S. Bourennane, and Z. Ghassemlooy, "PAM- and CAP-based transmission schemes for visible-light communications," *IEEE Access*, vol. 5, pp. 27002–27013, Oct. 2017.

[167] H. Qian, S. J. Yao, S. Z. Cai, and T. Zhou, "Adaptive postdistortion for nonlinear LEDs in visible light communications," *IEEE Photonics Journal*, vol. 6, no. 4, pp. 1–8, June 2014.

[168] H. Elgala, R. Mesleh, and H. Haas, "An LED model for intensity-modulated optical communication systems," *IEEE Photonics Technology Letters*, vol. 22, no. 11, pp. 835–837, Apr. 2010.

[169] Shihe Long and Mohammad A. Khalighi, "Advantage of CAP signaling for VLC systems under non-linear LED characteristics," in *West Asian Colloquium on Optical Wireless Communications (WACOWC)*, Apr. 2019, pp. 21–25, Tehran, Iran.

[170] R. You and J. M. Kahn, "Average power reduction techniques for multiple-subcarrier intensity-modulated optical signals," *IEEE Transactions on Communications*, vol. 49, no. 12, pp. 2164–2171, Dec. 2001.

[171] Wei-Wen Hu, "SLM-based ACO-OFDM VLC system with low-complexity minimum amplitude difference decoder," *Electronics Letters*, vol. 54, pp. 144–146, Feb. 2018.

[172] W. O. Popoola, Z. Ghassemlooy, and B. G. Stewart, "Pilot-assisted PAPR reduction technique for optical OFDM communication systems," *Journal of Lightwave Technology*, vol. 32, no. 7, pp. 1374–1382, Feb. 2014.

[173] A. W. Azim, Y. Le Guennec, and G. Maury, "Hermitian symmetry free optical-single-carrier frequency division multiple access for visible light communication," *Optics Communications*, vol. 415, pp. 177 – 185, May 2018.

[174] H. G. Myung and D. J. Goodman, *Single Carrier FDMA*, pp. 37–59, Wiley, 2008.

[175] V. Jungnickel and L. Grobe, "Localized SC-FDMA with constant envelope," in *IEEE International Symposium on Personal, Indoor, and Mobile Radio Communications (PIMRC)*, Sept. 2013, pp. 24–29, London, UK.

[176] S. M. R. Islam, N. Avazov, O. A. Dobre, and K. Kwak, "Power-domain non-orthogonal multiple access (noma) in 5g systems: Potentials and challenges," *IEEE Communications Surveys Tutorials*, vol. 19, no. 2, pp. 721–742, Oct. 2017.

[177] M. Shirvanimoghaddam, M. Dohler, and S. J. Johnson, "Massive non-orthogonal multiple access for cellular IoT: Potentials and limitations," *IEEE Communications Magazine*, vol. 55, no. 9, pp. 55–61, Sept. 2017.

[178] M. Mohammadkarimi, M. A. Raza, and O. A. Dobre, "Signature-based nonorthogonal massive multiple access for future wireless networks: Uplink massive connectivity for machine-type communications," *IEEE Vehicular Technology Magazine*, vol. 13, no. 4, pp. 40–50, Oct. 2018.

[179] K. Au, L. Zhang, H. Nikopour, E. Yi, A. Bayesteh, U. Vilaipornsawai, J. Ma, and P. Zhu, "Uplink contention based SCMA for 5G radio access," in *IEEE Globecom Workshops (GC Wkshps)*, Dec. 2014, pp. 900–905, Austin,TX.

[180] Z. Yuan, G. Yu, W. Li, Y. Yuan, X. Wang, and J. Xu, "Multi-user shared access for internet of things," in *IEEE 83rd Vehicular Technology Conference (VTC Spring)*, May. 2016, pp. 1–5, Nanjing,China.

[181] S. Chen, B. Ren, Q. Gao, S. Kang, S. Sun, and K. Niu, "Pattern division multiple access- a novel nonorthogonal multiple access for fifth-generation radio networks," *IEEE Transactions on Vehicular Technology*, vol. 66, no. 4, pp. 3185–3196, July 2017.

[182] Y. Cao, H. Sun, J. Soriaga, and T. Ji, "Resource spread multiple access - a novel transmission scheme for 5G uplink," in *IEEE 86th Vehicular Technology Conference (VTC-Fall)*, Sep. 2017, pp. 1–5, Toronto,ON.

[183] J. An and W. Chung, "Single-led multichannel optical transmission with SCMA for long range health information monitoring," *Journal of Lightwave Technology*, vol. 36, no. 23, pp. 5470–5480, Dec. 2018.

[184] Y. Qiu, S. Chen, H.-H. Chen, and W. Meng, "Visible light communications based on CDMA technology," *IEEE Wireless Communications*, vol. 25, no. 2, pp. 178–185, Apr. 2018.

[185] J. A. Salehi, "Code division multiple-access techniques in optical fiber networks - part I: Fundamental principles," *IEEE Transactions on Communications*, vol. 37, no. 8, pp. 824–833, Aug. 1989.

[186] W. C Yang, G.-C; Kwong, "Performance analysis of optical CDMA with prime codes," *Electronics Letters*, vol. 33, no. 7, pp. 569–570, Mar. 1995.

[187] J. A. Martin-Gonzalez, E. Poves, and F. J. Lopez-Hernandez, "Random optical codes used in optical networks," *IET Communications*, vol. 3, pp. 1392–1401(9), Aug. 2009.

[188] M. F. Guerra-Medina, O. González, B. Rojas-Guillama, J. A. Martín-González, F. Delgado, and J. Rabadán, "Ethernet-OCDMA system for multi-user visible light communications," *Electronics Letters*, vol. 48, pp. 227–228(1), Feb. 2012.

[189] Z. Zheng, T. Chen, L. Liu, and W. Hu, "Experimental demonstration of femtocell visible light communication system employing code division multiple access," in *Optical Fiber Communications Conference and Exhibition (OFC)*, Mar. 2015, pp. 1–3, Los Angeles, CA.

[190] Y. H. Lee and S. J. Kim, "Sequence acquisition of DS-CDMA systems employing Gold sequences," *IEEE Transactions on Vehicular Technology*, vol. 49, no. 6, pp. 2397–2404, Nov. 2000.

[191] D. Zaccarin and M. Kavehrad, "An optical CDMA system based on spectral encoding of LED," *IEEE Photonics Technology Letters*, vol. 5, no. 4, pp. 479–482, Apr. 1993.

[192] C. Wu, H. Zhang, and W. Xu, "On visible light communication using LED array with DFT-spread OFDM," in *IEEE International Conference on Communications (ICC)*, Aug. 2014, pp. 3325–3330, Sydney, Australia.

[193] S. D. Dissanayake and J. Armstrong, "Comparison of ACO-OFDM, DCO-OFDM and ADO-OFDM in IM/DD systems," *Journal of Lightwave Technology*, vol. 31, no. 7, pp. 1063–1072, Apr. 2013.

[194] Lumileds Holding B.V., *DS190 LUXEON IR Compact Line Product Datasheet*, 2018.

[195] J. Abshire, "Performance of OOK and low-order PPM modulations in optical communications when using APD-based receivers," *IEEE Transactions on Communications*, vol. 32, no. 10, pp. 1140–1143, Oct. 1984.

[196] F. Xu, M. Khalighi, and S. Bourennane, "Coded PPM and multipulse PPM and iterative detection for free-space optical links," *IEEE/OSA Journal of Optical Communications and Networking*, vol. 1, no. 5, pp. 404–415, Oct. 2009.

[197] F. R.K. Chung, J. A. Salehi, and V. K. Wei, "Optical orthogonal codes: Design, analysis and applications," *IEEE Transactions on Information Theory*, vol. 35, no. 3, pp. 595–604, May 1989.

[198] J. A. Salehi, "Emerging optical CDMA techniques and applications," *International Journal of Optics and Photonics*, vol. 1, no. 1, Mar. 2007.

[199] J. G. Proakis and M. Salehi, *Digital Communications*, McGraw-Hill, New York, 5th edition, 2007.

[200] D. C. Chen, B. J. Sheu, and W. C. Young, "A CDMA communication detector with robust near-far resistance using paralleled array processors," *IEEE Transactions on Circuits and Systems for Video Technology*, vol. 7, no. 4, pp. 654–662, Aug. 1997.

[201] J. A. Salehi and C. A. Brackett, "Code division multiple-access techniques in optical fiber networks - part II: Systems performance analysis," *IEEE Transactions on Communications*, vol. 37, no. 8, pp. 834–842, Aug. 1989.

[202] O. Tomoaki, "Performance analysis of indoor infrared wireless systems using PPM CDMA," *Electronics and Communications in Japan (Part I: Communications)*, vol. 85, no. 1, pp. 1–10, 2002.

[203] S. Zahedi and J. A. Salehi, "Analytical comparison of various fiber-optic CDMA receiver structures," *Journal of Lightwave Technology*, vol. 18, no. 12, pp. 1718–1727, Dec. 2000.

[204] F. Xu, M. Khalighi, and S. Bourennane, "Impact of different noise sources on the performance of PIN- and APD-based FSO receivers," in *International Conference on Telecommunications (ConTel)*, June 2011, pp. 211–218, Graz, Austria.

[205] K. Lee, H. Park, and J. R. Barry, "Indoor channel characteristics for visible light communications," *IEEE Communications Letters*, vol. 15, no. 2, pp. 217–219, 2011.

[206] HAMAMATSU Photonics, *SI PIN photodiodes: S5106, S5107, S7509, S7510*, May 2018.

[207] G. P. Agrawal, *Fiber-Optic Communications Systems*, Wiley, 1992.

[208] S. Zahedi, J. A. Salehi, and M. Nasiri-Kenari, "M-ary infrared CDMA for indoors wireless communications," in *International Symposium on Personal, Indoor and Mobile Radio Communications (PIMRC)*, Oct. 2001, vol. 2, pp. 6–10, San Diego, CA.

[209] H. Schulze, "Frequency-domain simulation of the indoor wireless optical communication channel," *IEEE Transactions on Communications*, vol. 64, no. 6, pp. 2551–2562, 2016.

[210] R. G. A. Gallo, A. M. Abdelaziz, M. Alghoniemy, and H. M. H. Shalaby, "Real-DFT based DCO-OFDM and ACO-OFDM for optical communications systems," in *International Conference on Transparent Optical Networks (ICTON)*, July 2019, pp. 1–4, Angers, France.

[211] C. Aupetit-Berthelemot and M. F. O. Sanya, "An IFFT/FFT size efficient improved ACO-OFDM scheme for next-generation passive optical network," in *European Conference on Networks and Optical Communications (NOC)*, June 2016, pp. 111–116, Lisbon, PT.

[212] M. Chen, X. Xiao, Z. R. Huang, J. Yu, F. Li, Q. Chen, and L. Chen, "Experimental demonstration of an ifft/fft size efficient dft-spread ofdm for short reach optical transmission systems," *Journal of Lightwave Technology*, vol. 34, no. 9, pp. 2100–2105, May 2016.

[213] C. Chen, D. A. Basnayaka, and H. Haas, "Downlink performance of optical attocell networks," *Journal of Lightwave Technology*, vol. 34, no. 1, pp. 137–156, Jan. 2016.

[214] M. W. Eltokhey, M. A. Khalighi, A. S. Ghazy, and S. Hranilovic, "Hybrid NOMA and ZF precoding transmission for multi-cell VLC networks," *IEEE Open Journal of the Communications Society*, vol. 1, pp. 513–526, Apr. 2020.

[215] M. J. Hasan, M. A. Khalighi, J. GarcÃa-MÃ¡rquez, and B. BÃ©chadergue, "Performance analysis of optical-CDMA for uplink transmission in medical extra-WBANs," *IEEE Access*, vol. 8, pp. 171672–171685, Sept. 2020.

[216] Stanley Electric Co. Ltd., *HDN1102W-TR Standard Product Specifications*, 2014.

[217] M. Morelli, L. Sanguinetti, and H. V. Poor, "A robust ranging scheme for OFDMA-based networks," *IEEE Transactions on Communications*, vol. 57, no. 8, pp. 2441–2452, Aug. 2009.

[218] Y. Jiang, Y. Wang, P. Cao, M. Safari, J. Thompson, and H. Haas, "Robust and low-complexity timing synchronization for DCO-OFDM LiFi systems," *IEEE Journal on Selected Areas in Communications*, vol. 36, no. 1, pp. 53–65, Jan. 2018.

[219] S. Tian, K. Panta, H. A. Suraweera, B. J. C. Schmidt, S. McLaughlin, and J. Armstrong, "A novel timing synchronization method for ACO-OFDM-based optical wireless communications," *IEEE Transactions on Wireless Communications*, vol. 7, no. 12, pp. 4958–4967, Dec. 2008.

[220] Tuan-Anh Truong, Matthieu Arzel, Hao Lin, Bruno Jahan, and Michel Jezequel, "New low-complexity and robust time synchronization technique for optical IMDD OFDM transmissions," *Opt. Express*, vol. 22, no. 12, pp. 14322–14340, June 2014.

[221] X. Qian, Y. Deng, H. Deng, Y. Hu, C. Zhang, and J. Du, "Synchronisation algorithm based on zero correlation code pair for OFDM-based VLC systems," *IET Communications*, vol. 11, no. 2, pp. 205–210, Jan. 2017.

[222] Alan V. Oppenheim and Ronald W. Schafer, *Discrete-Time Signal Processing*, Prentice Hall Press, USA, 3rd edition, 2009.

[223] S. So and K. K. Paliwal, "Reconstruction of a signal from the real part of its discrete fourier transform [tips & tricks]," *IEEE Signal Processing Magazine*, vol. 35, no. 2, pp. 162–174, Mar. 2018.

[224] H. Elgala, R. Mesleh, and H. Haas, "Non-linearity effects and predistortion in optical OFDM wireless transmission using LEDs," *International Journal of Ultra Wideband Communications and Systems*, vol. 1, no. 2, pp. 143–150, Oct. 2009.

[225] S. H. Han and J. H. Lee, "An overview of peak-to-average power ratio reduction techniques for multicarrier transmission," *IEEE Wireless Communications*, vol. 12, no. 2, pp. 56–65, Apr. 2005.

[226] Adriano J C Moreira, Rui T Valadas, A M De, and Oliveira Duarte, "Optical interference produced by artificial light," May 1997.

[227] W. Zheng, K. Li, and K. Li, "Scaled radix-2/8 algorithm for efficient computation of length-$N = 2^m$ DFTs," *IEEE Transactions on Signal Processing*, vol. 62, no. 10, pp. 2492–2503, Mar. 2014.

[228] J. Cooley and J. Tukey, "An algorithm for the machine calculation of complex Fourier series," *Mathematics of Computation*, vol. 19, no. 90, pp. 297–301, 1965.

[229] S. Bouguezel, M. O. Ahmad, and M. N. S. Swamy, "A general class of split-radix FFT algorithms for the computation of the DFT of length-$2^m$," *IEEE Transactions on Signal Processing*, vol. 55, no. 8, pp. 4127–4138, July 2007.

[230] H. M. H. Shalaby, "Chip-level detection in optical code division multiple access," *Journal of Lightwave Technology*, vol. 16, no. 6, pp. 1077–1087, June 1998.

[231] S. Mashhadi and J. A. Salehi, "Code-division multiple-access techniques in optical fiber networks - part III: Optical AND logic gate receiver structure with generalized optical orthogonal codes," *IEEE Transactions on Communications*, vol. 54, no. 8, pp. 1457–1468, Aug. 2006.

[232] A. Keshavarzian and J. A. Salehi, "Optical orthogonal code acquisition in fiber-optic CDMA systems via the simple serial-search method," *IEEE Transactions on Communications*, vol. 50, no. 3, pp. 473–483, Mar. 2002.

[233] R. W. Apperson, Z. Yu, M. J. Meeuwsen, T. Mohsenin, and B. M. Baas, "A scalable dual-clock FIFO for data transfers between arbitrary and haltable clock domains," *IEEE Transactions on Very Large Scale Integration (VLSI) Systems*, vol. 15, no. 10, pp. 1125–1134, Oct. 2007.

[234] T. J. Chaney and C. E. Molnar, "Anomalous behavior of synchronizer and arbiter circuits," *IEEE Transactions on Computers*, vol. C-22, no. 4, pp. 421–422, Apr. 1973.

[235] I. Kuon and J. Rose, "Measuring the gap between FPGAs and ASICs," *IEEE Transactions on Computer-Aided Design of Integrated Circuits and Systems*, vol. 26, no. 2, pp. 203–215, 2007.

[236] R. Cameron and B. Woerner, "Performance analysis of CDMA with imperfect power control," *IEEE Transactions on Communications*, vol. 44, no. 7, pp. 777–781, July 1996.

[237] L. Rodrigues, M. Figueiredo, and L. N. Alves, "Optimized analog multi-band carrierless amplitude and phase modulation for visible light communication-based internet of things systems," *Sensors*, vol. 21, no. 7, Apr. 2021.